Detecting Alpine glacier changes from a combination of ICESAT-2 and GEDI data

Timo Bisschop

MSc Thesis

TU Delft

Detecting Alpine glacier changes from a combination of ICESAT-2 and GEDI data

By

Timo Bisschop

Master Thesis

January, 2021

Student number: 4297199

Supervisor:	Dr. R.C. (Roderik) Lindenbergh
Thesis committee:	Dr. H. (Harry) Zekollari
	Dr. Ir. B. (Bert) Wouters

Abstract

The melting of mountain glaciers worldwide contributes significantly to global sea level rise, and is considered an indicator of climate change. The accurate modelling of glacier heights is crucial for determining their past, current and future state. The new lidar altimeters ICESAT-2 and GEDI were launched in 2018, which could provide valuable new data in this regard. ICESAT-2 uses a novel photon counting technique that delivers elevation data at an unprecedented 0.7 m along-track resolution. This also poses questions about how such data should be processed. GEDI uses a more conventional full waveform sensor, which creates a vertical profile of surface returns every 60 m representing a footprint with a 30 m diameter. In this thesis the potential of ICESAT-2 and GEDI for detecting glacier changes in Austria is examined.

The vertical errors on the Austrian glaciers of the ATL03 geolocated photons and ATL06 Land ice elevation data products of ICESAT-2 were found to be 1.94 and 1.72 meters respectively, which outperforms most alternative sensors. The GEDI L2A product provides an error of 5.80 m for the same area. For both sensors, the horizontal geolocation error was found to be relatively large, which results in a strong relation between the surface gradient and the vertical error.

The high resolution and accuracy of ICESAT-2 can provide valuable detailed information about glacier height differences worldwide. The inclusion of GEDI data can help provide observations in sparsely sampled areas, but considering its relatively poor resolution and accuracy better alternatives may be available.

The satellite observations were confined to glacier inventory outlines and compared to a high quality Digital Elevation Model of Austria. The results show an average glacier height loss of 5.85 m for ICESAT-2 and 4.86 m for GEDI, with the majority of observations representing the period 2010-2019. The height differences were compared with their local elevation, slope, orientation and their distance to the glacier edge, in order to find what features could assist in extrapolating the observations. All features show some relation with the glacier height differences, but the elevation and distance to glacier edge were found to contribute the most information.

Spaceborne lidar data is confined to narrow profiles of the surface, so they require extrapolation to make conclusions about the total state of the glaciers. The total mass difference of Austria was estimated first by simply applying the average height difference to the total glacier area, and secondly by ordinary cokriging with the elevation. Both techniques agree on a total mass loss of 1.59 gigatons, while the cokriging method additionally results in a more detailed image of mass loss for individual glaciers. For the Ötztal region a mass loss of 77.07 megatons annually was estimated for the period 2010-2019.

Preface

This thesis concludes my master's degree in Geoscience and Remote Sensing at Delft University of Technology. In this research, I have examined satellite Lidar data to study the melting of glaciers in Austria, a subject closely related to climate change. I hesitated between several graduation topics, but I believe I have made the right decision and I am proud of the result.

I would like to thank Roderik Lindenbergh for being such a great supervisor. This thesis would not have been possible without your enthusiastic support and insightful feedback. It was always a pleasure to discuss my progress with you. Thank you also for asking me to be the assistant for Lidar scanning for the past years, which has allowed me to work on a number of fascinating projects and meet so many interesting people.

I would also like to express gratitude to my supervisors Bert Wouters and Harry Zekollari for their valuable knowledge and feedback.

When I began my thesis, the COVID pandemic was just getting started. The lockdown has prevented me from getting too distracted from my work, but it has also made for some boring months. I would like to thank my friends for keeping me motivated during these times. Your support, friendship and humour have helped me a lot.

Last but not least, I would like to thank my parents, brother and sister for their love and support.

Timo Bisschop

Delft, January 2021

Contents

1. Introduction

In all mountain ranges on Earth, glacial mass has decreased substantially over the past decades. The rate of glacial mass loss in the 21st century has reached a level that is unprecedented for the observed time span [1]. Excluding the Greenland and Antarctic ice sheets, estimates for the mass loss of ice during the last decade lie between 200 and 270 gigatons per year (Estimates differ due to different time ranges and due to different methods for combining types of observations) [2] [3] [4]. This is equivalent to 0.554 to 0.748 millimetres of annual sea level rise, and accounts for approximately a third of the total global ice loss.

The International Panel on Climate Change (IPCC) considers mountain glaciers to be sensitive climate change indicators [5], but the rapid disappearance of mountain glaciers also has regional and local consequences. Glacier-fed river runoffs can be either increased (due to a larger amount of melt) or decreased (due to a limited amount of ice available for melt), depending on circumstances. A change in runoff can have an impact on water supply, agriculture and hydropower. In addition, local ecosystems have already changed significantly in areas where glaciers have retreated and will continue to do so until an equilibrium is reached. In some areas natural hazards such as landslides and glacial floods may become more likely [6].

More accurate observation techniques of glaciers could be used to decrease the uncertainty of their contribution to sea level rise and the impact of climate change, as well as to more accurately predict and possibly mitigate local and regional effects. An increase of glacier observations can also be used to validate or calibrate projections of the state of glaciers. In recent years two new lidar satellite sensors have been launched; namely ICESAT-2 and GEDI, and examining the possibility of combining them for glacier observations is therefore of interest.

Combining ICESAT-2 and GEDI could potentially give a much needed improvement in coverage and measurement frequency of mid- and low-latitude mountain glaciers, and therefore improve the accuracy of glacier change detection. This combination will however introduce some questions regarding how to handle the differences of the two data sources.

While the spatial and temporal resolution of glacier altimetry measurements could be improved this way, spaceborne altimetry will never cover the complete area of any specific glacier, but only supply heights along narrow ground-tracks. This also has as an effect that the amount of locations which are observed at multiple different times is minimal. This can be solved by taking a complete Digital Elevation Model of the glacier created by airborne altimetry and taking all differences relative to this datum. These differences will still only cover a small portion of the glacier's area. In order to make conclusions about the general state of the glacier, some sort of extrapolation will be required.

The height change of mountain glaciers is not constant over their area, but depends on the location within the system. One method for extrapolation is to find features that vary depending on the location on the glacier. Examples of possible features are elevation, distance to the glacier edge, slope and orientation. These features could then be correlated with the measured change from altimetry, and be used to estimate glacier change at locations without measurements. It is expected that the feature with the most influence by far will be the elevation of the glacier. It will be investigated how exactly glaciers change with elevation, what other features have an influence, and how an estimation of the glacier mass loss can be made with sparse data.

The Austrian Alps have been selected as a study area, because they are at a latitude that is regularly observed by both GEDI and ICESAT-2, high quality Digital Elevation Models are freely available, and significant mass loss of the glaciers has been known to occur [7].

The main research question for this master thesis is defined as:

How can a combination of ICESAT-2 and GEDI data be used to detect changes of Alpine glaciers?

This will be further split up between the following sub-questions:

1. Why is Alpine glacier change relevant?
2. What is a suitable workflow to process ICESAT-2 and GEDI data to ice thickness changes?
    - How are ICESAT-2 geolocated photon and GEDI geolocated waveform products created and how do they compare?
    - How does a combination of ICESAT-2 and GEDI improve the spatial and temporal coverage for the selected Alpine glaciers?
    - How can Lidar altimetry be used in combination with a Digital Elevation Model to estimate ice thickness changes?
    - What is the quality of estimated ice thickness changes?
3. How can characteristic features (such as elevation, slope, proximity to the edge of the glacier) of locations on the glacier be created and how do they correlate with their estimated ice thickness change?
4. Can estimated ice thickness changes be used to infer the mass balance of the whole glacier?
5. How do the results compare to those obtained by other methods?

Figure 1: Kesselwandferner [8]

2. Glacier Change Observations

In this chapter an introduction will be given on glacier change observations. Firstly, the morphology of glaciers will be described, which gives insight into what glacier changes may be expected in Austria. Secondly, the general types of methods for monitoring glacier changes will be described, and finally an overview of satellite sensors suitable for glacier studies will be given.

2.1 Glacier Morphology

The spatial distribution of ice loss within a mountain glacier is intrinsically linked to the glacier structure. Larger glaciers are generally separated into an accumulation zone and an ablation zone by the equilibrium line, as shown in figure 2. The accumulation zone is the high elevation area where snow is collected over years and compressed into firn and ice. The ablation zone is the low-lying glacier tongue where ice flows into the area and is subsequently melted or sublimated. Factors including the mean glacier elevation, slope of the glacier tongue, debris cover, and avalanche contributing area all influence the glacier mass balance [9]. The largest examples of this type of valley glacier in Austria are the Hintereisferner and Gepatschferner in the Ötztal in Tirol, and the Pasterze glacier in Carinthia.

A distinction is made between glacier retreat, where the extent of the glacier decreases, and glacier thinning. Glacier retreat significantly alters the geometry of the glacier, and therefore also its ice mass fluxes. Even glaciers located in the same region which are subject to the same climate and weather conditions can react differently to climate change due to differences in their morphology [10]. The mass balance of a glacier is impacted immediately by changes in climate but can take decades or centuries to reach a new steady state [11].

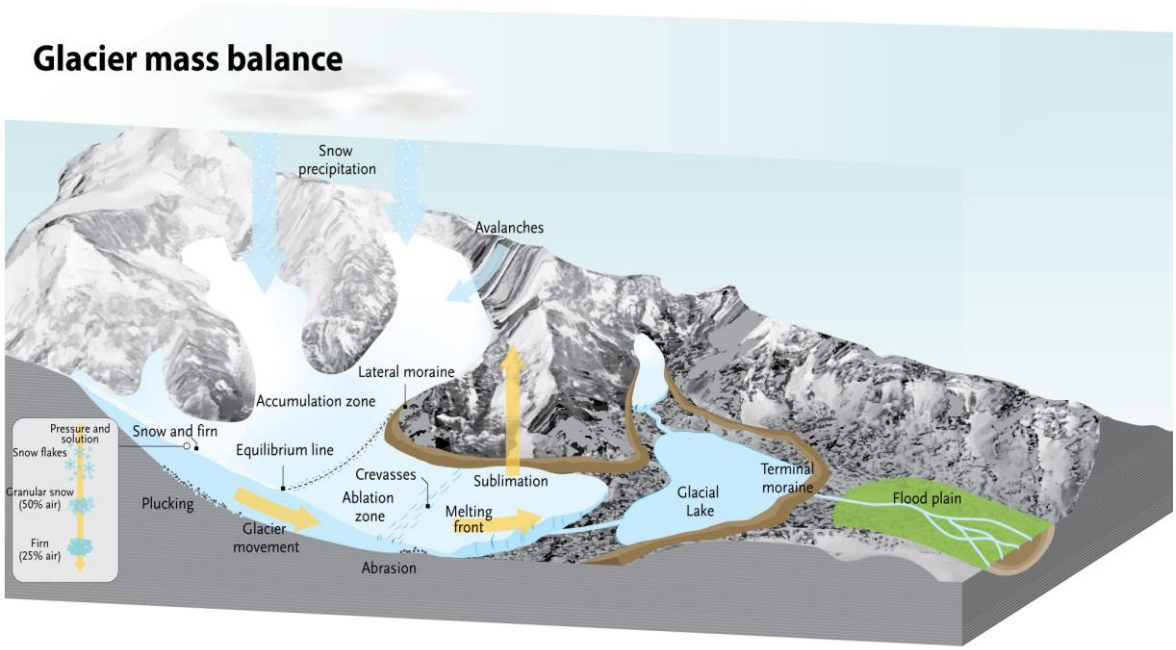

Figure 2: Glacier morphology and mass balance components [12]

In addition to the well-defined valley glaciers described in figure 2, many smaller patches of permanent ice exist in Austria. The smallest types of glaciers often have little to no internal ice flow, which is why they are sometimes called ice patches instead. The glacier inventories used in this study do not differentiate between different types of permanent ice, and their mass changes are just as relevant, so they are included in the analysis nonetheless.

Small glaciers can be divided in types that are the remains of a larger glacier (in which case they can be called glacierets) and types that are simply smaller areas where snow and firn has accumulated over time [13]. The Austrian glaciers have retreated significantly since the little ice age, and as a result the smaller types of remaining glaciers are relatively common [14].

Cirque glaciers occur in cases where the glacier tongue has receded so far that only the upmost of the old accumulation zone remains, often in a circular shape. Smaller ice masses that occur on steep mountain sides are often called hanging glaciers, cliff glaciers or apron glaciers. Hanging glaciers can show mass loss through avalanches caused by structural instability, which may take place even if no melting is taking place [15]. In general, smaller glaciers tend to react more quickly to changes in temperature or snowfall [14].

Figure 3: Hallstatter Glacier [16]

2.2 Monitoring of Glaciers

Three general methods exist for the estimation of mass loss of glaciers: glaciological surveys, gravimetry and altimetry. All three techniques are in some way limited in their spatial and temporal range and resolution, as well as their accuracy.

Glaciological surveys commonly measure a number of meteorological, geometric and mass balance characteristics such as glacier runoff, precipitation on the glacier and the surface area of the glacier [2]. They are limited mainly due to practicality. Only a limited number of glaciers can be measured, and of those only a limited area, so a large amount of extrapolation is required. However, they have the advantage of multiple decade long time series for a number of relatively easily accessible glaciers, such as the list of reference glaciers maintained by the World Glacier Monitoring Service.

Gravimetry involves mapping changes in the earth's gravity field. These changes correspond to large movements of mass in the earth's system. When correcting for other significant signals (such as glacial isostatic adjustment, hydrology, atmosphere, earthquakes and volcanic activity) changes in gravity can be used to determine ice mass loss on a large scale. However, it cannot be used for individual glaciers or smaller regions because it has limited spatial resolution [17].

Altimetry measurements are distinguished by their platform (airborne or spaceborne) and method (Radar, photogrammetry or Lidar). Airborne altimetry has a higher resolution and accuracy than can be reached by spaceborne sensors, but has practical limits in terms of price and accessibility so that only a small number of glaciers will be measured in this way a limited number of times. Spaceborne Lidar sensors only collect measurements on narrow paths on the ground, essentially creating profiles of the surface. This is the main disadvantage of spaceborne Lidar measurements for glaciers: glaciers will be measured a limited number of times (or not at all), and the measurements are only dense in one direction. Combining different satellite Lidar sensors would increase coverage, which would be greatly beneficial.

Many studies combine glaciology, gravimetry and altimetry results to arrive at estimates for long term trends and large scales, e.g. [2] [7].

The general focus of remote sensing glacier mass balance studies has been the contribution of glaciers to global sea level ice, for which the combined ice loss of a large region is most important. However, the behaviour of individual glaciers is also of interest, since this can give more insight into how they react to climate change, which allows for more accurate modelling and prediction of future ice melt. In addition, glacier changes are not entire homogeneous over a mountain region, and the behaviour of individual glaciers can be important for local hydrology, ecology and tourism. Accurate height change measurements are important for the study of the interplay between mass balance, morphology and climate change [18].

2.3 Satellite Sensors for Detecting Glacier Change

Some of the missions commonly used for similar types of studies include: SRTM, ASTER, GRACE-FO, ICESAT, TanDEM-X and CRYOSAT-2. Their methods and performance will be summarised here.

An overview of the sensor properties as described in this chapter is given in the table below. It should be noted that the accuracy of these sensors is often variable, and the values shown in this table are only a rough indication of the performance over mountainous terrain.

	Timespan	Resolution	Accuracy (approximate)	Data availability
SRTM	February 2000	30 m	10 m	Free
ASTER	February 2000 - present	30 m	30 m	Free
GRACE(-FO)	March 2002 - October 2017, May 2018 – present	100's of km	N/A	Free
ICESAT	January 2003 - February 2010	172 m	1 m	Free
TanDEM-X	June 2010 - present	12 m	4 m	Partly free, partly via proposal
Cryosat-2	April 2010 - present	400 m	40 m	Free

Table 1: Overview of satellite sensor properties

2.3.1 SRTM

The Shuttle Radar Topography Mission (SRTM) was a mission flown in February 2000 with the Space Shuttle Endeavor to create a Digital Elevation Model (DEM) with near global coverage, using X-band and C-band Synthetic Aperture Radar. SRTM is widely used in studies of glacier mass changes [19] [20] [21] [22], for its large coverage, good resolution and because its age results in relatively long timespans with new data, which results in a better image of the average annual mass change. It has a resolution of 1 arcsecond, corresponding to 30 m. The accuracy standard of SRTM was set at 16 m absolute vertical accuracy with a 90% confidence [23]. SRTM is freely available via the EarthExplorer website of the U.S. Geological Survey.

Accuracy assessment of the SRTM-GL1 DEM shows a standard deviation error of 6.6 m, but there is a heavy dependence on the slope of the terrain, pointing to a large horizontal error. Areas with a slope higher than 20 degrees show a standard deviation error of 14.9 m [24]. As can be seen in figure 31 in chapter 5.2, the Austrian glaciers commonly include slopes much steeper than that, so this should always be considered when using SRTM data.

The suitability of SRTM for determining glacier heights is controversial. Some results have shown large disagreements with other methods, likely due to the bias introduced by penetration of the radar signal in snow and ice, and the uncertainty of applied corrections for this bias [25] [26]. The depth of radar penetration can be in the order of meters, but depends on the physical properties of the snow and ice, which are often largely unknown. If no correction is applied, the glacier height in the SRTM will be underestimated, which also leads to an underestimation of the mass change.

A common solution is to apply a correction based on the elevations found in the study area, assuming that low lying areas will contain the bare ice of the ablation zone and high areas will contain loose snow of the accumulation zone. No correction is applied for areas with elevations below the equilibrium line, and a linearly increasing correction is applied for any areas above it [21] [22]. However, determining the suitable magnitude of this correction can be difficult since it depends on the local conditions at the time of data collection. The significant inconsistencies between results as pointed out by Berthier et al. (2018) were explained by a disagreement between penetration bias corrections [25].

Dussaillant et al. (2018) finds that SRTM C-band penetration is only an issue for about 1% of the area of the Northern Patagonia Icefield due to the relatively wet glacier conditions at the time of SRTM collection [27]. However, for any glaciers in the Northern Hemisphere the SRTM was collected around the coldest time of the year, and therefore at the most susceptible to radar penetration.

A comparison of the C-band and X-band DEM's of SRTM could give an indication of the penetration depth of the study area [28]. This assumes that there is no penetration for the X-band, however it has been found that X-band penetration can still reach several meters under certain snow and ice conditions [25]. Only comparing data from the same time of year using the same radar frequency is another approach to reduce bias [29], assuming that glacier conditions will be relatively similar.

2.3.2 ASTER

ASTER (Advanced Spaceborne Thermal Emission and Reflection Radiometer) is an imaging sensor aboard the Terra satellite and has been active since February 2000. DEM's can be created from ASTER using stereo-photogrammetry. The AST14 DEM product is automatically generated this way for any location for every 16 day ASTER repeat. This product has a 30 m resolution and a vertical accuracy ranging between 15 and 60 m depending on the terrain [30]. The ASTER GDEM product is generally not used for glacier mass change calculations since it is created from a composition of ASTER images acquired over the mission's lifetime. ASTER data products are available freely through NASA Earthdata search.

2.3.3 GRACE

The Gravity Recovery and Climate Experiment (GRACE) mission was launched in 2002 and was the first satellite mission dedicated to mapping changes in the earth's gravity field. It finished its mission in October 2017, and Its continuation GRACE-FO was launched in 2018.

Spaceborne gravimetry is mostly applicable for larger regions with significant mass loss and not for individual glaciers or subregions due to its low resolution and the need to correct for other mass change signals (such as glacial isostatic adjustment and hydrology), which is more challenging on a smaller scale. The filtering methods used to process GRACE and GRACE-FO data result in a spreading out of the mass signal over many kilometers. As a result, analysing a subset of glaciers in an area will result in a large amount of signal from neighbouring glaciers leaking in. The spatial resolution of GRACE data is somewhat subjective as it depends on the post-processing strategy, but is in the order of hundreds of kilometers [17].

An advantage of the gravimetric approach compared to lidar is that it measures mass changes directly, so it does not rely on an assumption about ice density. GRACE and GRACE-FO provide a complete global image monthly, allowing for a complete time series without irregularities for the entire mission duration. Mass changes caused by atmospheric movement and hydrology are included in the signal, but cloud coverage is not an issue for gravimetry.

2.3.4 ICESAT

The Ice, Cloud, and Land Elevation Satellite (ICESAT) was the predecessor of ICESAT-2 active from January 2003 until February 2010. It carried the Geoscience Laser Altimeter System (GLAS), measuring the surface at a 172 m along-track resolution with a 70 m footprint. ICESAT data is available via the National Snow & Ice Data Center (NSIDC) website.

Moholdt et al (2010) found a one sigma vertical accuracy of 0.66 m at slopes under 5 degrees in Svalbard by analysing crossover locations [31], with the accuracy depending heavily on the terrain slope.

While ICESAT provided a good accuracy, it lacked in terms of resolution, footprint and coverage, which can be an issue for measuring relatively small mountain glaciers. ICESAT-2 improved upon the first mission in all these aspects, as will be described in chapter 3.

2.3.5 TerraSAR-X and TanDEM-X

TanDEM-X is a 2010 add-on to the TerraSAR-x mission that allows for the creation of DEM's from bistatic radar interferometry. The name TanDEM-X or TDX is also used to refer to the two satellites combined. Height differences can be determined by either creating a DEM from a single TDX pass and comparing it against another DEM, or by directly comparing two interferograms created at different times. As the name implies, the sensor uses the X-band of the radar spectrum, and is therefore less susceptible to radar penetration bias than the C-band SRTM DEM which was created with a longer wavelength. TDX has a ground resolution of 0.4 arcseconds or approximately 12 m [32].

Globally, the TDX DEM has a vertical accuracy of 1.09 m [33]. However, like most altimeters the accuracy decreases for mountainous terrain due to horizontal geolocation errors. Malz et al. (2018) finds an accuracy of 3.14 m when comparing TDX to SRTM in Patagonia [21]. Sommer et al. (2020) found a standard deviation of 4.87 m using a similar method in the Alpes [22], and Neckel et al. (2013) determined an error of 3.70 m in the Himalaya [29]. Neckel et al. also calculated height differences by directly comparing interferograms of TDX and SRTM, which improved the accuracy to 2.38 m. These accuracy assessments were all performed on non-glacier areas, so radar penetration bias is not included. The TDX radar penetration bias is in the order of meters depending on glacier conditions, but can be partially estimated based on the radar backscatter and coherence [34].

TanDEM-X 90 m DEM data is freely available online, whereas higher resolution data products are accessible via a proposal submission.

2.3.6 CRYOSAT-2

The CryoSat-2 satellite was launched in April 2010 and uses the Synthetic Aperture Radar and Interferometric Radar Altimeter (SIRAL). Its main mission objectives are to monitor sea ice and to detect changes on the Antarctic and Greenland ice sheets. Measurement of glacier and ice cap thickness changes is a secondary objective of the Cryosat-2 mission [35].

CryoSat-2 uses a 2.2 cm wavelength (Ku-band), which is shorter than that of TanDEM-X and SRTM, which reduces the radar penetration bias [19]. The sensor uses three different modes, of which the synthetic aperture interferometric (SARIn) mode is used when the satellite crosses any area containing mountain glaciers or the edges of ice sheets and ice caps, including the Alpes [35]. The sampling of CryoSat-2 in SARIn mode tends to cluster towards higher elevations, meaning that valley glaciers can be under-sampled [36] [37]. The Cryosat-2 effective resolution in SARIn mode is approximately 400 meters with some variation depending on the terrain [38]. Accuracy analyses of SARIn data over Antarctica and Greenland show that the accuracy decreases rapidly with increasing terrain gradients. For slopes under 1 degree the random error when compared with ICESAT-1 data is below 5 m, but for the more mountainous coastal area of Greenland this becomes 40 meters [36] [39]. Cryosat-2 has also been used successfully for mass loss studies of ice caps in Patagonia, Svalbard and Iceland [19] [40] [41].

Cryosat-2 has a good spatial coverage, temporal resolution and accuracy over flat terrains. This makes it especially suitable for analysis of larger ice fields and ice sheets. It has been active since 2010 and has a ground track repeat time of 30 days, allowing for a long and detailed time series analysis. However, it provides limited and relatively inaccurate data on smaller mountain glaciers such as those found in Austria. Cryosat-2 data can be accessed freely online via the CryoSat-2 Science Server of the European Space Agency.

3. ICESAT-2 & GEDI Data Products

Three different altimetry data products were used for this thesis; ATL03 and ATL06 from ICESAT-2 and L2A from GEDI. This chapter gives an overview of these products and of how they are created. Lastly, the spatial coverage of the lidar ground tracks over Austria will be described.

3.1 ICESAT-2

An overview of the mission characteristics and data products will be given here, followed by a summarized description of the processing chain from the raw collected data to the land ice surface heights of ATL06.

3.1.1 Mission overview

The Ice, Cloud, and land Elevation Satellite 2 (ICESAT-2) was launched in September 2018 and carries the Advanced Topographic Laser Altimeter System (ATLAS) lidar sensor. Like its predecessor its main purpose is to measure sea ice and ice sheet thickness, which is why it occupies a near polar orbit. Thanks to this orbit it measures heights globally, so it can be used for many other purposes.

ICESAT-2 has two main conceptual differences compared with ICESAT. Firstly, to improve spatial resolution ICESAT-2 splits its laser beam into six separate beams, organized in three pairs each containing a strong and weak beam. The three pairs are separated by 3.3 kilometres, whereas the strong and weak beams in each pair are separated by 90 meters. This also allows for the cross-track slope to be measured. In addition, the footprint of the beams is reduced from the 70 meters of ICESAT to 17 meters for ICESAT-2, and the along-track resolution is increased from 150 meters to 0.7 meters [42]. These improvements are ideal for the sometimes rough surfaces of glaciers, and potentially allow for more accurate change detection.

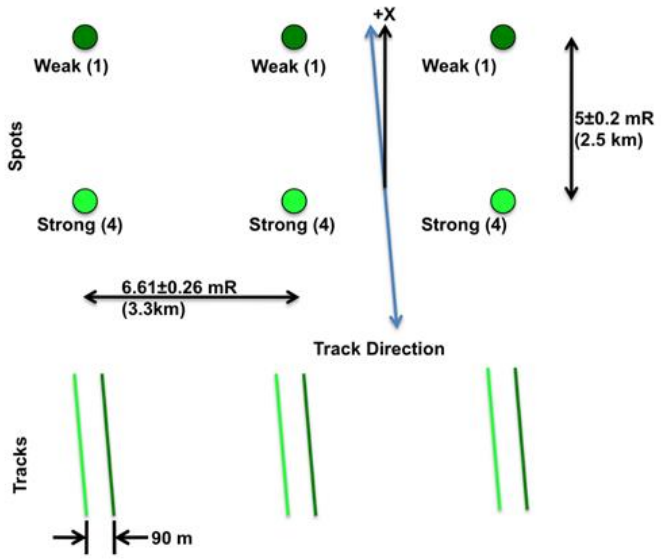

Figure 4: ICESAT-2 ground-track configuration. Six laser beams are used, arranged into three pairs consisting of a weak and strong beam. The pairs are located 3.3 km apart and the beams within each pair are separated by 90 m. The weak beams are always pointed 2.5 km ahead of the strong beams, but this has no consequence on the data pattern of data collection [43].

Secondly, it uses a photon-counting lidar instrument called ATLAS instead of ICESAT's full-waveform lidar called GLAS. This means that instead of measuring the power of the returned laser beam signal over time, single returning photons are detected. This change means that the transmitted signal of the laser could be lowered, which allowed the frequency of the laser beam to be increased while keeping power requirements limited. This resulted in the much higher along-track resolution [43]. The downside of using photon-counting technology is that the returned signal needs to be distinguished from the natural background rate of photons.

An overview of ICESAT-2/ATLAS data products is given in figure 5. The data captured by ATLAS is released in a number of different products to allow different users to select the right location in the processing chain that best suits their needs. For example, users researching techniques to process raw space altimetry data can use the ATL00 product, while users only interested in vegetation height may select ATL08 or ATL18, for which most pre-processing has already been done. The main data products that are of interest for this research are ATL03 Geolocated Photons and ATL06 Land Ice Height. ICESAT-2 data is free to download from the National Snow & Ice Data Center website (nsidc.org).

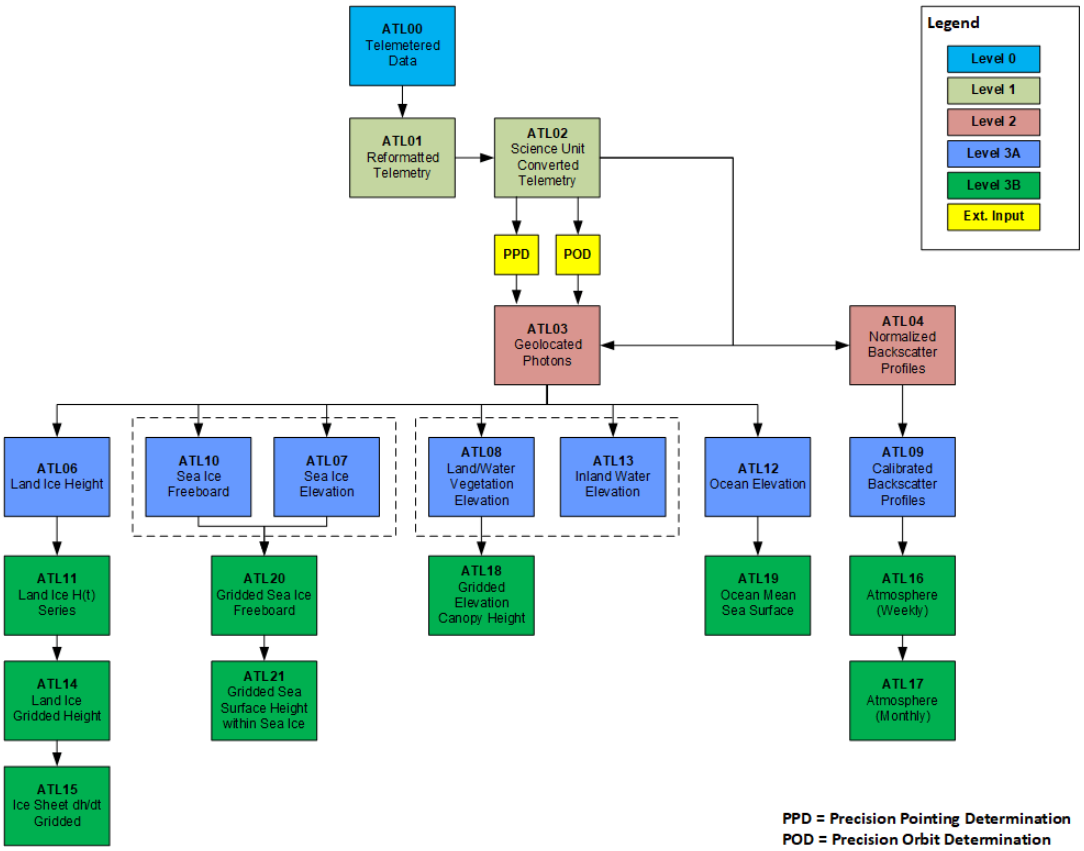

Figure 5: ATLAS product processing chain. Data is released as a number of different products to suit user needs. The products are grouped by level indicating the degree of processing [44].

3.1.2 ATL00 Telemetered Data

Since ATLAS is a photon counting lidar, it not only detects photons from the transmitted signal, but also a number of naturally occurring background photons. In order to reduce data size and ensure that all data can be telemetered some processing steps are done aboard ATLAS for every mainframe, which are along-track segments of 140 meters.

The ATLAS Flight Science Receiver Algorithms document describes the on-board algorithms that are used to select data to be telemetered [45]. The photons are initially filtered for a wavelength of 532 nm. For every mainframe a range of elevations is determined where the surface could realistically be located. This is done based on on-board datasets. Firstly the minimum and maximum elevation of the approximate location of the mainframe are taken from a Digital Elevation Model. This range is vertically extended by 250 meters and used to create a first selection of photons. A histogram is made of this selection, and the bin with the largest amount of returns is assumed to be approximately at the surface. A Digital Relief Map is used to determine the number of bins above and below to be added based on the variability of the elevation in the area. As a consequence, a larger amount of background photons are telemetered for high-relief areas.

By design, a wide margin of background photons is present to ensure that all surface photons are preserved. Figure 6 shows an along-track profile of a single beam over the Austrian Alpes with all telemetered photons. While the data in this figure is from the ATL03 product, it shows the typical amount of photons telemetered in the ATL00 product.

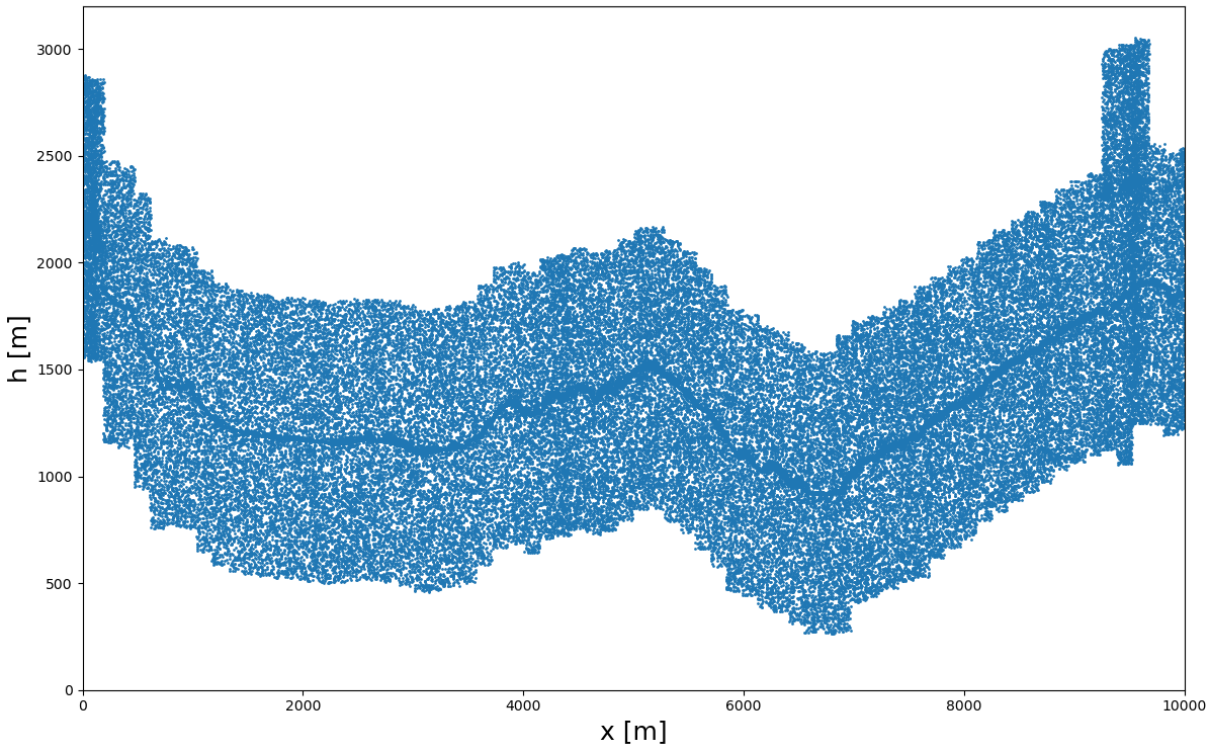

Figure 6: A segment of unfiltered ATL03 data over Austria, showing the vertical extent of telemetered photons.

The rate of background photons is not constant, but depends on the solar elevation angle and the top of atmosphere reflectance of the surface. In order to determine the background rate, an atmospheric histogram is also made and telemetered for every mainframe.

3.1.3 ATL01, ATL02, POD and PPD

After the telemetered data is received, it is time ordered and reformatted into Hierarchical Data Format (HDF) files and released as the ATL01 reformatted telemetry data product [46]. For the ATL02 data product the time of day (TOD) of the transmitted laser pulses is corrected for biases and converted to GPS time, and the time of flight (TOF) of all the detected photons relative to the start of the laser pulse is determined [47]. It also provides radiometric parameters such as the transmitted energy and the receiver sensitivity.

The algorithms for the precise location of the satellite as a function of time are described separately in the Precise Orbit Determination (POD) algorithm theoretical basis document, [48]. The direction of the pointing vector of ATLAS is also derived separately in the Precision Pointing Determination (PPD) algorithm theoretical basis document, [49]. ICESAT-2 uses a combination of stellar tracking and inertial reference units to achieve this. The TOF, POD and PPD parameters are the building blocks that are combined to calculate the geolocation of every photon.

3.1.4. ATL03 Geolocated Photons

The ATLAS algorithms are described in more detail in the ATL03 Algorithm Theoretical Basis Document (ATBD), [50]. The ATL03g ATBD gives a more detailed description of the geolocation algorithm, [51]. An overview of the algorithm steps to derive the geolocation of photons is given in figure 7, where the red bordered area shows the steps described in the ATL03g ATBD.

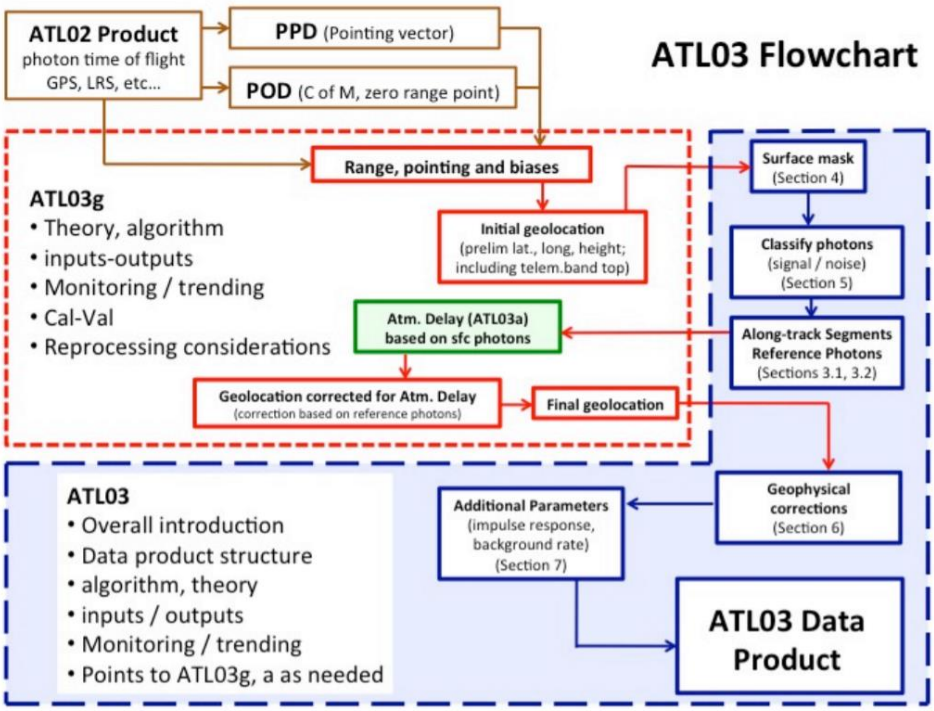

Figure 7: ATL03 geolocation algorithm overview. [50]

Firstly, the TOF of the photons is used to calculate the rough range of every photon bounce point from the instrument. The speed of light in a vacuum is used, and no corrections for atmospheric delay are applied yet. The range bias at the instrument is constantly monitored by directing a small portion of the transmitted laser beam directly back into the sensor. This bias is already applied here.

This range is then combined with the POD and PPD parameters to derive the approximate location of the bounce point on earth. The location is initially derived in the Earth-centred Inertial reference frame and is then converted to the longitude, latitude and height coordinates of the WGS 84 reference system, with ellipsoidal height.

After this initial geolocation the photons are grouped by their surface type. This is done because certain parameters in the subsequent photon classification algorithm are adjusted based on surface type. The used surface types are: land, ocean, sea ice, land ice and inland water. The final purpose of the surface types is to reduce the amount of data that is passed on to the surface specific level 3 algorithms.

The surface type masks are made from a list of external sources. For the glaciers in Austria, the relevant source is the Randolph Glacier Inventory (RGI) version 5.0 [52]. More information about the RGI is given in chapter 4.1 . To ensure that all land ice is captured completely within the surface type mask, a 10 km buffer is added to the RGI. This also means that the surface type cannot be used to select only glacier photons, and that photons commonly belong to multiple surface types.

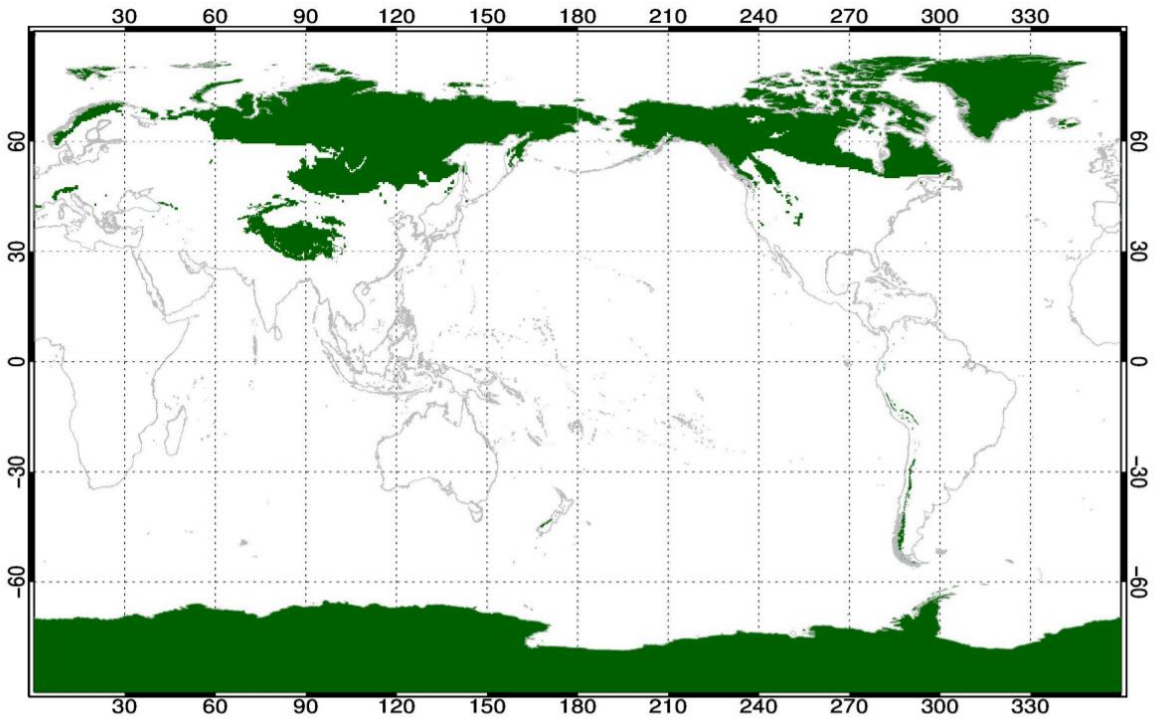

Figure 8: Surface mask for 'Land Ice' type used by ATL03 [50]

The next step is to classify the photons by their likelihood of being a surface return vs being a background photon. As shown in figure 6, all telemetered data is present in ATL03, resulting in a thick layer mostly consisting of background photons. In order to make a distinction between signal and background a system of quality flags is introduced. This distinction is based on a difference in density that is introduced by the addition of surface photons in a constant stream of background photons. In addition, this classification is used to select reference photons for which the atmospheric path delay is computed. The meaning of the quality flags is shown in table 2.

Quality Flag	Confidence	Signal to Noise Ratio
0	Background	-
1	Background, but added as Buffer	-
2	Low	SNR < 40
3	Medium	40 < SNR < 100
4	High	SNR > 100

Table 2: ATL03 quality flags

The photon classification algorithm starts by dividing the photons in along-track segments using a predefined time difference ΔTime. For every ΔTime segment a vertical histogram is made with a bin size of δz. If the number of photons in any of the bins exceeds the threshold value, all the photons of that bin are flagged as surface photons. The threshold value is defined as:

$$T_h = \mu_{bg\_\delta z\_\delta t} + 3\sigma_{bg\_\delta z\_\delta t} \quad (1)$$

Where $\mu_{bg\_\delta z\_\delta t}$ is the mean background rate of photons adjusted for the bin size and $\sigma_{bg\_\delta z\_\delta t}$ is the standard deviation of the background rate adjusted for the bin size. Both values are calculated from the atmospheric photon histogram that is created for every along-track segment of 140 m.

In the case that no histogram bins are found to have an amount of photons larger than the threshold, the bin size δz is increased stepwise until either the threshold is satisfied or the maximum vertical bin size is reached. When the maximum vertical bin size is reached, the along-track width of the histogram δt will also be increased stepwise until the maximum along-track histogram width has been reached. If bins containing surface photons have been found using an increased δt only the photons within the original histogram width ΔTime will be tagged as being surface photons.

In this initial approach the histograms are all created perpendicular to the earth's reference ellipsoid. However, in the case of a steep slope the surface photons will be spread out vertically so that the threshold cannot be reached for any bin size. For this reason the slope is estimated for the remaining gaps based on any surrounding segments for which surface bins are detected. A new histogram is made that is perpendicular to this slope, and the previously described process of bin size adjustment is repeated. In the case that the terrain is very rough and unpredictable the new histogram orientation may still be unable to resolve, so as a last resort a number of other orientations are tried.

To further classify the surface detection the signal to noise ratio of any surface bin is calculated as the number of photons contained in it divided by the current mean background photon ratio $\mu_{bg\_\delta z\_\delta t}$. Table 2 shows how the SNR translates to the quality flag. Algorithms for level 3A data products commonly require a minimum vertical span of photons, so the quality flag with value 1 indicates background photons that are added purely for this requirement.

All predetermined variables used in the algorithm described above are different based on the surface type and whether the track belongs to a strong beam or a weak beam. Therefore, a single photon can have different quality flags if it belongs to multiple surface types. Most importantly the minimum vertical bin size for the land ice surface type is 0.7 m for the strong beam and 0.8 m for the weak beam, showing that the surface is not perfectly resolved but a range of photons remains.

After classification the photons are binned in predetermined 20 meter along-track segments. For every segment a single reference photon is selected that has the highest possible quality (quality flag 4 if available) and lies as close as possible to the centre of the segment. The atmospheric path delay correction is then computed only for the reference photon [53].

The atmospheric path delay is a function of the air density along the path through the atmosphere taken by the signal. This density depends on the air temperature, atmospheric pressure and the water vapour partial pressure. Only the variation in water vapour is considered, since variations in other atmospheric components such as ozone have an insignificant effect. The ATL03 algorithm takes the necessary atmospheric parameters from the GEOS FP-IT numerical weather model, created by NASA's Global Modeling and Assimilation Office. This model has a temporal resolution of three hours, a 0.3125° longitudinal resolution and a 0.25° latitudinal resolution [54].

The resulting atmospheric path delay correction is applied to the whole segment belonging to the reference photon. These corrections are normally in the order of several meters. The photons now have their final geolocation expressed in longitude, latitude and height expressed in the WGS 84 reference system. However, the earth's land surfaces are not at a constant height, but move in relatively short timescales as they are subject to large scale forces. These include the tidal forces of the moon and sun, the shifting weight of the ocean's due to tides and variations in the Earth's rotation and centre of mass. These processes are generally not of interest for users of ATLAS data, so they are computed for every 20 meter segment and adjusted for by default.

The ATL03 data product files also include the geoid height relative to the reference ellipsoid, taken from the Earth Gravitational Model 2008, which is determined for every 20 meter segment but not applied by default.

As of release version 3, ATL03 provides a single, pessimistic estimate of the one-sigma uncertainty of the geolocation process. This value is 20 meters for the horizontal location, and 0.3 meters for height. In future releases, the uncertainties will be provided dynamically per reference photon. However, an estimate in the ATL03g ATBD based on the expected errors in POD, PPD and TOF products shows that under normal conditions the vertical error will not exceed 0.1 m and the horizontal error in both along and cross track directions will not exceed 5 m. [51], pp 41.

Figure 9 shows a short segment of the ATL03 data with the highest quality flag over the Austrian mountains. As can be seen, there is still a number of photons for any given along-track location, and these photons occupy a range of elevations in the order of meters. This distribution of photons can have a number of different sources, including:

- Natural surface roughness at a scale smaller than the resolution
- Random errors in the geolocation
- Random errors in ranging, including atmospheric corrections and the distribution of the transmitted pulse
- Variations in height in the cross-track dimension
- The presence of vegetation

Figure 10 shows how a narrow transmitted pulse is stretched the same way by a rough surface as by a sloped surface with the same height variation.

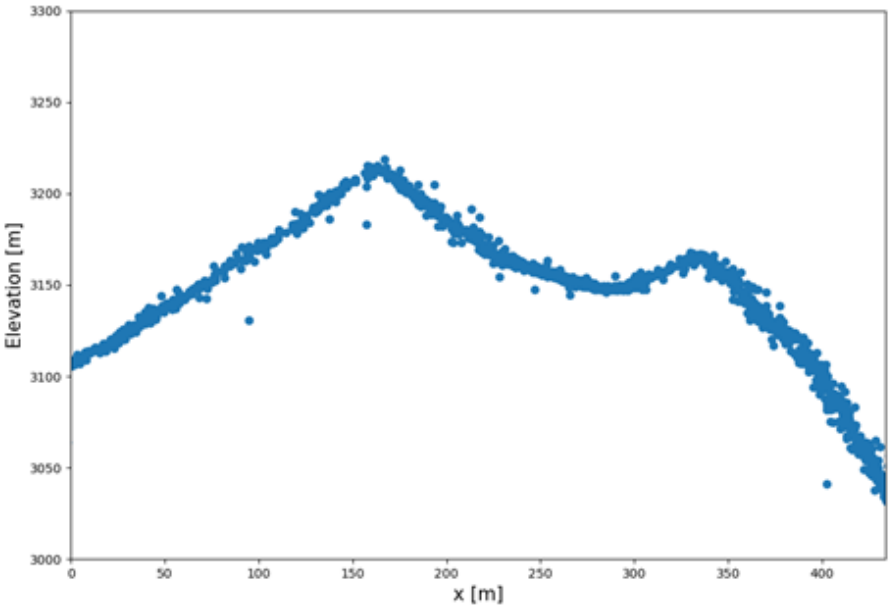

Figure 9: Segment of ATL03 data with quality flag 4 over a mountain top in Austria.

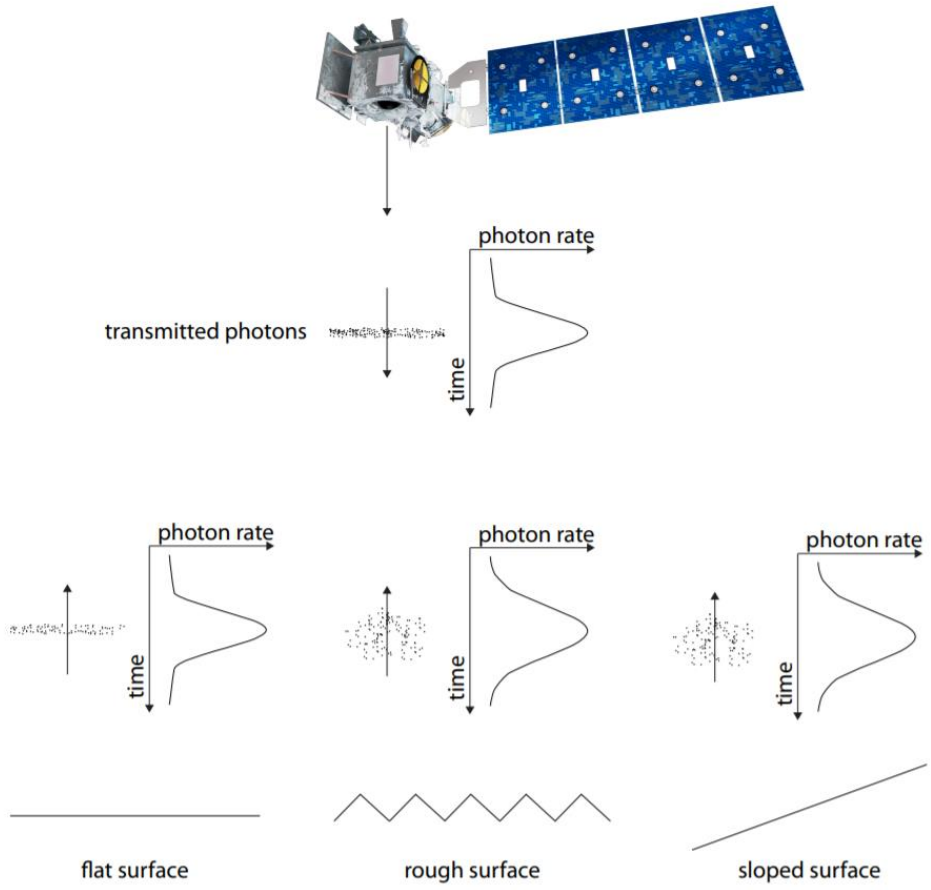

Figure 10: A narrow transmitted pulse is stretched vertically by a surface's roughness and slope [55]

The relevant level 3 data product for glaciers is ATL06: Land Ice Height, which creates a single, unambiguous surface elevation for any location, but also sacrifices along-track resolution in order to increase accuracy. All photons with quality flag values one to four are passed on to the higher level algorithms.

3.1.5. ATL06 Land Ice Elevation

ATL06 transforms the ATL03 geolocated photons into surface heights with an along-track resolution of 20 m. It works on the assumption that the surface can be approximated as a linear slope on a short scale. [55]

For every 40 m segment the algorithm selects the group of ATL03 photons that could describe the surface. For a photon collection of a segment to be considered sufficient the minimal number of photons must be 10 and the largest along-track distance between photons has to be at least 20 meters. These criteria are first tested with all ATL03 photons with a quality flag larger than 1, which are classified as surface. If this fails, the added buffer of photons with quality flag 1 as shown in table 2 are added.

For every valid segment, an initial linear slope is fitted with least squares to all available photons. A rough initial vertical window is created based on the quality of the photons and their spread in the segment. The algorithm then iteratively reduces the window size using the following steps:

1. Create a least-squares fit based on all photons within the current window
2. Calculate all the residuals of the photons, and determine the standard deviation of the residuals, corrected for the expected ratio of background photons to surface photons. Also calculate the expected spread of photons based on the formula described below with zero roughness (R=0)
3. Define a new window height defined as the maximum of the following:
    a. 6 times the standard deviation of the residuals
    b. 6 times the expected standard deviation based on equation 1
    c. 0.75 times the last window height
    d. 3 meters
4. Return to step 1 unless the amount of iterations exceeds 20 or the window refinement has not resulted in a change of photon selection

The vertical spread of photons for any location (such as shown in figure 9) is estimated by the formula:

$$\sigma_{rx} = \left[{\sigma_{tx}}^2 + \left(\frac{W}{8c} tan\varphi \right)^2 + \left(\frac{R}{2c} \right)^2 \right]^{\frac{1}{2}} \quad (2)$$

Where σ_{rx} is the expected vertical standard deviation of photons, σ_{tx} is the standard deviation of the transmitted pulse, W is the footprint diameter, c is the speed of light in a vacuum, φ is the local surface slope angle and R is the root mean square deviation from the surface [56]. This estimation is used in step 2 and 3 of the iterative process to ensure the window size is not reduced too drastically.

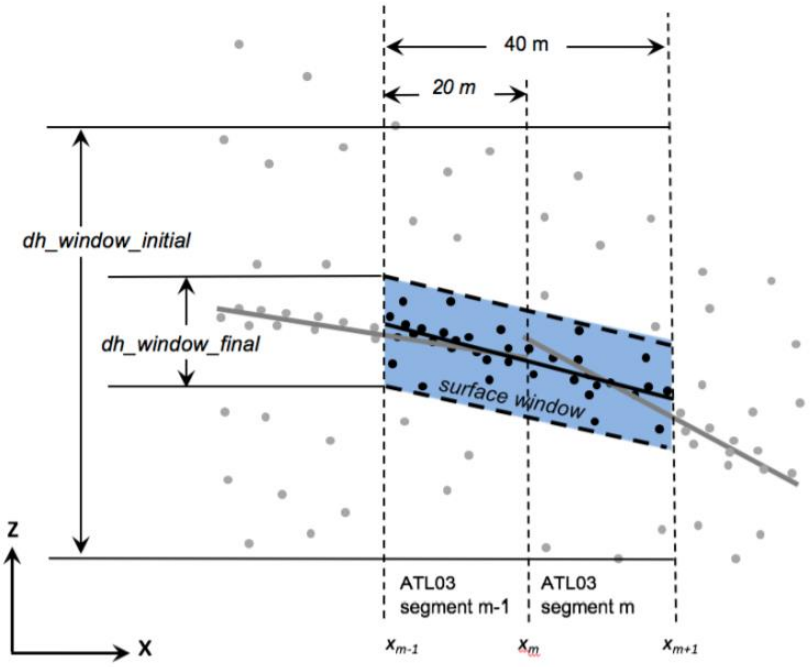

Figure 11: ATL06 window height reduction [55]

After the surface window has converged some bias corrections are applied. The difference between the mean and median photon height in the window is examined to apply a correction for the effect of outliers. A correction is also applied for the 'first photon effect', which takes place when two photons arrive at the ATLAS sensor with a very small time difference between them. The sensor is unable to make a distinction between the two and only the first photon will be detected. Therefore, a slight positive bias is expected when a large group of photons is considered, such as in the 40 meter segments of the ATL06 algorithm. Lastly, the transmitted pulse of ATLAS is not perfectly symmetric, but has a trailing edge, also resulting in an offset when considering larger groups of photons. All these biases are estimated for every segment, and applied to the surface height by default.

ATL06 provides two different uncertainty estimate parameters. The parameter *h_li_sigma* propagates the ranging error of the ATL03 photons in the least squares fit. The parameter *sigma_geo_h* takes the ATL03 geolocation error and calculates the vertical error caused by this shift assuming the determined slope is constant. As mentioned for ATL03, the geolocation and ranging errors are not yet determined dynamically for the data product version 3. A constant and rather pessimistic value is given instead. These values are propagated for the ATL06 uncertainties, meaning they reach quite large values, in the order of tens of meters for *sigma_geo_h*.

A new quality flag is made for ATL06 which indicates if the surface point has failed any of a number of quality tests. This includes information about the surface window detection, the signal to noise ratio and the size of residuals. Points with a quality flag of 0 are considered to be of high quality.

Figure 12 shows a comparison of ATL03 data of quality flag 4 and ATL06 data over the Hintereisferner glacier. The ATL06 heights indeed seem robust to outliers in ATL03. ATL03 seems to include the presence of crevasses in the glacier, while ATL06 represents the top surface.

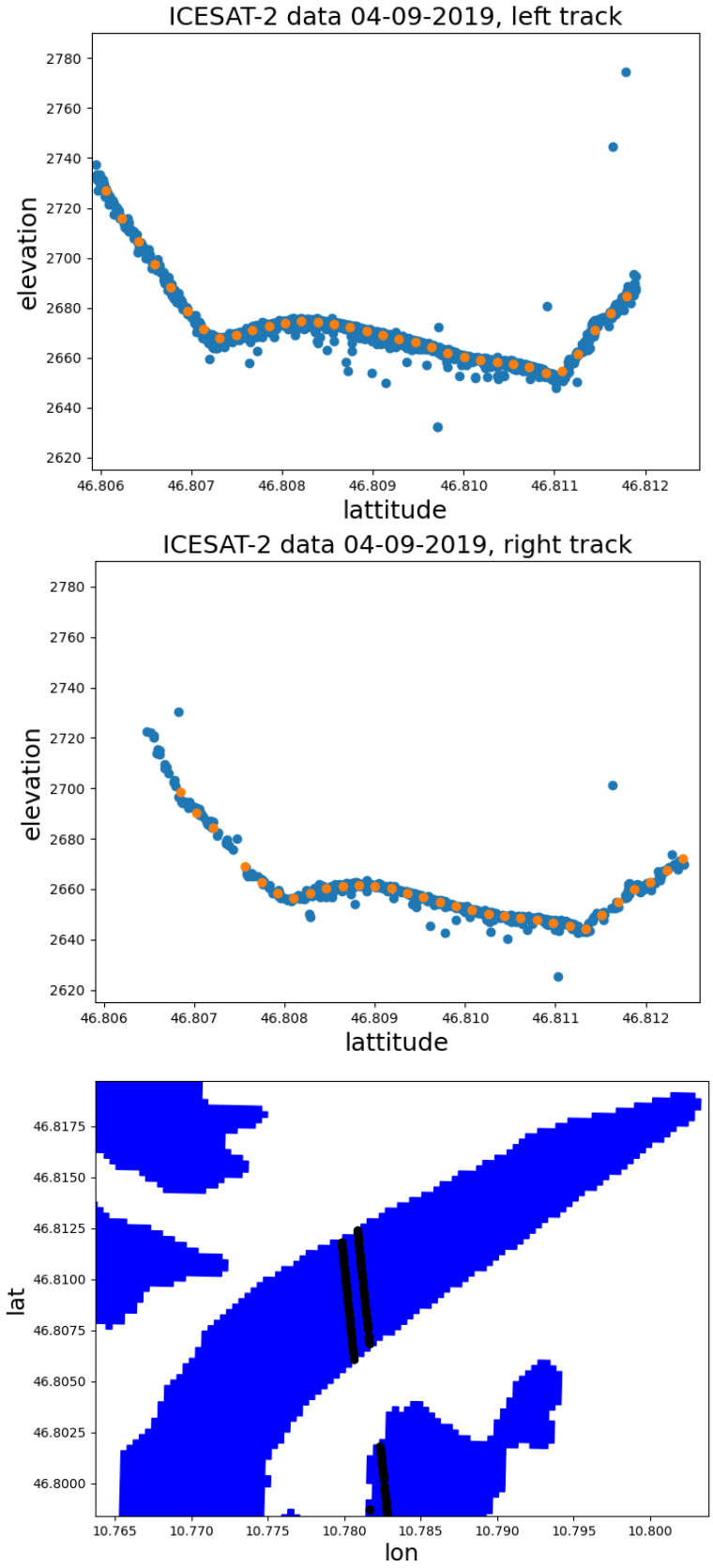

Figure 12: (a) ATL03 with quality flag 4 and ATL06 for the left strong beam, (b) ATL03 with quality flag 4 and ATL06 for the right weak beam, (c) location of the data on the Hintereisferner outline from RGI.

3.2 GEDI

An overview of the GEDI mission will be given here, followed by a description of the algorithms used to create the L1B and L2A data products.

3.2.1 Mission Overview

The Global Ecosystem Dynamics Investigation (GEDI) is a Lidar sensor that was launched in December 2018 and attached to the International Space Station. Its main objective is to observe Earth's forests vertical structure and by extent their biomass [57]. GEDI uses a full waveform Lidar to capture the height and density of vegetation. It splits three lasers into 8 ground tracks, spaced 600 meters apart in the cross-track direction. The beams have a footprint of approximately 30 meters, and samples are spaced 60 meters apart in the along-track direction.

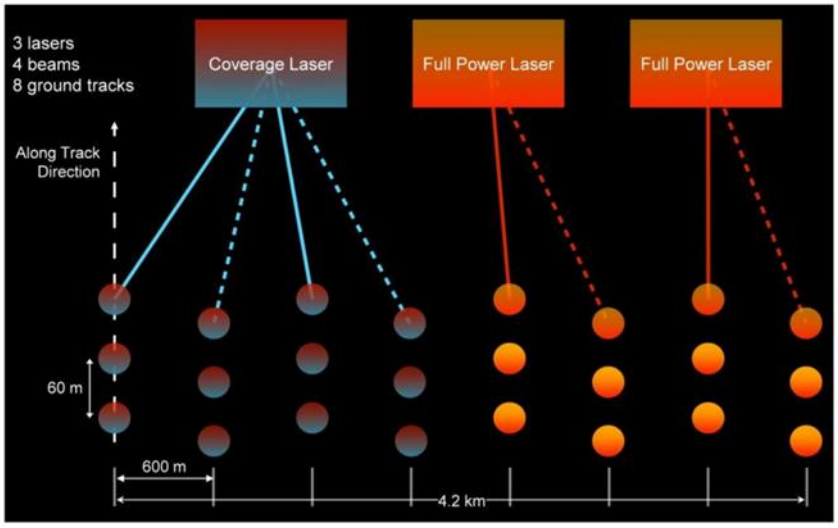

Figure 13: GEDI beam configuration [58]

GEDI data can be freely downloaded from the website of the Land Processes Distributed Active Archive Center (lpdaacsvc.cr.usgs.gov). The data products that will be used are L1B: 'Geolocated waveforms' and L2A: 'Ground elevation, canopy top height, relative height (RH) metrics'.

3.2.2 L1B Geolocated Waveforms

GEDI's full waveform technique means that it does not detect individual photons, but simply monitors the combined energy of all photons received from the surface. The return of the laser beam is easily detected over the background noise, and it is time tagged and passed on to the waveform processing and geolocation algorithms. In addition, the transmitted waveforms are also recorded and time tagged. The waveforms are recorded at a resolution of 1 ns, corresponding to a 0.15 m vertical resolution on the ground.

The L1B data product contains the geolocated waveforms. Since the waveforms are not necessarily perpendicular to the surface, the first and last bin of every waveform are geolocated, allowing the locations of any of the middle bins to be interpolated if necessary. The geolocation algorithm is described in [59].

The first step in the geolocation algorithm is to characterize the transmitted pulse, fitting a Gaussian curve and setting its centre as the start of the transmit time. This allows the time of the received pulse to be taken relative to the transmitted pulse, which is used to determine the range to the bounce point.

GEDI uses a combination of GPS and star tracking to determine its location and pointing. The location and pointing are used with the travel times of received waveform to determine the bounce point of the first and last waveform bin. The bounce points are converted from GEDI's inertial reference frame to the WGS84 system. The atmospheric path delay is then determined using the exact same method as described for ICESAT-2, which algorithmic basis document is also named as the source for GEDI [53].

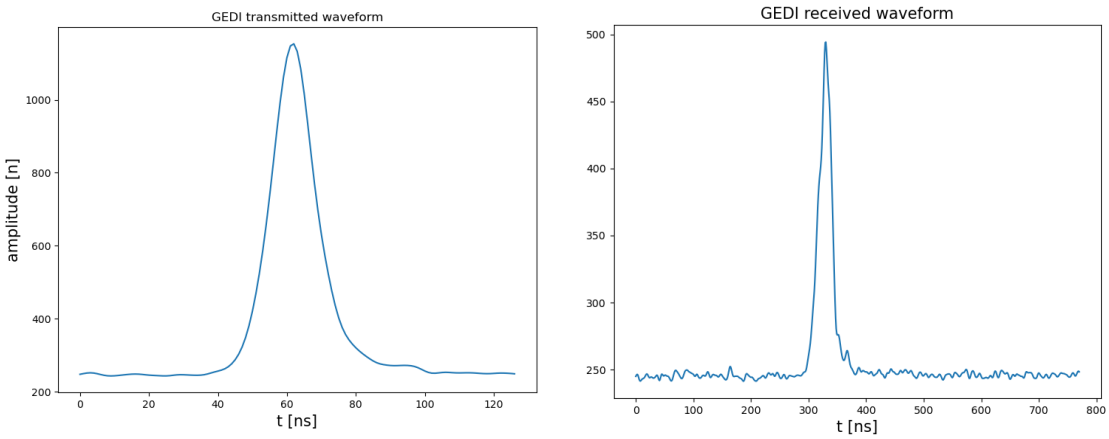

Figure 14: Example of GEDI (a) transmitted and (b) received waveforms

The L1B product dynamically estimates the uncertainty of its geolocation and height. The height error estimation ranges approximately between 0.2 and 0.8 meters and the horizontal errors range between approximately 2 and 11 meters.

Similarly to ICESAT-2, GEDI corrects for solid earth tides, ocean loading and geocenter motion by default and supplies the geoid height relative to the reference ellipsoid.

3.2.3 L2A Ground elevation, canopy top height, relative height (RH) metrics

The L2A data product contains the elevation of detected surface returns from the geolocated waveforms. It has the same 60 meter along track resolution as the L1B product.

GEDI was designed specifically for the determination of canopy heights relative to the terrain. Therefore, the algorithm for the L2A product determines not only the height of the terrain at the bounce point, but accounts for any number of surface returns above it.

The received waveform interpretation algorithm [60] starts by applying a convolution with a Gaussian curve for smoothing. The extent of all possible returns is then determined by taking the segment which is significantly above the background noise level. Inside of this extent, all locations where the first derivative of the smoothed curve passes zero are tagged as 'modes', which are possible surface returns. Figure 16 shows a sample of GEDI L2A data over the Hintereisferner.

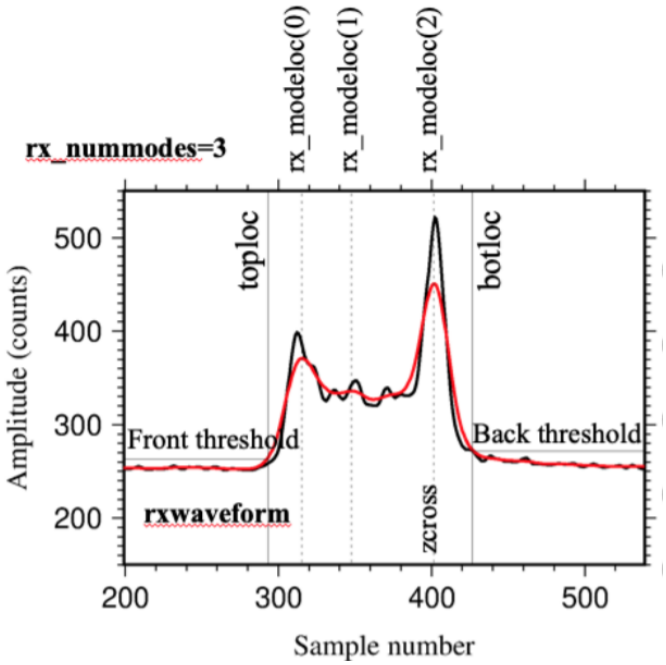

Figure 15: Visualisation of the mode detection algorithm described in [60]. The black line represents the original received waveform, which is smoothed to the red line. The toploc and botloc show the extent of the waveform for which modes are detected. Three modes have been detected in this example, shown as rx_modeloc(0), (1) and (2).

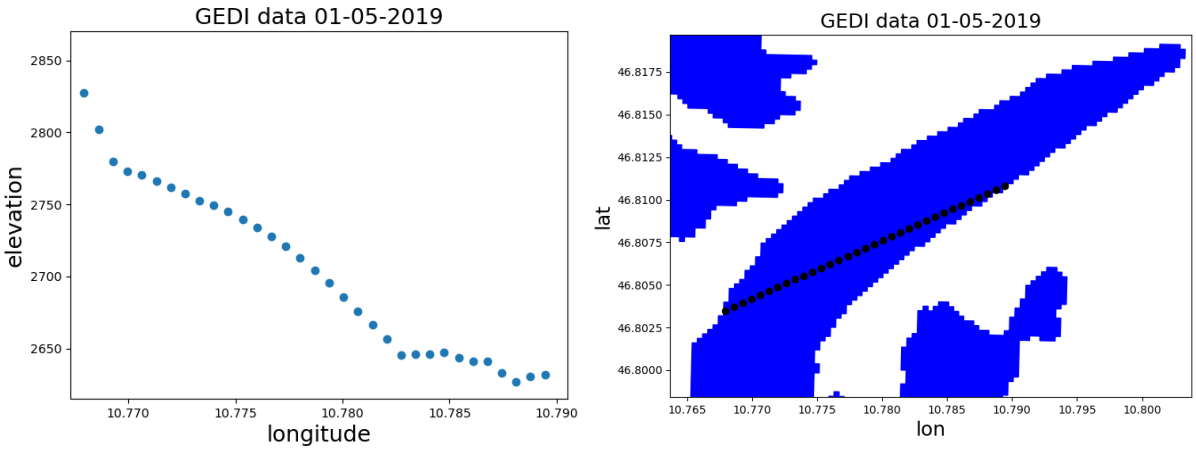

Figure 16: (a) example of an along-track segment of GEDI L2A data (b) Location of the data on the Hintereisferner outline from the RGI [52]

3.3 ICESAT-2 and GEDI coverage

ICESAT-2 occupies a near-polar retrograde orbit of 92 degrees. As a result, it visits practically all latitudes once per orbit. Through further careful design of its orbit, the ground tracks create a pattern on the Earth's surface. The distance between parallel ground tracks varies with latitude but is constant with longitude. Ground tracks at the equator are 28.8 km apart, while at 88 degrees latitude north or south they converge. At Austria's latitude of 47 degrees north this distance is 19.5 km. It takes ICESAT-2 91 days to cover the entire globe in this manner. The blue lines in Figure 17 show the ground track for the first 91 day period.

After 91 days ICESAT-2 repeats the same ground track from the start. For every one of these repeats, the ATLAS instrument is pointed to the side of the true ground track when it is above land surfaces outside of the polar regions. This has as an advantage that the spatial coverage of the total satellite mission is increased, but sacrifices the time series that would be created by an exact repeat. Figure 17 shows the pattern of ground tracks that is created after 8 repeats, which is to be finished on December 23, 2020. These parallel tracks are approximately 2.44 km apart. Every reference ground track represents 3 pairs of beams which are 3.3 km apart. This results in the pattern of ground tracks shown in figure 18, where parallel tracks are approximately 810 meters apart.

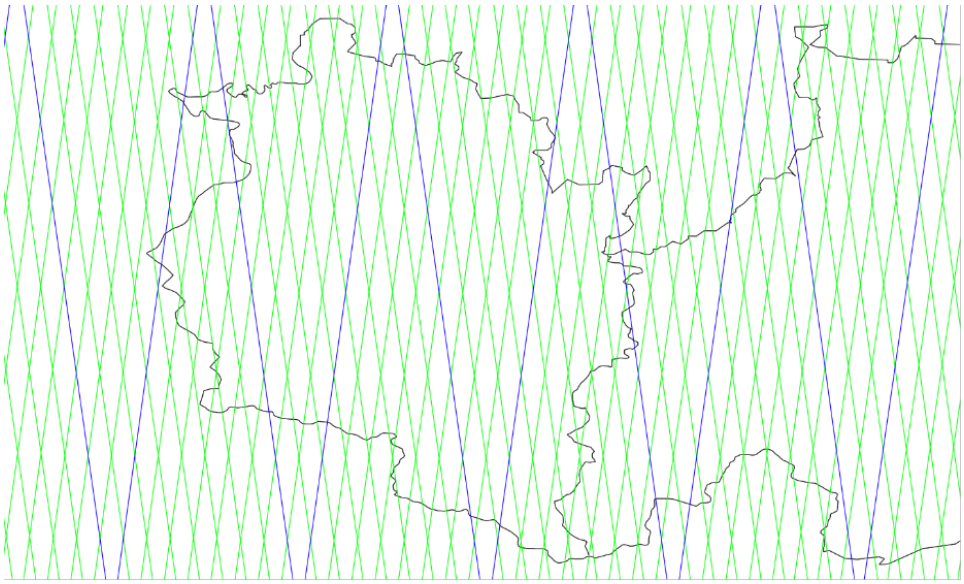

Figure 17: ICESAT-2 Reference Ground Tracks over the Austrian province of Vorarlberg. The first 91 day repeat is shown in blue and the subsequent 7 repeats with side-pointing of the ATLAS instrument are shown in green.

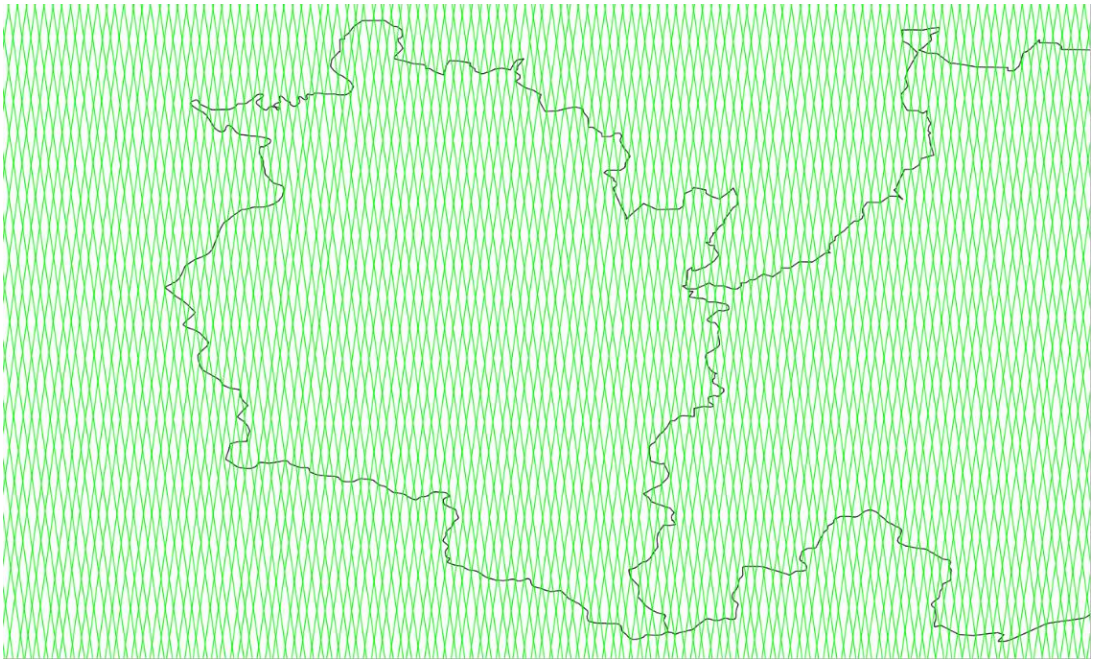

Figure 18: ICESAT-2 laser beam pair ground tracks over the Austrian province of Vorarlberg. Every track represents 2 laser beams which are 90 meters apart.

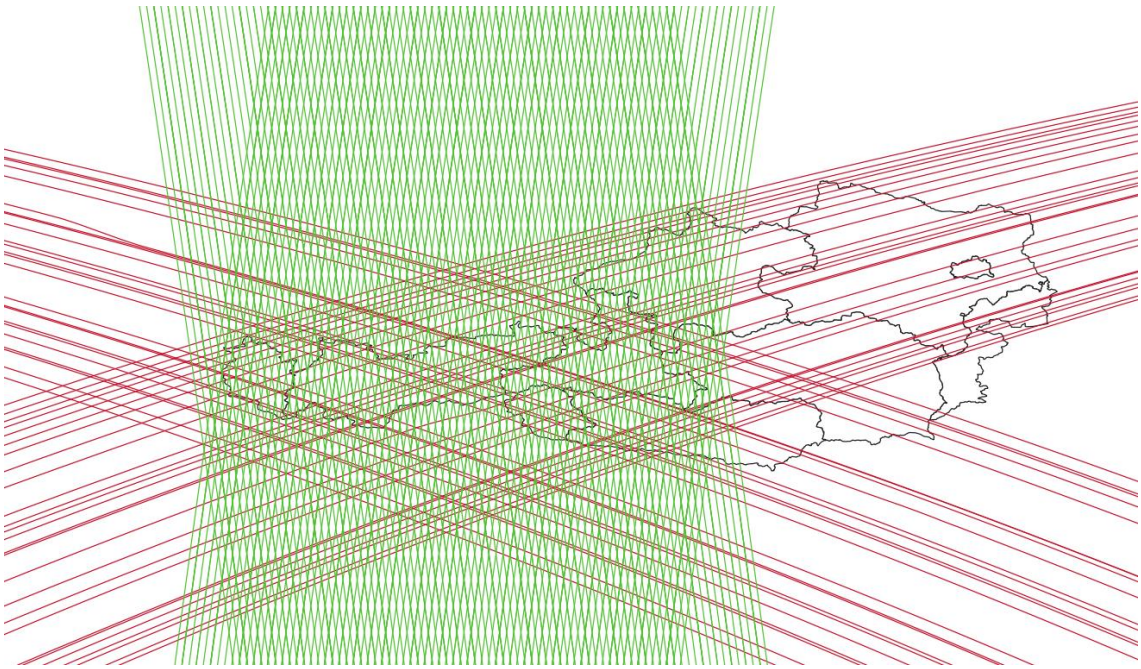

Figure 19: All reference ground tracks of ICESAT-2 (green) and all ground tracks of GEDI available when the data was retrieved (red). Only the tracks that cross the general area of Austria containing glaciers are used. Note that every ICESAT-2 or GEDI ground track represents 6 and 8 laser beam ground tracks respectively.

GEDI is attached to the ISS, which has an orbital inclination of 51.64 degrees. This is much lower than that of ICESAT-2, meaning that GEDI's ground tracks do not cross Greenland and Antarctica, as well as some other regions with significant glacial masses, such as Alaska, the most southern parts of Patagonia, Scandinavia and the numerous arctic archipelagos. Because GEDI is dependent on the ISS orbit, it samples the Earth's surface more irregularly, as shown in figure 19. GEDI does have the

capability of pointing to the side of the ISS ground track by 40 km. GEDI does not provide reference ground tracks for its future data like ICESAT-2.

ICESAT-2 was launched on September 15th 2018 and its earliest available data is from October 13th. Its nominal mission duration is 3 years, meaning the scheduled deactivation is in the autumn of 2021, although it may remain active for longer. GEDI was launched to the ISS on December 5th 2018 and collected its first data on April 19th. Its mission duration is 2 years, and it is planned to collect its final data in the spring of 2021.

4. Methodology

This chapter describes how ICESAT-2 and GEDI data is used to determine the elevation changes of Austrian glaciers, how these changes will be correlated with certain features and how cokriging will be used to give an estimate of the total ice loss in Austria.

4.1 Glacier Height Changes

To determine the ice loss in the Austrian glaciers, the height measurements from ICESAT-2 and GEDI need to be compared against a Digital Elevation Model (DEM) that contains the elevations of the glaciers at some moment in the past. An airborne lidar DEM with a resolution of 5 meters is available for the state of Tirol while the rest of the country is available at a resolution of 10 meters. These can be downloaded from the Austrian government's open data website, [61] [62].

The datasets have all been created from the same original point cloud which had a horizontal accuracy of 0.3 m and a vertical accuracy of 0.15 m. The resolution in the mountainous areas was at least 1 point per $4m^2$ and the flat, low areas had a resolution of at least 8 points per m^2. A ground filter classification was applied and the dataset was rasterized initially at 1m resolution, interpolating for any locations without data.

The DEM's are available in the EPSG:31255 Cartesian reference system of Austria. The elevation of the models is relative to the geoid.

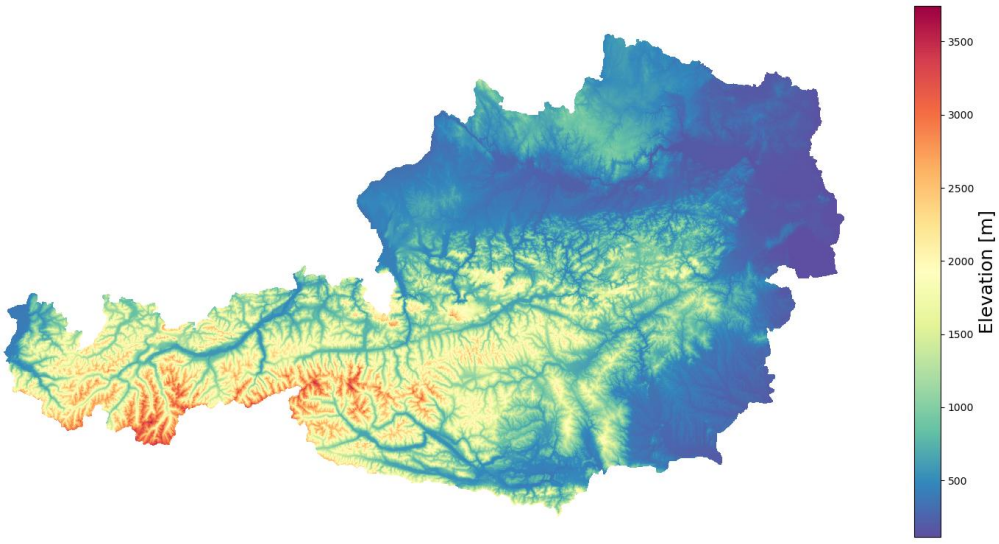

Figure 20: DEM of Austria [62]

The creation of a nationwide airborne DEM such as this takes multiple years. The original data of the DEM was collected between 2006 and 2017 depending on the location. Therefore, some of the results will represent longer timeseries than others. Figure 21 gives an overview of the age of the DEM for Austria. Figure 22 shows the same information in more detail for the province of Tyrol, including the Ötztal region shown in blue, which was collected entirely in the year 2010. The Ötztal contains many major glaciers (including the Hintereisferner, Gepatschferner and Kesselwandferner), and other studies have estimated the ice mass loss here before [22] [63], making it suitable for a

comparison. The black hatched area in figure 22 that includes the Ötztal was remeasured in 2017 and 2018, but that data is not used in this analysis.

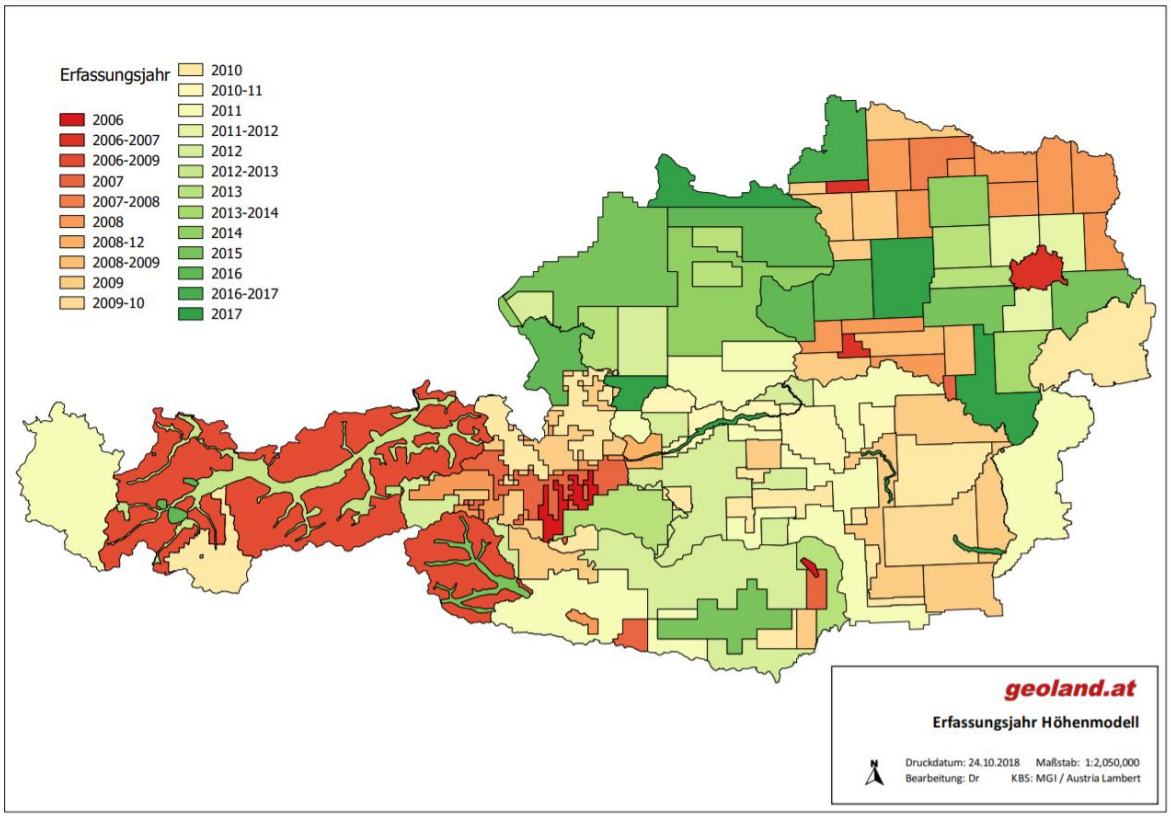

Figure 21: Age of the Austrian Digital Elevation Model

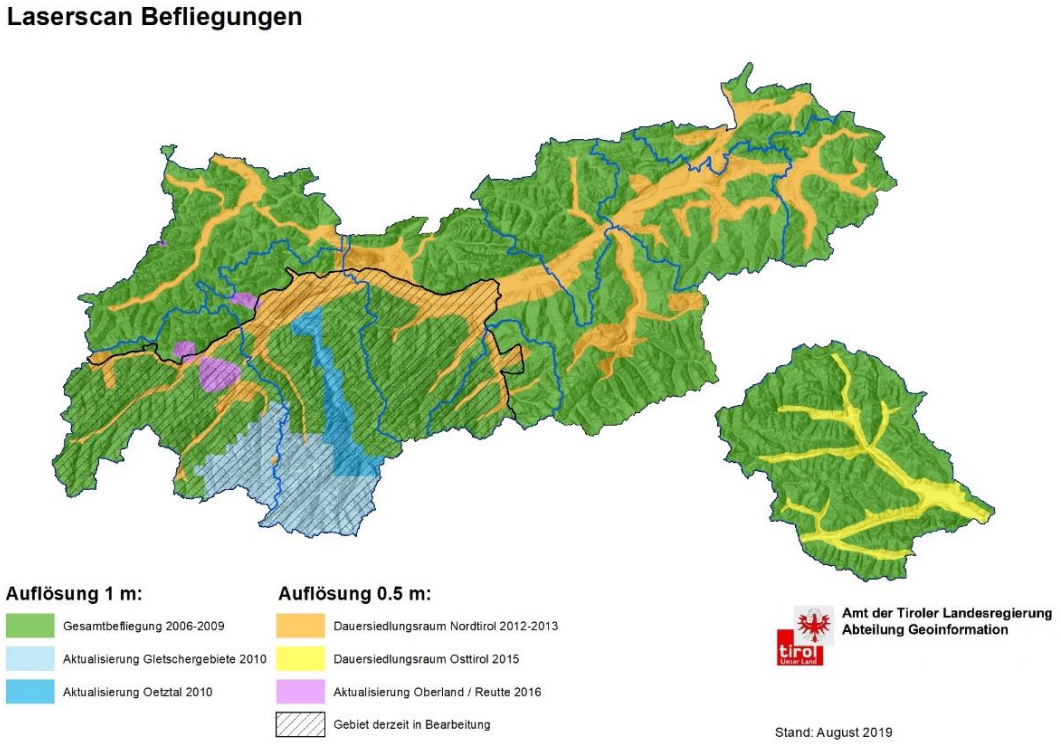

Figure 22: Age of the digital elevation model in Tirol [64] with the Ötztal region shown in blue

Whether an ICESAT-2 or GEDI datapoint belongs to a glacier cannot be seen from the data itself. Surface masks for land ice are available in the data, as described in chapter 3.1.4, however these are meant to clip the data to the approximate relevant region and are not precise enough on a smaller scale.

To perform this task, an inventory of glacier outlines is needed. One such database is the Randolph Glacier Inventory (RGI) that was also used to create the land ice surface masks for ICESAT-2 as mentioned in chapter 3.1.4. [52]. The RGI aims to describe the outline of glaciers in as narrow a time span as possible, near the start of the 21st century. The glaciers in Central Europe specifically have been created from Landsat 7 imagery taken in the summer of 2003. A new glacier inventory was created by Paul et al. (2020) using Sentinel-2 imagery from the year 2015 [65]. This inventory is used for the analysis in this thesis. Figure 23 shows the locations of all these glaciers in Austria.

Comparing these two datasets shows that the total glacier area in Austria has shrunk from 389.78 km^2 to 379.93 km^2, or a decrease of 2.5%. Figure 24 shows the outline of the Hintereisferner from the 2003 RGI and the 2015 inventory by Paul et al. in Google Earth. The shrinkage is clearly visible, but the new inventory outlines are already outdated when compared with the Google Earth imagery from the year 2020.

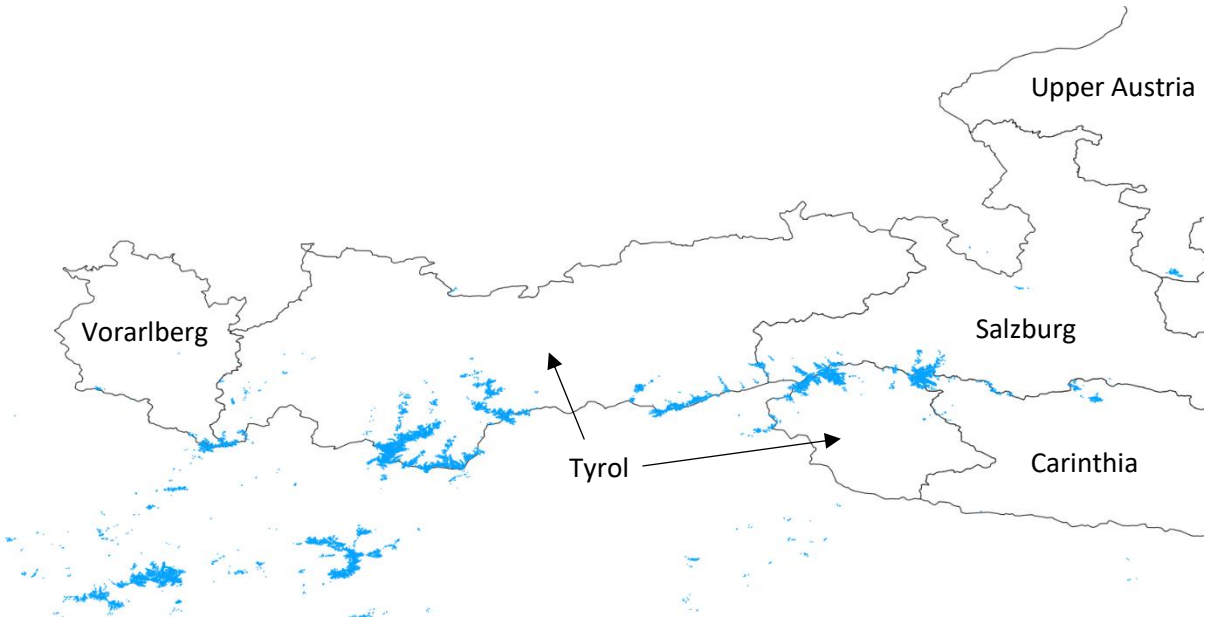

Figure 23: Glacier outlines of the glacier inventory created by Paul et al. (2020) over Austria [65]. Glaciers shown in Northern Italy are not included in the analysis.

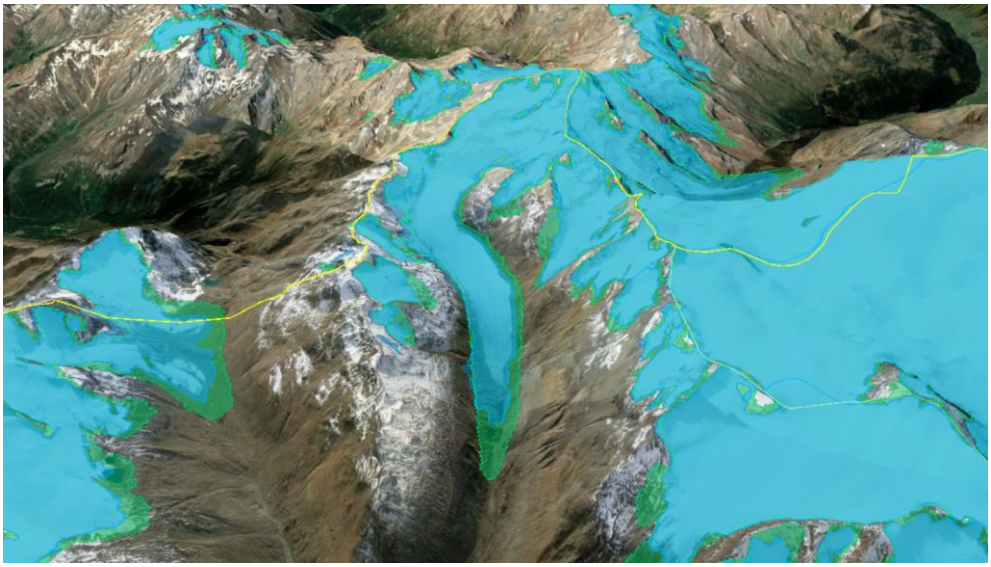

Figure 24: Glacier outline of the Hintereisferner for the year 2003 from the Randolph Glacier Inventory (green) and for the year 2015 from Paul et al. (blue) in Google Earth.

At the time of downloading, ICESAT-2 data was available from 16-10-2018 to 12-11-2019, and GEDI data was available for 18-04-2019 to 10-07-2019. All datasets were downloaded for a bounding box of latitude 46.6 – 47.6 and longitude 9.5 – 14.0, corresponding roughly to the area of Austria containing glaciers. 148 datasets were available for ICESAT-2 and 50 for GEDI, each dataset corresponding to a single crossing of the satellite over Austria. Approximately a third of these datasets contain data that lies on the glacier and is of sufficient quality.

A script was made to loop over all ATL06 and L2A datasets. In this loop, the location, height and quality parameters were collected and filtered to the bounding box of the country of Austria. For ICESAT-2 ATL03 data only the photons with a confidence flag corresponding to a surface return (2,3 or 4) were used. For GEDI the lowest detected return of the waveform was taken as the surface height. A more detailed filter was then performed for every point to get only the data that lies on the glaciers. Figure 25 shows all data over the Ötztal region as an example.

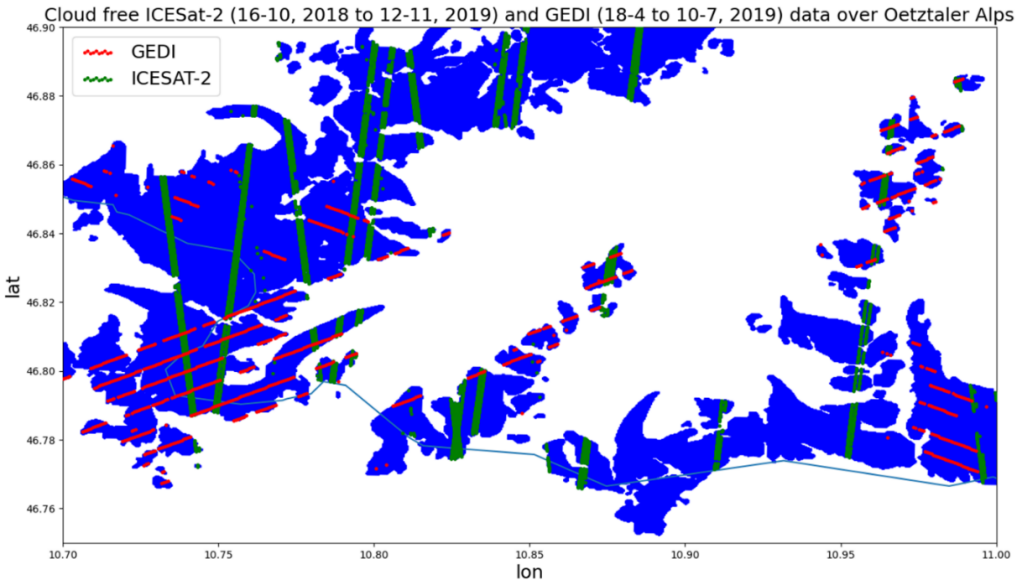

Figure 25: ICESAT-2 ATL06 and GEDI L2A data location

In order to compare the heights from the altimeters with the digital elevation models they need to be converted from ellipsoidal height to geoid height. Both ATL06 and L2A give the height of the geoid relative to the ellipsoid for every data point, making this conversion simple.

The digital elevation models were converted from the local Austrian reference system to the longitude, latitude system of WGS84 in QGIS. They were also clipped roughly to the areas containing glaciers in order to save memory.

For any location of the data points, the height from the DEM could be taken as simply the height of the pixel that data point is located in. This would correspond to a nearest neighbour method of selecting the DEM height. However, this would be suboptimal since it would assume that within a pixel of 10 by 10 or 5 by 5 meters the terrain is perfectly flat. Instead, a bilinear interpolation method was chosen based on the four closest pixels in the DEM [66]. As shown in figure 26, this method first interpolates linearly the top two pixels and bottom two pixels horizontally to the longitude of point p, and then interpolates linearly those two values to the latitude of point p. This takes into account the local slope described by the four pixels and should result in a more realistic DEM value at the data point locations.

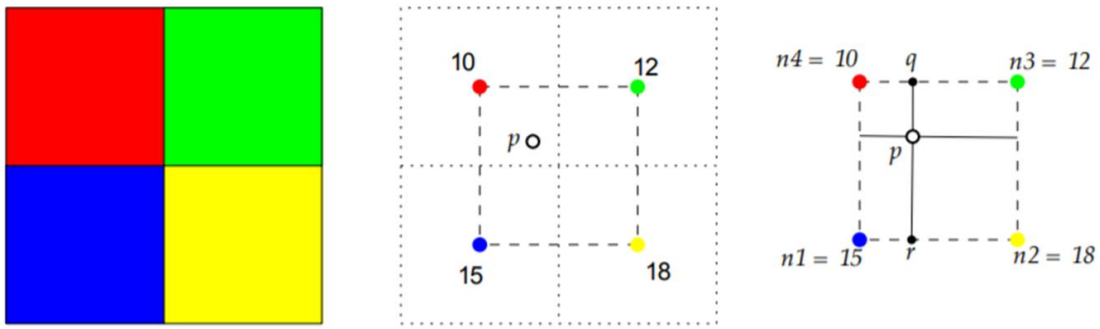

Figure 26: Bilinear interpolation [66]

4.2 Feature Correlation

The height changes due to ice loss can differ greatly between locations within a single glacier. By its nature spaceborne lidar data needs to be extrapolated to gain a complete image of the mass loss. This can be done based purely on the observations themselves, but including features of the extrapolation location itself could create a more realistic result, especially when examining individual glaciers. For this purpose, features have to be created for every glacier location, and their correlation with the observations should be examined.

The elevation of the glacier location is expected to have by far the largest correlation with glacier height changes. Accumulation zones at high altitudes are expected to have little to no mass loss, while low lying valley glaciers have been observed to shrink rapidly.

The distance to the edge of the glacier of a point may be another useful feature. The glacier extent may have shrunk considerably since the creation of the glacier outlines, and more generally points near the edge may have a different rate of thinning. The glacier outlines are divided into smaller sections in cases where multiple glacier tongues come from the same continuous accumulation zone, which allows the glaciers to be analysed separately. However, for the calculation of the distance to the glacier edge the shapes were dissolved.

The local slope could potentially add information about the potential ice loss as it adds information about the structure of the glacier, although it may also simply express the differences in slope between valley glaciers and accumulation zones, which can be more accurately captured by the elevation comparison. The slope was calculated based on the Austrian DEM using QGIS. QGIS calculates the slope for every pixel by fitting a plane with least squares through its eight surrounding pixels.

The aspect is the orientation of the slope relative to the north direction. In the Alpes, slopes pointing north will generally have less sun hours than those pointing south, so it may be expected that they are more susceptible to melting. The aspect was also computed in QGIS based on the Austrian DEM.

In addition to the features presented in this thesis, many other features could potentially add more information, including surface roughness, sun hours and glacier colour.

4.3 Ordinary Cokriging

Since spaceborne lidar observations are limited to thin profiles of the surface, some sort of extrapolation is required to arrive at an estimate of the volume change of the glaciers in the study area.

The simplest method to do this is to take the average of the glacier height differences, and multiply it by the total glacier area. This assumes that the study area is well represented by the observations. The major factor influencing differences in glacier height changes within an area is the altitude of the glacier. Therefore, in order for the lidar data to be well representative of the study area, the distribution of the elevations of the observations should be similar to that of the distribution of elevations of the total area. Since the location of lidar data with regards to the terrain is essentially random, this should generally be true if a large amount of data is gathered over a large enough area. Kaab [26] and Gardner [7] use this method.

A downside of this method is that it does not give much insight into the spatial distribution of the mass loss. An alternative method is cokriging, which incorporates the correlation of the DEM with the glacier height differences. The datasets are partially heterotopic, meaning that all lidar datapoints have an associated DEM elevation, but most DEM locations do not have any associated lidar data. Therefore the much denser DEM data can be used to improve the estimate of the glacier height differences for points at further distances from the observations. All kriging methods are based on covariance functions of the observations, which describe how much a variable can be expected to change when moving a certain distance. To visualise the covariance functions variograms are created, which plot the distance between observations against their variance. Cokriging then assigns weights to all observations based on their distance to the cokriging location and the corresponding variograms. In the context of this research, weights are assigned to every lidar observation and DEM pixel in the neighbourhood of the cokriging location.

$$\hat{X}(u_0) = \sum_{i=1}^{n} \lambda_i X(u_i) + \sum_{j=1}^{m} w_j Y(v_j) \tag{3}$$

X represents the primary variable (the glacier height change) and Y represents the secondary variable (the DEM elevation). There are n observations of the primary variable and m observations of the secondary variable, and the same number of weights, represented by λ_i and w_j. The locations of the primary and secondary variable observations are represented by u and v respectively, and u_0 is the location for which cokriging is performed. These weights have to be determined for every location where cokriging is required.

Two constraints are placed on the weights. The sum of all primary variable observation weights λ should be 1 and the sum of all secondary observation weights w should be 0, to ensure that the average estimation error should be zero and the secondary variable does not introduce a bias with regard to the estimated first variable [67]. The values of the weights can be found by the equation:

$$\boldsymbol{\lambda} = \boldsymbol{Q}^{-1}\boldsymbol{Q_0} \tag{4}$$

Lambda represents both the primary and secondary variable weights, as well as two Lagrange multipliers. Matrix **Q** contains the variogram values for the distances between all observations, and likewise $\mathbf{Q_0}$ contains the variogram values for all distances from the cokriging location to the

observations. The variogram values essentially indicate how much the value of a variable is likely to differ from an observation, given the distance to that observation.

$$\boldsymbol{\lambda} = \begin{pmatrix} \lambda_1 \\ \vdots \\ \lambda_n \\ w_1 \\ \vdots \\ w_m \\ L_1 \\ L_2 \end{pmatrix}, \quad \boldsymbol{Q} = \begin{pmatrix} \boldsymbol{G_{xx}} & \boldsymbol{G_{xy}} & 1 & 0 \\ \boldsymbol{G_{yx}} & \boldsymbol{G_{yy}} & 0 & 1 \\ 1 & 0 & 0 & 0 \\ 0 & 1 & 0 & 0 \end{pmatrix}, \quad \boldsymbol{Q_0} = \begin{pmatrix} \boldsymbol{G_{x0}} \\ \boldsymbol{G_{y0}} \\ 1 \\ 0 \end{pmatrix} \tag{5}$$

Matrix **Q** is split into $\mathbf{G_{xx}}$ for the primary variable, $\mathbf{G_{yy}}$ for the secondary variable, and $\mathbf{G_{xy}}$ and $\mathbf{G_{yx}}$ for the cross-variograms. Likewise Q_0 has a component for the primary and secondary variable.

$$\boldsymbol{G_{xx}} = \begin{pmatrix} \gamma_x(u_1 - u_1) & \cdots & \gamma_x(u_1 - u_n) \\ \vdots & \ddots & \vdots \\ \gamma_x(u_n - u_1) & \cdots & \gamma_x(u_n - u_n) \end{pmatrix} \tag{6}$$

$$\boldsymbol{G_{xy}} = \begin{pmatrix} \gamma_{xy}(u_1 - v_1) & \cdots & \gamma_{xy}(u_1 - v_m) \\ \vdots & \ddots & \vdots \\ \gamma_{xy}(u_n - v_1) & \cdots & \gamma_{xy}(u_n - v_m) \end{pmatrix}$$

$$\boldsymbol{G_{x0}} = \begin{pmatrix} \gamma_x(u_1 - u_0) \\ \vdots \\ \gamma_x(u_n - u_0) \end{pmatrix}$$

The variograms of the primary and secondary variables are represented by γ_x and γ_y, while γ_{xy} represents the cross-variogram between the two variables. The cross-variogram matrices $\mathbf{G_{xy}}$ and $\mathbf{G_{yx}}$ contain the same values but are mirrored, so the matrix **Q** is always symmetrical around the diagonal. In order to determine the input values for these matrices, experimental variograms are created and theoretical variograms are fitted to these.

To start the construction of the experimental variograms the observations of both the glacier height differences and the DEM are normalized by subtracting their mean and dividing by their standard deviation, ensuring that the scale of their units does not affect the cokriging result.

For every pair of observations the distance between points is determined and their semivariance is calculated. The semivariance is defined as the difference squared and halved. Figure 27 shows in red the average semivariance per distance bin of 20 meters for the glacier height difference observations. A theoretical variogram was fitted to this curve. All theoretical variograms are described by three variables: the sill, which is the maximum semivariance that is reached at large distances from an observation; the range, which is the distance from an observation at which the sill is reached; and the nugget, which is the minimum semivariance at close distance to an observation (although the variogram value at zero distance is still defined as zero). For the glacier height differences variogram an exponential variogram was fitted, with a nugget of 0.13, a sill of 0.9 and a range of 2500 meters. For the cross-variogram a Gaussian curve was fitted, with a sill of 0.48, a range of 4800 meters and without a nugget. For the DEM variogram a Gaussian curve was used as well, with a sill of 1 and a range of 4000 meters, also without a nugget.

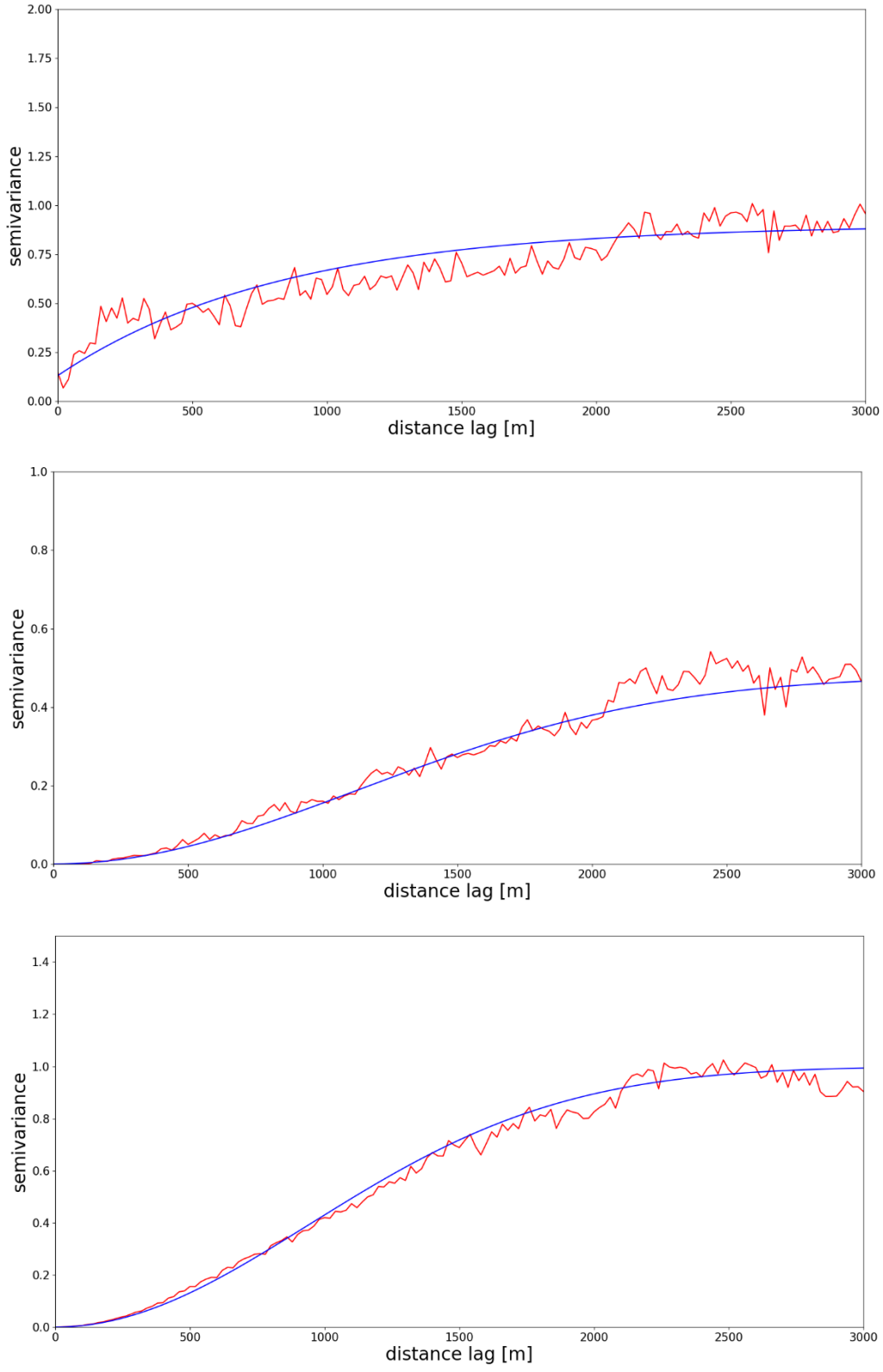

Figure 27: experimental variograms in red and theoretical variograms in blue of (a) the glacier height differences (b) cross-variogram of the glacier height differences and the DEM (c) the DEM

Given the grid resolution of cokriging location the area each pixel represents is known. To determine the volume difference the cokriging glacier height difference was multiplied by this area for every point. The glacier ice density can be used to estimate the resulting mass difference, but it is variable and generally unknown for most glaciers. Most studies therefore opt to take a constant ice density, of either 850 or 900 kg/m^3 [7] [19] [68] [21] [22]. For consistency, an ice density of 850 kg/m^3 will be used here, though this will be adjusted when results are compared with studies that use a different value.

Cross-validation will be performed to estimate the accuracy of the cokriging procedure. For every glacier crossed by multiple tracks one of the tracks is removed and cokriging is performed at all of its datapoint locations using the remaining tracks. The cokriging results were then subtracted from the true values of the datapoints to give the error of the height difference. This error can then be converted to a mass error using the set grid resolution and ice density.

The total glacier mass difference over Austria is calculated by summing the mass difference of every pixel. The uncertainty of the total mass difference due to the cokriging accuracy can then be found by using formula 7.

$$\sigma_{cokriging} = \sqrt{N} * \sigma_{pixel} \quad (7)$$

Where N is the total amount of pixels and σ_{pixel} is the mass uncertainty of a pixel.

In this research, the local height change will be estimated for every cell in a 25 m grid for every glacier which area contains spaceborne lidar observations, using the cokriging procedure and variograms described here. Based on these results the total mass change will also be computed for every such glacier, as well as the Ötztal region and the whole of Austria. The estimates for the Ötztal and Austria will also be compared against the method of simply applying the average height change.

5. Accuracy Assessment

In this chapter the accuracy of glacier surface height changes from a comparison between the Austrian DEM and ICESAT-2 or GEDI data will be examined.

5.1 Methodology

In order to examine how well the surface heights determined by ICESAT-2 and GEDI correspond to the DEM, they were compared at locations outside of the glacier outlines. There are many processes that could cause a change in surface height at any location, but it is assumed that the average elevation will not change significantly, and that for the vast majority of locations the elevation change will be small. Therefore, the height differences between the reference DEM and the spaceborne altimetry data give information about the accuracy of the method. The exception to this may be the change caused by seasonal variations, such as vegetation height and snow cover. It is not known at what time of year the DEM was collected, so this is not corrected for, which may lead to an underestimation of the accuracy. Any variation in the terrain below the DEM resolution captured by the high resolution ATL03 will also contribute to the measured errors.

No distinguishment can be made directly between what part of the errors is due to the space altimetry data and what part is due to the DEM. However, it is expected that both ICESAT-2 and GEDI will have a worse accuracy than the DEM, since the original pointcloud of the DEM had a vertical accuracy of 0.15 m and because airborne lidar in general can usually achieve an accuracy in the order of decimeters [69]. The rasterization of the point cloud may have reduced the accuracy, but it will still be in the same order of magnitude.

In order to reduce processing times and to restrict the accuracy assessment to the relevant terrain the DEM was cropped roughly to the areas containing glaciers, as shown in figure 28. All available altimetry data located outside of the glacier outlines but within these areas was used.

Figure 28: DEM cropped to the relevant areas

The datasets contain a small number of large outliers of up to thousands of meters, which has a large effect on its standard deviation. To give a more robust measure of the dispersion the Median Absolute Deviation (MAD) was used:

$$MAD = median(|\Delta h_j - m_{\Delta h}|) \quad (8)$$

Where Δh_j corresponds to all individual height differences and $m_{\Delta h}$ is the median of all the individual height differences. [70]

As described in chapter 3.1.4, the horizontal geolocation error is expected to be much larger than the vertical error, and therefore a large part of the errors is expected to be due to a horizontal error in a sloped area. For an equal horizontal error, the vertical error will be larger for an area with a steep slope than for an area which is relatively flat.

To investigate this effect, a slope map was created from the DEM in QGIS. QGIS calculates the slope for every pixel by fitting a plane with least squares through its eight surrounding pixels.

A slope value was then added to every datapoint, using the same bilinear interpolation method described in chapter 4.1. All observations were grouped by their slope in bins of 1 degree, and the MAD was calculated for every bin.

For areas with terrain slopes near zero the errors are expected to be smallest, and these errors will show the vertical accuracy of the method. The decrease in the accuracy as the slope increases will be mostly due to the horizontal error. Assuming the slope will be linear locally, the relation between the observed error and the slope will be:

$$e_{v,obs} = \tan(\theta) * e_h + e_v \quad (9)$$

Where $e_{v,obs}$ is the observed error between the spaceborne altimetry data and the DEM, θ is the terrain slope, e_h is the horizontal geolocation error and e_v is the vertical geolocation error. This relation can be fitted to the observed errors to find the vertical and horizontal components of the error.

The terrain slopes found on glaciers is expected to be lower on average than those in the mountainous off-glacier areas. Since the accuracy depends on the slope, the average off-glacier accuracy will therefore be worse than it will be on-glacier. The accuracy value is therefore finally calculated by weighting the off-glacier accuracy for any slope value by the frequency of that slope within the glacier outlines.

5.2 Results

Accuracy assessment was performed for ICESAT-2 ATL03, ATL06 and GEDI L2a. The two ICESAT-2 data products were examined separately, since it is expected that ATL06 will have a better accuracy than ATL03 as a result of essentially averaging the high resolution spread of photons.

5.2.1 ATL03

For the ATL03 data, only the photons which are expected to correspond to surface reflections were used. These are the photons with quality flags 2,3 and 4, which respectively low, medium and high confidence.

Figure 29 shows the histogram of height differences between the DEM and ATL03 data. The statistical parameters are summarised in Table 3.

Assuming that the change of elevation in the area will be zero on average, the median of the highest quality photons shows a small positive systematic error in the differences of 0.65 m. The systematic error is increased for lower quality photons to 1.16 m and 1.60 m.

The MAD shows the random error in the data, and likewise the MAD is highest for the highest quality photons. The high and medium quality photons have an MAD of 2.17 m and 2.67 m. However, the lowest quality photons have a significantly worse value of 5.93 m. The low quality photons represent 32.0 % of the data, but including them will have a negative effect on both the systematic and random error of the data.

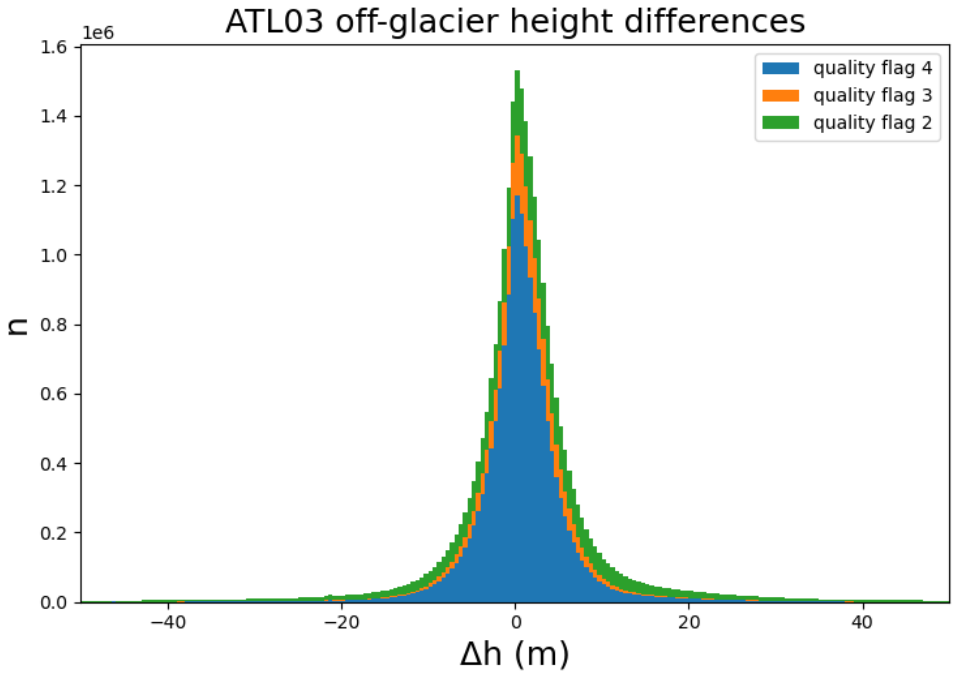

Figure 29: Histogram of height differences between the DEM and ICESAT-2 ATL03 measurements for quality flags 2,3 and 4.

	Mean [m]	Median [m]	Std [m]	MAD [m]	Weighted MAD [m]
QF=4	0.79	0.65	5.88	2.17	1.89
QF=3	1.16	1.16	6.14	2.67	2.25
QF=2	2.01	1.60	22.33	5.93	4.50
QF=3,4	0.85	0.72	5.92	2.25	1.94
QF = 2,3,4	1.15	0.83	12.38	2.76	2.23

Table 3: Accuracy parameters of the ATL03 to DEM height differences, for high (4), medium (3) and low (2) quality flags, a combination of high and medium quality flags (3,4) and all available surface photons (2,3,4)

The MAD was calculated for every slope bin, and plotted in black in figure 30a. The number of points per bin is shown in figure 30b. As expected the vertical accuracy is best in flat areas, with an MAD of only 0.41 m. It then increases gradually and reaches a value of 5 meters at 54 degrees and 10 meters at 68 degrees. The plot becomes erratic at slopes steeper than 70 degrees, due to the small sample sizes of the bins. Formula 9 was fitted to the graph, as shown by the red line. Only the values up to 50 degrees were considered, as this is where the vast majority of data lies. This fit corresponds to a horizontal accuracy of 3.41 m.

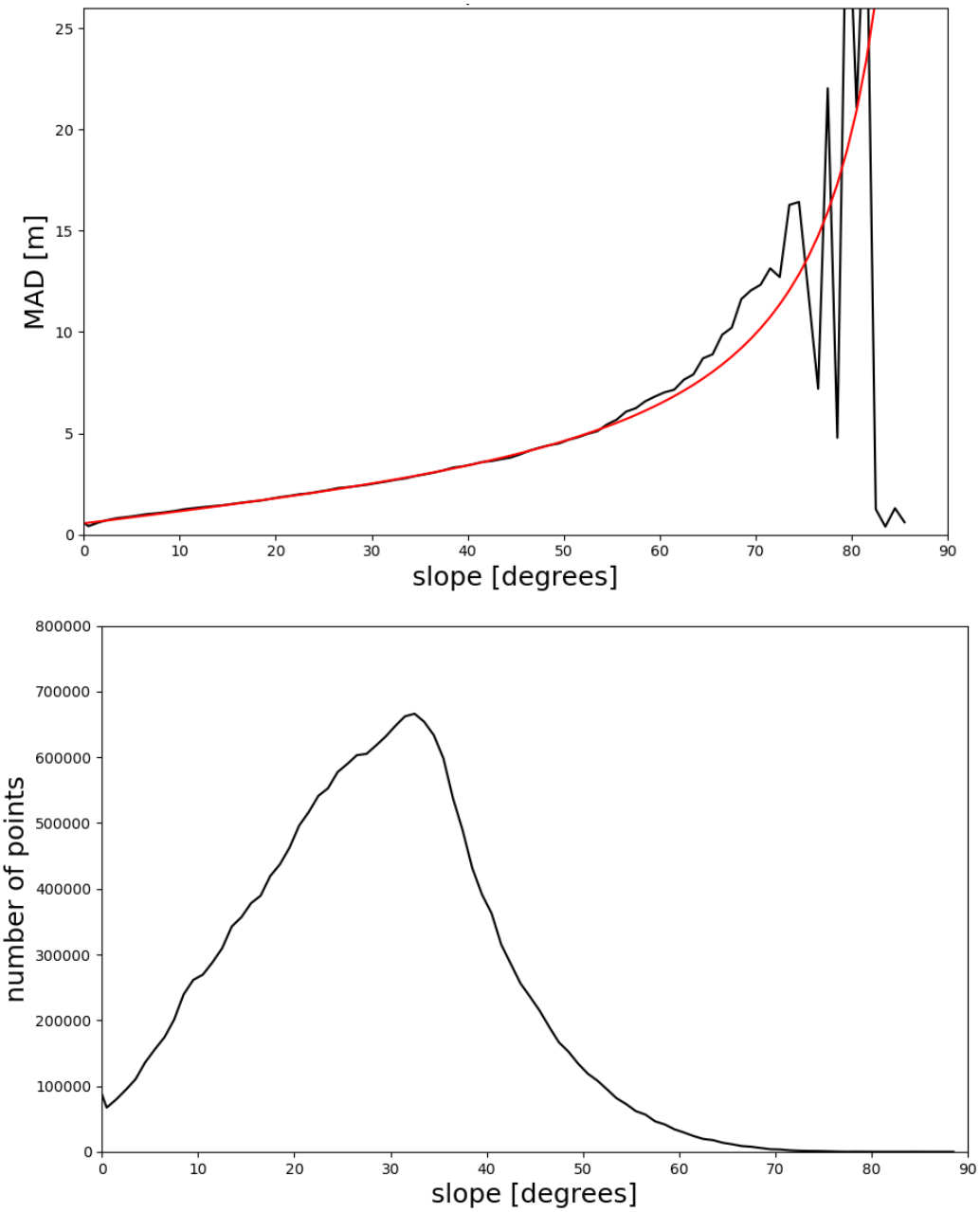

Figure 30: (a) ATL03 Median Absolute Deviation vs slope of the reference DEM (b) Number of points per bin vs slope of the reference DEM

Figure 31 shows the histogram of slope gradients located on glaciers, with values on average significantly lower than off-glacier locations. Weighting the above found accuracy with the frequency of the slope values on-glacier results in a lower MAD of 1.94 m.

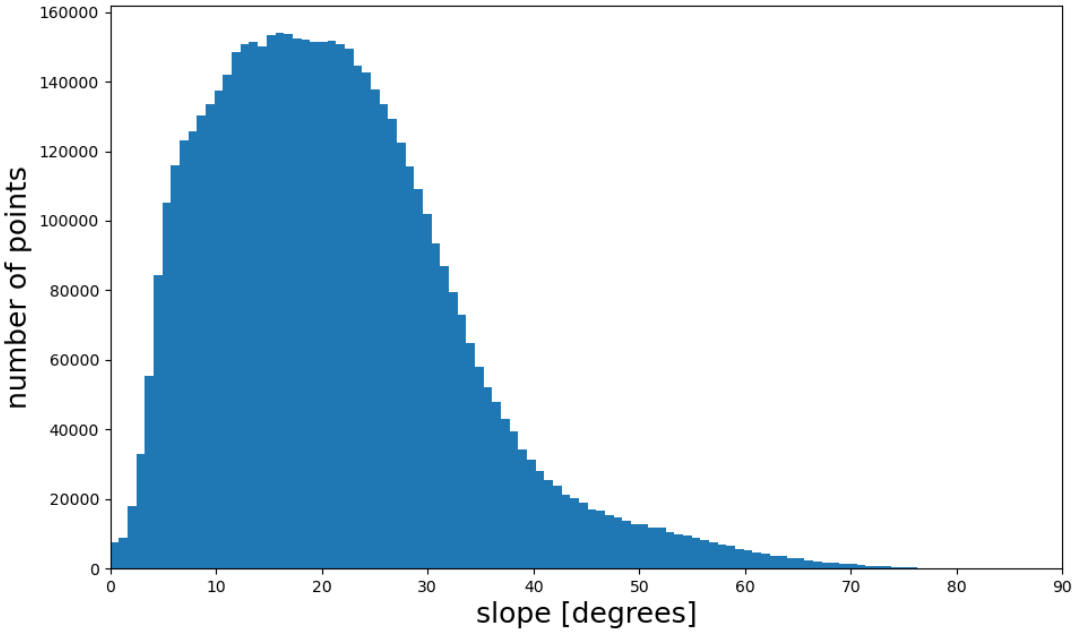

Figure 31: Histogram of slope values based on the airborne DEM found within the glacier outlines in Austria.

5.2.2 ATL06

Figure 32a shows a histogram of all ATL06 heights relative to the DEM outside the glaciers, and table 4 shows the statistical parameters of the height differences. Both the systematic and random error are slightly lower than that of the highest quality ATL03 photons. This is because for any 20 meter segment the spread of photons is reduced to a single point.

The same method as for ATL03 was used to inspect the influence of the slope on the accuracy, shown in figure 33a. The observed relation is very similar as the MAD is 0.21 m for flat areas and crosses 5 m at 53 degrees. The main difference is that the sample size of areas with steep slopes is relatively low compared to ATL03, which causes the MAD graph to become chaotic at slopes larger than 55 degrees. This is potentially caused by the surface detection algorithm of ATL06 (as described in chapter 3.1.5.) having more issues with steep or rough terrain. An advantage of using the raw ATL03 photons could therefore be that it provides more data for these terrain types.

The increase of the error shown in figure 33 corresponds to a horizontal error of approximately 3.41 m, the same as that of ATL03. This shows that ATL06 only improves in vertical accuracy. When the errors are weighted by the frequency of occurrence of the slopes on the Austrian glaciers as shown in figure 31 the accuracy of ATL06 becomes 1.72 m.

5.2.3 GEDI L2A

The histogram for the GEDI L2A to DEM height differences is shown in figure 32b. The systematic error as represented by the mean (0.85) and median (1.29) is larger but comparable to that of ICESAT-2. However, the MAD is much larger at 7.66 m. Also note the larger scale on the x-axis of the histogram.

An explanation for this could be the much larger area that each GEDI datapoint represents, compared to ICESAT-2. The returning waveform of GEDI represents a footprint with a diameter of approximately 30 m. All elevations within this footprint are being represented by a single point, and there is no information about the precise horizontal location within the footprint that this single elevation represents. Since the mountainous terrain can lead to quite a large height difference within such an area, it may be more suitable to take an average of all DEM pixels within the footprint rather than picking a single DEM height.

In addition to the larger dispersion of the GEDI data, it is also relatively more common for very large height differences to occur, as can be seen by the long tails of the histogram.

The slope analysis of the GEDI data, as shown in figure 34, shows a strong correlation between the slope of the terrain and the accuracy. This, again, leads to the conclusion that a large part of the vertical differences are caused by a horizontal error. The MAD in flat areas is 0.78 m, but already crosses 5m at 21 degrees, and 10 m at 36 degrees. The corresponding horizontal error is approximately 12.55 m, and its fit is shown in red in figure 34. The area-weighted on-glacier MAD of GEDI is 5.80 m.

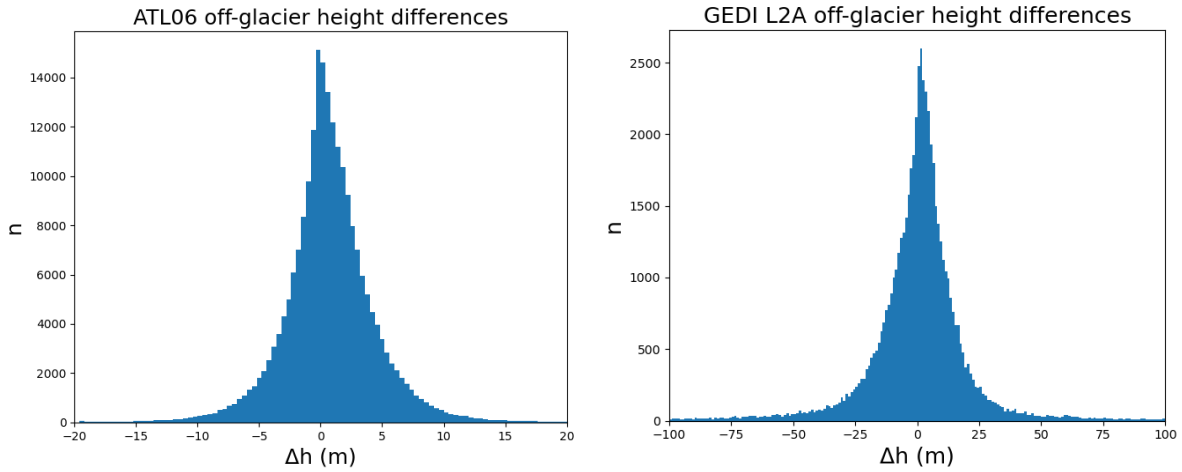

Figure 32: histograms of height differences wrt DEM outside the glacier outlines for (a) ICESAT-2 ATL06 (b) GEDI L2A

	Mean [m]	Median [m]	Std [m]	MAD [m]	Weighted MAD[m]
ICESAT-2 ATL06	0.63	0.52	4.77	1.86	1.72
GEDI L2A	0.85	1.29	11.12	7.66	5.80

Table 4: Accuracy parameters of the ICESAT-2 ATL06 to DEM and GEDI L2A to DEM height differences.

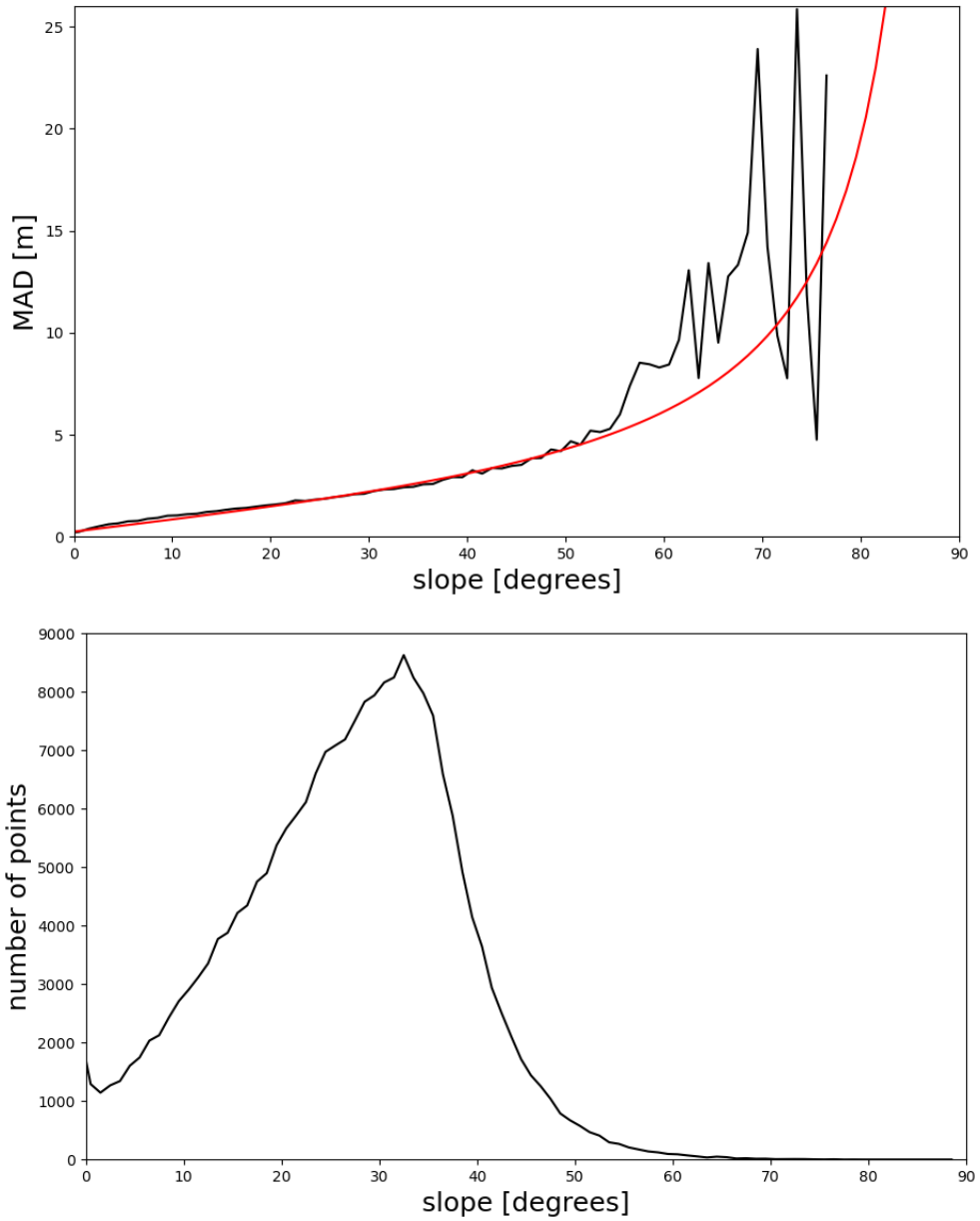

Figure 33: (a) ATL06 Median Absolute Deviation vs slope of the reference DEM (b) Number of points per bin vs slope of the reference DEM

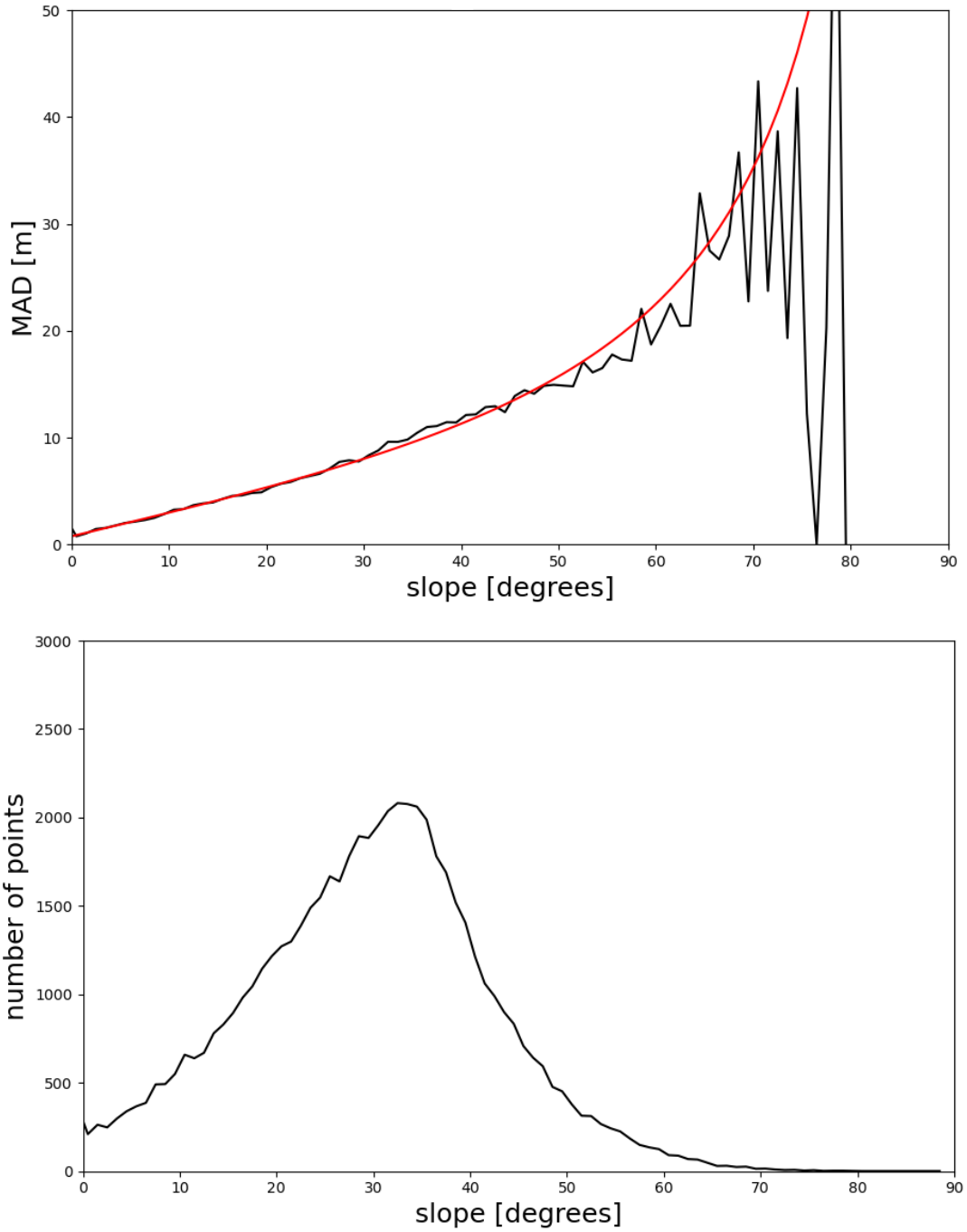

Figure 34: (a) GEDI L2A Median Absolute Deviation vs slope of the reference DEM (b) Number of points per bin vs slope of the reference DEM

6. Results

In this chapter the results of the height change calculations, feature correlation and mass loss using ordinary cokriging will be given.

6.1 Height Differences

The same method to obtain the height differences outside of the glacier outlines for the accuracy assessment was applied to all locations within the glacier outlines. The resulting histograms are shown in figure 35. The medians of the histograms are now shifted to -5.85 m for ICESAT-2 and -4.86 m for GEDI. This shows that on average the Austrian glaciers have lost a considerable amount of ice during this period. The histograms show a relatively long tail towards the more negative height differences, showing that in a minority of locations the glaciers have shrunk significantly more than average. The locations with a height increase are a minority, but still represent a significant portion of the data.

Because GEDI has approximately a third of the amount of satellite passes as ICESAT-2 and a third of the resolution of ATL06 the available data is approximately one ninth, which shows in the histograms.

	Mean [m]	Median [m]	Std [m]	MAD [m]
ATL03	-6.28	-5.87	11.30	3.96
ATL06	-6.49	-5.85	6.89	3.65
GEDI	-4.82	-4.86	15.03	6.01

Table 5: Statistical parameters of all on-glacier differences

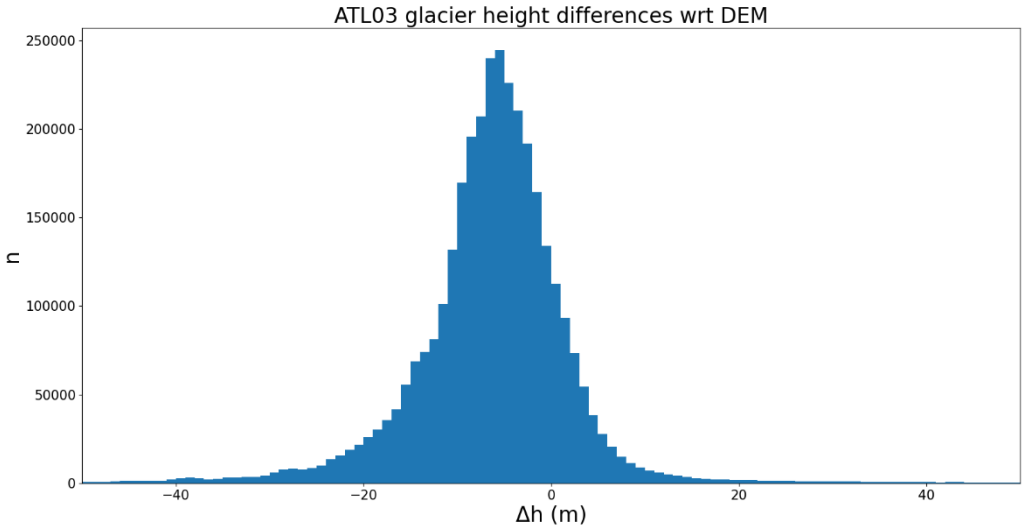

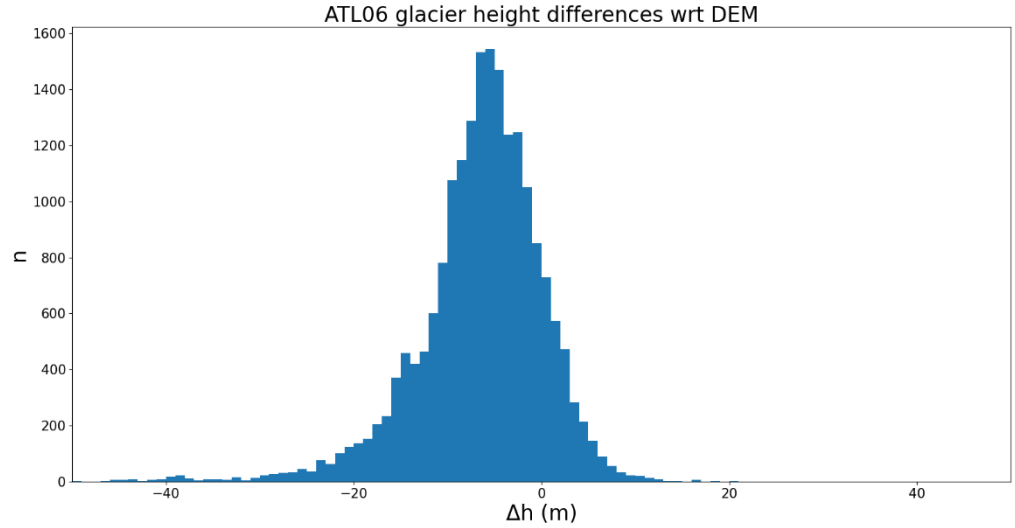

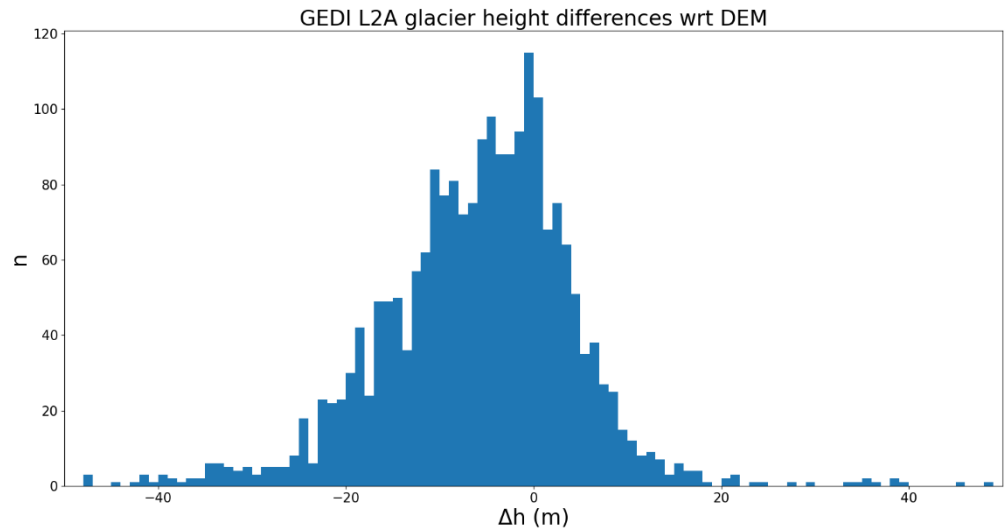

Figure 35: histograms of height differences wrt DEM inside the glacier outlines for (a) ICESAT-2 ATL03 (b) ICESAT-2 ATL06 (c) GEDI L2A

In order to gain a clearer view of how the glacier height differences from ATL06 and GEDI L2A are distributed they are plotted for the Gepatschferner in figure 36 as an example. The GEDI data can be recognized by the almost east-west orientation of the tracks. Clouds were present when the GEDI data was collected, leading to large gaps in the data. What is noticeable is that the largest negative height differences occur on the valley glaciers, whereas changes at higher altitudes are more subtle. The largest negative height difference measured on the Gepatschferner is -50.94 m, or -5.66 m per year. The largest positive height difference observed is 4.95 m, or 0.55 m per year.

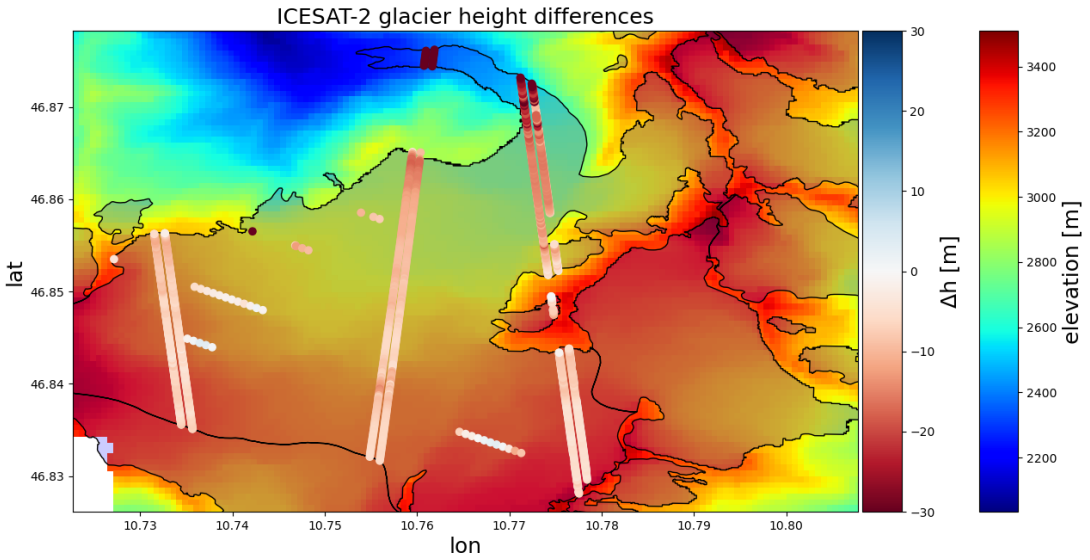

Figure 36: Glacier height differences for ICESAT-2 and GEDI on the Geptaschferner in the Ötztal, Tyrol

A small number of clearly unrealistic values are present in the height difference observations, reaching multiple hundreds of meters, both positive and negative. However, determining what the cut-off value is for realistic observations is not straightforward. Some of the most negative observations can be found on small hanging glaciers as the example shown in figure 37, which has a negative height change of 59.02 m over a 9 year period. All observations of this type are from GEDI and occur on steep gradients, which increases the possibility of large errors as shown in the accuracy analysis. It seems unlikely that such large height differences are purely due to ice loss given the glacier is only 60 meters wide.

Figure 37: A small hanging glacier that has one of the most negative height difference observations with -59.02 m over 9 years. Located at N 47.08° E 10.15°. Footage from 2015, Google Earth.

The occurrence of these types of values is relatively rare, and they represent a small fraction of the glacier area. Their inclusion has a minimal effect on the further analysis, so the cut-off value has been set at 100 m.

The largest realistic ice thickness loss that is not of the type above can be found on the tip of the glacier tongue of the Pasterze glacier, one of the largest glaciers in the country. The height loss here is 53.02 m over 8 years, or 6.63 m per year.

Likewise, most of the outliers with a large positive height change are from GEDI. Positive height changes are more commonly found in relatively flat areas at high altitude. The largest value that cannot be considered an observation error is 17.0169 m over 9 years and can be found at the top of the Hintereisferner in the Ötztal.

Figure 38: Pasterze glacier [71], with an observed negative height change of 53.02 m over 8 years.

6.2 Feature Correlation

Since it is hypothesised that low lying valley glaciers are subject to larger ice loss the relation between the elevation and the measured height difference is examined. Figure 39 shows the DEM elevation of all ATL06 and GEDI datapoints and the corresponding height difference. The mean of every 10 m bin is shown by the black line. When ignoring the regions with low sample sizes, a gradual upward trend can be observed, meaning that more ice loss occurs at lower elevations. The Pearson correlation coefficient between elevation and height change is 0.28.

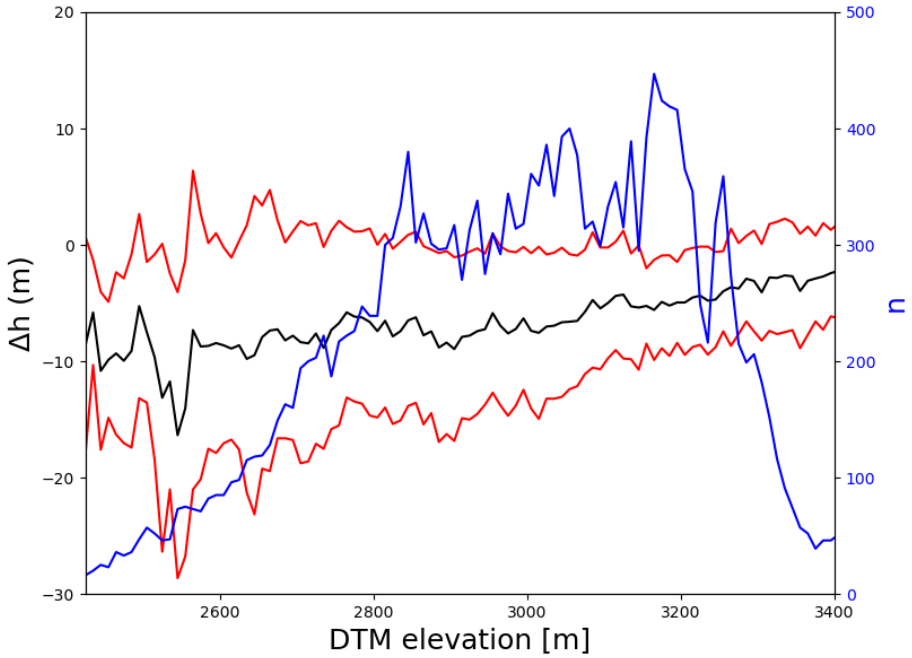

Figure 39: Comparison between the DEM elevations and the measured height differences for ICESAT-2 ATL06 and GEDI L2A. The black line represents the mean of every 10 meter elevation bin, and the red lines show the standard deviation of points within each bin. The blue line shows the number of points within each bin

When examining individual glaciers, a common pattern can be observed when comparing the elevation and the observed height differences, see for example figure 40. At the lowest elevations of the glacier, the height difference tends to be close to zero, but this quickly drops to the largest negative height difference. A cause of this could be that the glacier has already disappeared at the lowest elevations, while the lowest areas where it is still present are subject to the most loss of ice. After the minimum, the height difference tends to gradually return to more positive values, while the highest elevations have values close to zero or even positive height changes. This corresponds to the accumulation zone, where the presence of recent snowfall might have a larger influence than the ice loss of the glacier.

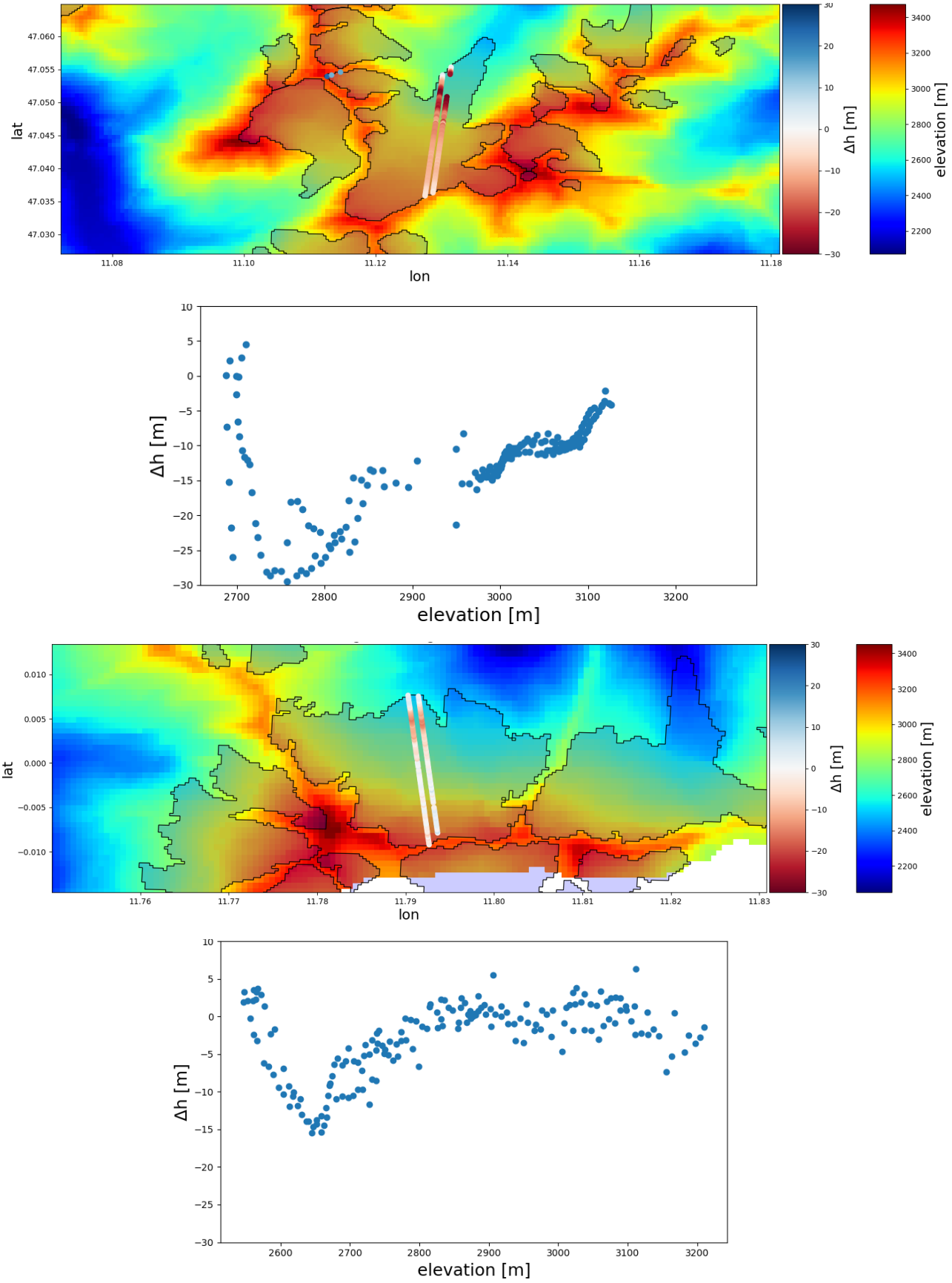

Figure 40: examples of altimetry data over glaciers in Austria with their corresponding plots comparing elevation and the observed height differences

The closest distance to the edge of the glacier outline is computed for every point. From looking at the locations of height differences in plots as figure 40, it seems that points lying close to the edge of the glacier are generally more stable, maybe because the glacier has disappeared at these locations over time.

The mean height difference starts at -2.63 m and decreases to -8.90 m at 160 m from the glacier edge, after which it increases again. While on average the height difference is small for small distances to the edge of the glacier, there is a wide spread of datapoints here, and many locations close to the glacier edge have large negative or even positive values. This shows that at many of these locations the glacier has not yet disappeared.

Distances of several hundreds of meters only occur in a small number of large glaciers at higher elevations, so the effects here are expected to be mostly related to elevation.

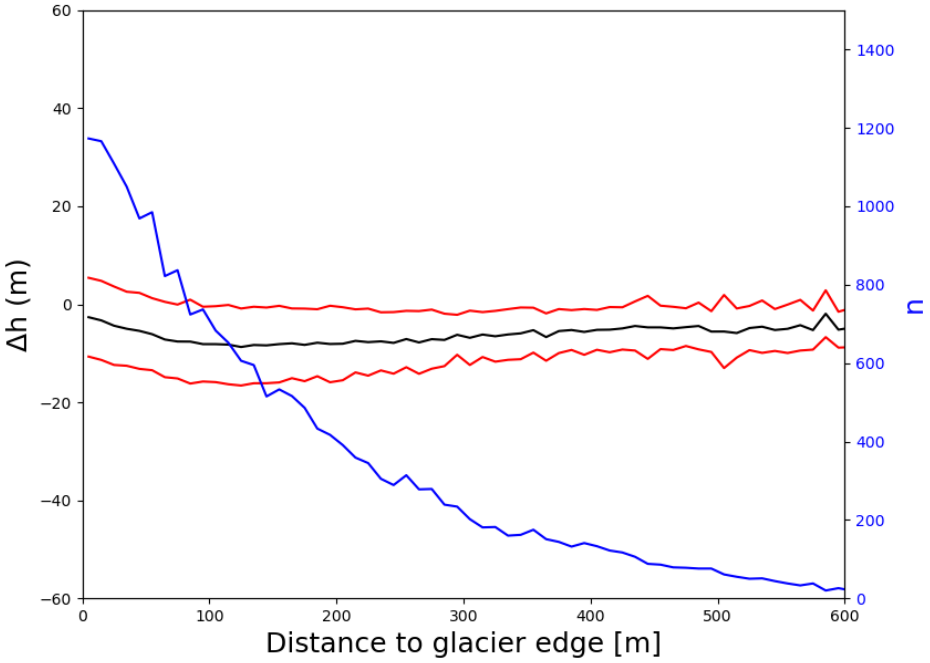

Figure 41: Comparison of the closest distance of every point to the edge of the glacier and the corresponding measured height change. The black line represents the mean of every 5 meter bin, and the red lines show the standard deviation of points within each bin. The blue line shows the number of points within each bin

The slope of every DEM pixel was computed as described in chapter 4.2, and every altimetry datapoint was given its corresponding slope value. Figure 42 shows the resulting relation, again with a trend line showing the mean of every 1 degree bin. The mean height change starts at approximately -8 m for flat areas and increases to -2 m at 40 degrees. This shows a slight correlation between the slope and the height differences, but this may be connected to the differences in slope between low and high elevation zones, which can be more accurately captured by the elevation comparison. Slopes steeper than 40 degrees are uncommon on the glaciers.

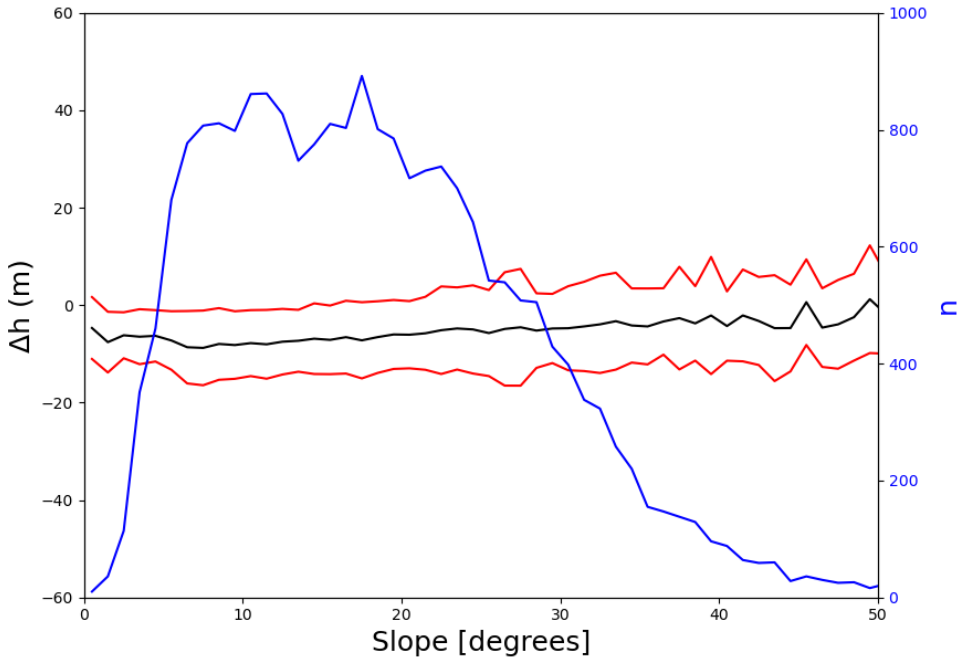

Figure 42: Comparison between the slope of every datapoint based on the DEM and the corresponding height change. The black line represents the mean of every 1 degree bin, and the red lines show the standard deviation of points within each bin. The blue line shows the number of points within each bin

Figure 43 shows the relation between the aspect and the measured height differences. The mean height difference is approximately -10 m for aspects near 0 or 360 degrees, while aspects near 180 degrees have a mean height difference of approximately -3 m. Strangely, glacier slopes pointing south towards the sun seem on average to suffer less ice loss than glaciers pointing north. A possible explanation for this is that most of the larger glaciers in Austria face north, and that the largest negative height differences are found on the larger glaciers. The blue line in figure 43 confirms that significantly more observations are found on north facing slopes.

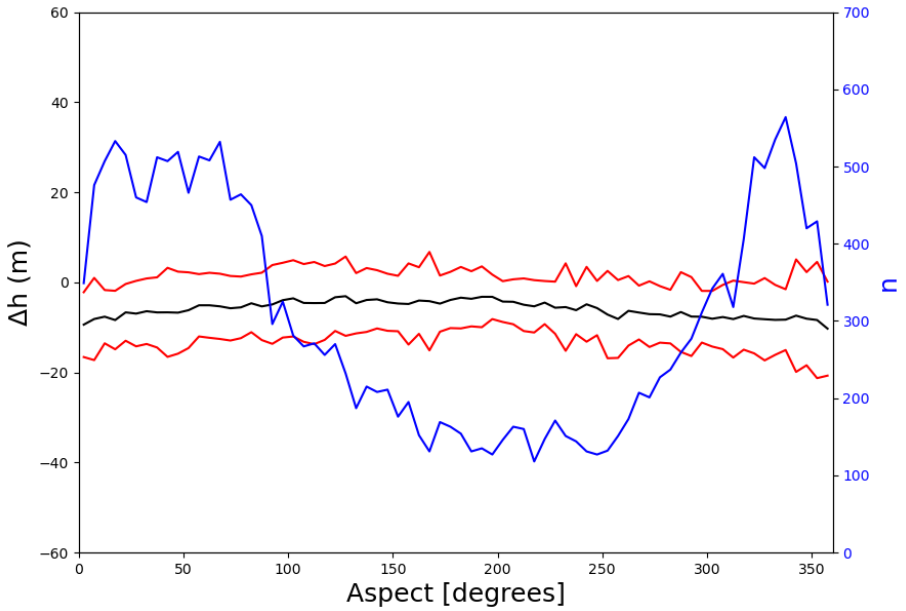

Figure 43: Comparison between the aspect of every datapoint based on the DEM and the corresponding height change. The black line represents the mean of every 5 degree bin, while the red lines show the standard deviation of points within each bin. The blue line shows the number of points within each bin.

6.3 Ice Volume Loss

To determine the ice volume loss the cokriging procedure was performed for every glacier in Austria containing ICESAT-2 or GEDI data. A grid of cokriging locations was created for every glacier, with a grid resolution of 25 m as a compromise between resolution and runtime.

Figure 44 shows the cokriging results for the Gepatschferner in the Ötztal region in Tirol. For most locations, the cokriging results are similar to that of the observations at similar elevation. An exception here is caused by a disagreement between two tracks in the accumulation zone at similar altitudes, so the correlation between elevation and height change does not hold in this situation. As a result, the cokriging results may differ from nearby observations.

Figure 45 shows the cokriging results for the Pasterze glacier in Carinthia. In this particular case, the data falls almost exclusively on the high elevation area corresponding to the glacier accumulation zone. As a result, the average of the height difference observations is close to zero. However, it is much more realistic that the low elevation valley glacier has a similar mass loss as other such glaciers in Austria, which is shown in the cokriging results.

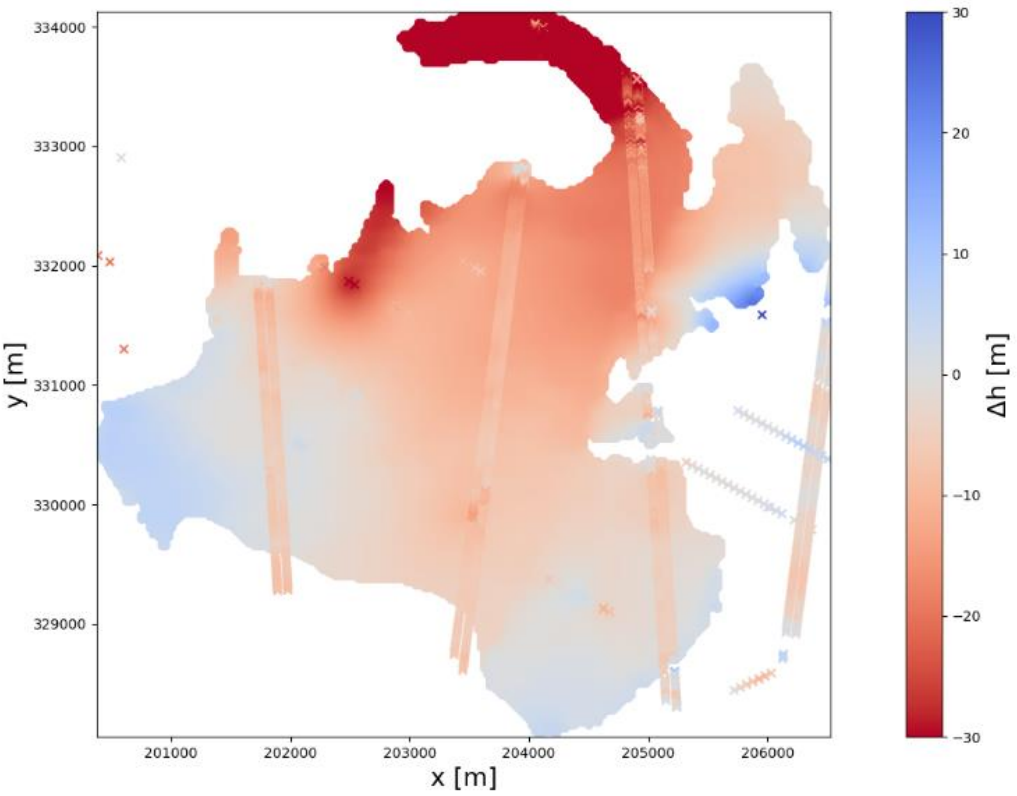

Figure 44: Cokriging results of the glacier height differences of the Gepatschferner

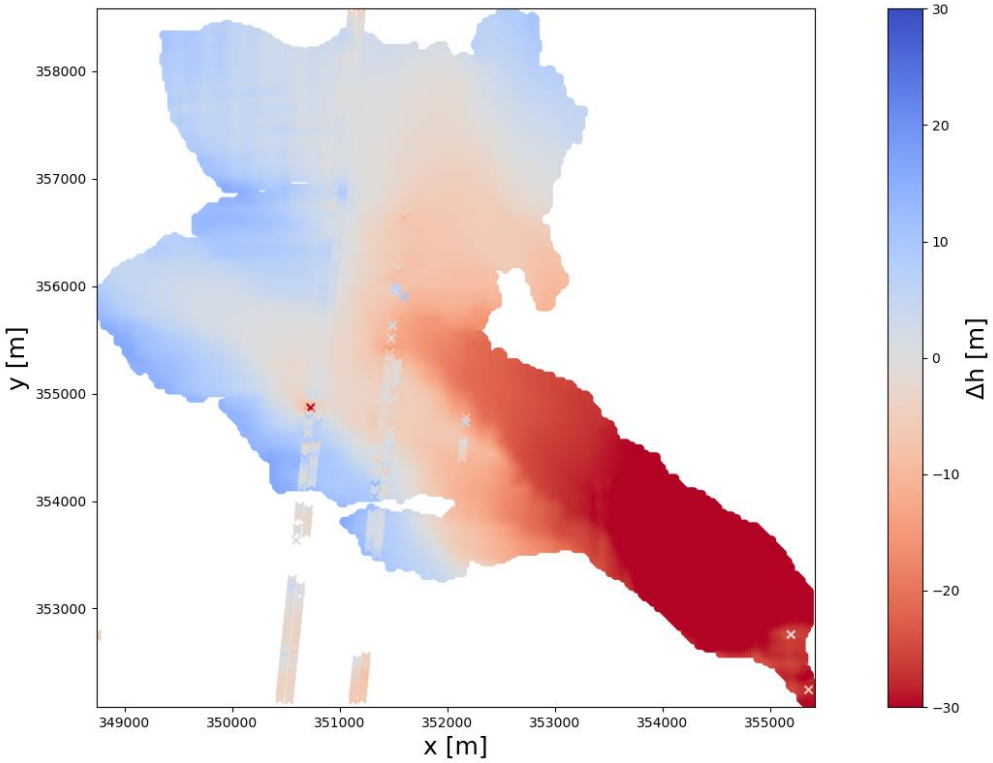

Figure 45: Cokriging results of the glacier height differences of the Gepatschferner

In order to obtain a figure of the total mass loss in a region, other studies commonly assume the spread of glacier elevations in the area is well represented by the spaceborne observations. If this is the case, multiplying the height differences by the total glacier area and dividing by the number of observations therefore gives the total ice volume loss. Assuming an ice density of 850 kg/m^3 this results in a mass loss for Austria of 1.59 Gt. The cokriging method only increases this number by 3.4 Mt. It can therefore be concluded that the method gives more insight into glacier behaviour at smaller scale without skewing the large scale result.

As discussed in chapter 4.1, the DEM used in this analysis was created in the timespan of 2006 to 2016. As a result it is not possible to compare the total figure for Austria with other results from literature. However, the part of the DEM in the area of the Ötztal glaciers was collected completely in the year 2010. The glaciers in the Ötztal account for 0.76 Gt of mass loss, slightly less than half of the total mass loss in the dataset. Sommer et al. (2020) determined a yearly volume change in the Ötztal of 0.10 km^3 for the period 2000-2012 [22]. The results from the ICESAT-2 and GEDI analysis over the years 2010 to 2019 show 0.091 km^3 annual ice volume loss. This corresponds to 77.07 Mt annual ice mass loss. Figure 46 shows an overview of mass loss in megatons for the Ötztal region. Figure 47 shows the mass loss per glacier divided by the surface area, which corresponds to the average height loss of the glacier determined by cokriging.

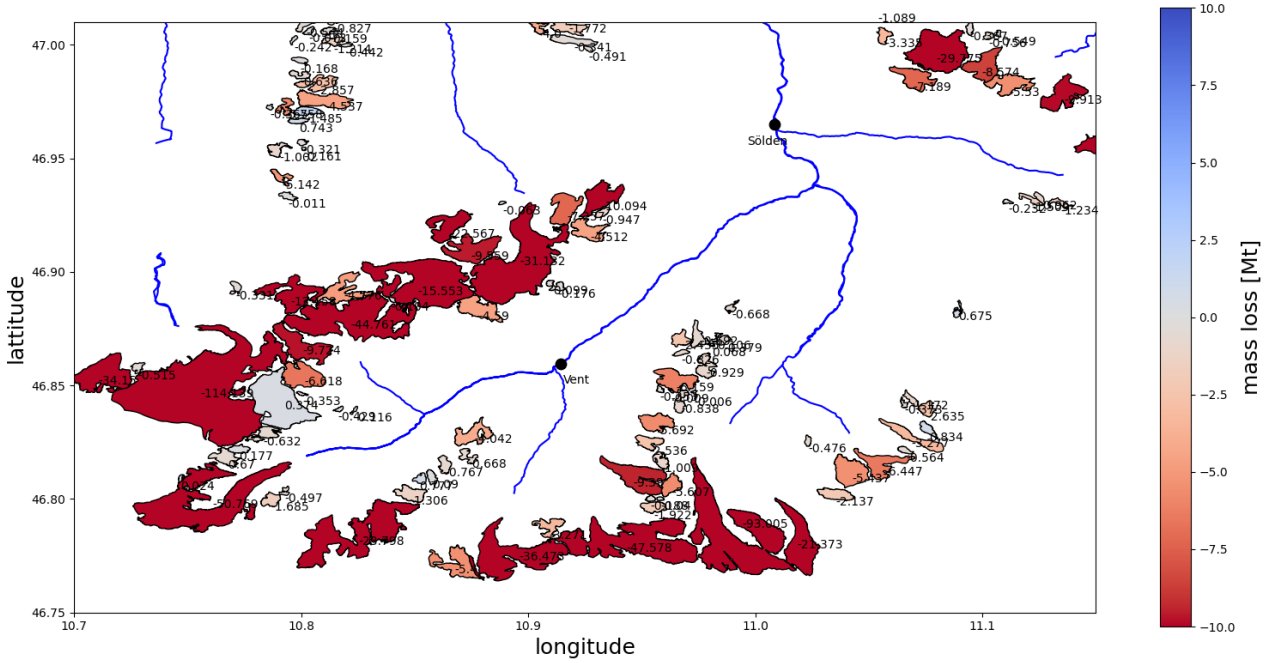

Figure 46: Map of mass differences in the Ötztal region for the period 2010-2019

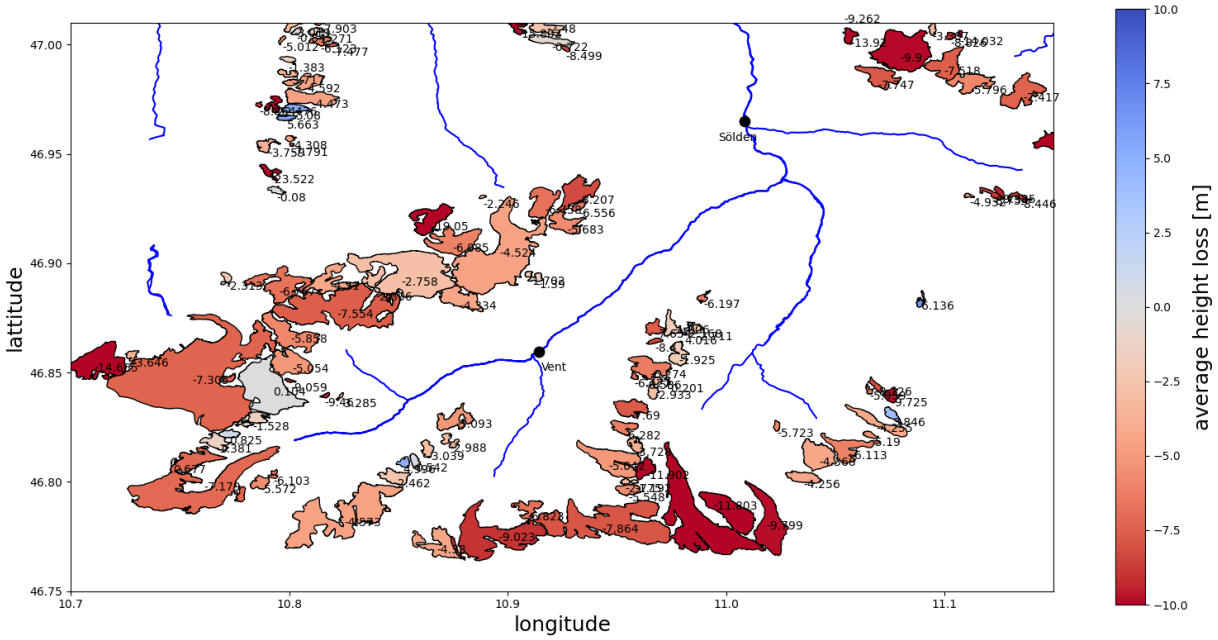

Figure 47: Map of cokriging results in the Ötztal as average height loss

One of the glaciers that jumps out in figure 46 and figure 47 is the Vernagtferner, which can be recognized by a mass difference that is almost zero, whereas the surrounding glaciers have larger mass losses. Charalampidis et al. (2018) describes the geometry changes of the Hintereisferner, Kesselwandferner and Vernagtferner for the period 1981-2010 [72]. They found that the Kesselwandferner responds relatively quickly to short term changes in local climate, and may have periods of advancing after periods of glacier retreat. This may explain why the glacier shows a slightly positive mass balance whereas most of its surrounding glaciers have a large negative mass balance.

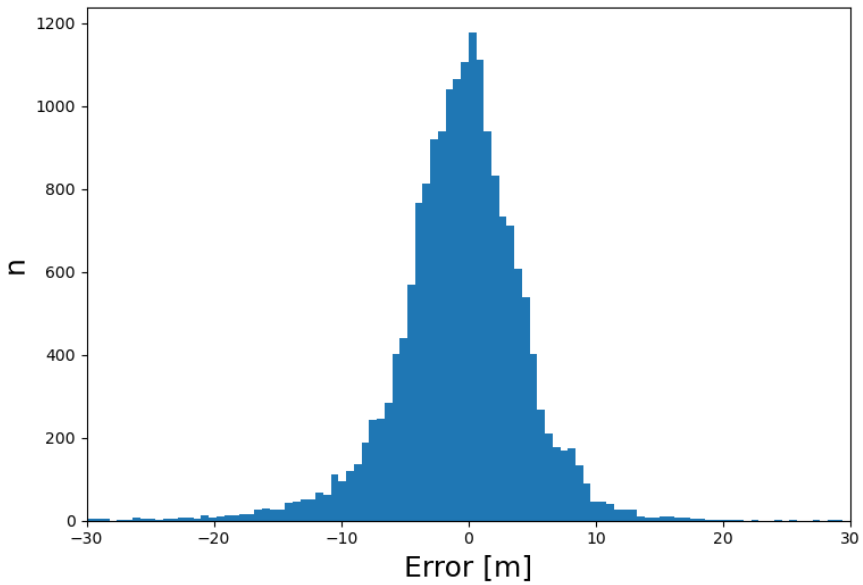

Figure 48: Histogram of errors from cross-validation leaving out one track each time (N = 18685).

Cross-validation of the cokriging results shows a slightly negative systematic error with a mean of -0.66 m and a standard deviation of 5.18 m. The histogram of cross-validation errors is shown in figure 48.

The negative systematic error suggests that the total mass loss estimated by the cokriging procedure will be too large. The mean of -0.66 m can be converted to a mass of -347.99 tonnes per pixel. Summing all 487,959 cokriging pixels for Austria, this results in a bias of -169.81 Mt. The bias for the Ötztal region becomes -7.08 Mt per year.

Every pixel for which cokriging is performed represents an area of 25m x 25m, so 625 m^2. Using the uncertainty found by cross-validation and an ice density of 850 kg/m^3 this gives a mass uncertainty of 2751 tonnes per pixel, which corresponds to 1.922 Mt for the whole of Austria, or 0.13 Mt per year for the Ötztal. It should be noted that this uncertainty describes how well the cokriging results match the observations, and does not include the accuracy of the observations themselves.

7. Discussion

Firstly, the suitability of ICESAT-2 and GEDI for observing glacier mass changes in general will be discussed and compared to other frequently used sensors. Secondly, the ice loss results for Austria and related technical issues will be discussed.

7.1 Comparison with other satellite sensors

ICESAT-2 and GEDI are relatively new sensors, so one can ask what their added value is to the set of satellites already used for the analysis of mountain glacier ice loss. The performance of ICESAT-2 and GEDI will be compared to the alternative sensors described in chapter 2.3.

7.1.1 ICESAT-2

One of the strong points of ICESAT-2 is its high resolution due to the novel photon counting technique it uses. The 0.7 m horizontal distance between observations is significantly better than that of other spaceborne sensors. The high resolution of the ICESAT-2 data makes it more suitable to investigate smaller glaciers and individual features of glaciers. However, this data comes in the form of a spread of photons present at every location in the ATL03 data, which means the glacier surface elevation at any location is ambiguous and the size of the datasets becomes relatively large. The higher level ATL06 data creates a single unambiguous glacier elevation with a better accuracy, but reduces the resolution to 20 m, similar to that of other sensors.

According to the ICESAT-2 algorithm theoretical basis documents (ATBD) the expected vertical geolocation error will generally be below 0.1 m vertically and 5 m horizontally([51], see also chapter 3.1.4). The accuracy analysis shows that for flat areas, the MAD is 0.41 m for ATL03 and 0.21 m for ATL06. This is slightly larger than the expected vertical error, which can be caused by errors in the DEM, the lower resolution of the DEM, or the fact that the accuracy estimation of the ATBD does not account for photons being erroneously labelled as surface reflections. The horizontal accuracy was estimated as 3.41 m for ATL06.

The accuracy weighted for slopes of ATL06 was determined to be 1.72 m. In terms of accuracy ICESAT-2 substantially outperforms most of the other commonly used satellite sensors, including ASTER, CryoSat-2 and SRTM. TDX has errors of similar sizes, though the accuracy is generally larger than 2 m for glacier areas. The radar penetration bias introduces further uncertainty for TDX, making ICESAT-2 the best choice when accuracy is the first priority.

ASTER's accuracy is significantly worse than that of ICESAT-2. However, since the repeat sampling period for any point is only 16 days the error size can be mitigated when the elevation change trend is estimated, since a large amount of observations are available [27]. ASTER's better spatial and temporal coverage make it perhaps more suitable for estimating the long term volume change trend, whereas ICESAT-2's better resolution and accuracy are better for small scale and short term changes.

The main downside of ICESAT-2 and spaceborne lidar sensors in general is the spatial coverage. The shifting repeat orbits result in two sets of parallel profiles at 810 m apart for Austria, as shown in figure 18. This means that any glacier has a good chance of being included in the ICESAT-2 data, but nevertheless all data remains limited to narrow profiles of the surface, and only a very limited percentage of the glacial area will be covered. In order to draw conclusions about the ice loss of a glacier or larger region the observations have to be extrapolated, and assumptions have to be made.

Remote sensing satellites using radar (TanDEM-X, CryoSat-2, SRTM), imaging (ASTER) or gravimetry (GRACE-FO) create a more complete image of the areas they sample. In addition, lidar data will not be able to collect data for areas covered by clouds, further reducing the amount of available observations.

ICESAT-2's good resolution and accuracy also make it suitable for validation or calibration of other types of data. The first ICESAT mission was widely used for quality assessment of DEM's, and ICESAT-2 has also been found to be of sufficient quality [73]. For glaciers this can be particularly useful in the case of radar based DEM's (such as those of SRTM, TanDEM-X or CRYOSAT-2), since they are known to be susceptible to bias caused by penetration of the radar signal into ice and snow [28]. ICESAT-2 can be used to estimate this effect, since lidar observations are not subject to such a bias.

7.1.2 GEDI

The mission objective of GEDI is to characterize the effects of changing climate and land-use on ecosystem structure and dynamics [57]. It has already been used to study canopy height and land use in numerous studies, but it has not yet been applied to glacier analysis.

As shown in chapter 5, the accuracy of the GEDI data used in this study is much worse than that of ICESAT-2. The MAD of GEDI points outside the glacier outlines in the Austrian mountains is 7.66 m, and errors as large as 20 m with regards to the DEM are not uncommon. These errors do not agree with the dynamically estimated vertical errors in the L1B product, which normally do not exceed 1 m. It is therefore expected that the largest contribution is the geolocation error, which can reach up to 10 m in the L1B product. The dependency of the slope shown in figure 34 shows that the errors are indeed heavily dependent on the slope, and that for completely flat areas the vertical MAD is 0.78 m, which is more similar to the errors estimated by L1B. The horizontal error determined from this analysis is 12.55 m, worse than those in the L1B product. When weighted for the slopes found within glacier outlines the error becomes 5.80 m.

Part of the suspected large geolocation error may be due to GEDI's footprint of 30 m. There is no information about the horizontal location of the specific returns of the waveforms within the footprint whereas ICESAT-2 can determine the exact location of photons within its footprint. This means that taking the lowest return will result in a height representing any of the pixels of the DEM within the footprint. Most waveforms on the examined glaciers have a single mode return that is spread out vertically over some meters. Taking this return will therefore probably best represent the average elevation within the footprint. However, for the DEM the centre pixel is taken because this is where most of the return energy will be expected.

As a result of the suboptimal accuracy, it can be questioned whether adding GEDI to the analysis is worthwhile. When the ICESAT-2 mission is completed, it will have created two sets of parallel profiles 810 m apart. Nevertheless, smaller glaciers can be missed by ICESAT-2, especially considering that cloud coverage can be an issue. Including GEDI improves the chances of smaller glaciers to be sampled, also because its ground tracks run almost perpendicular to those of ICESAT-2.

7.2 Ice loss results for Austria

A number of issues related to the determined glacier height differences and the cokriging results remain.

As described in chapter 4.1 the DEM was created during a ten year period (2006-2016), and the age is not the same for every location. Different locations have a different time span over which the mass loss per year is determined. Therefore, it was decided to focus the comparison of mass loss result on the Ötztal region, since its DEM was collected exclusively in the year 2010, and because other estimates about previous annual mass loss have been made there [22] [63]. The varying DEM age also undoubtedly has an influence on the feature correlation analysis, although when examining the data it seems like most locations do not differ by more than a couple of years.

The altimetry data was not filtered by month for two reasons. Firstly, this would almost halve the amount of data while some areas are already under-sampled, and secondly the time of year the DEM was collected is unknown, even for the Ötztal, so it cannot be known for sure how the data should be filtered. This is probably why some of the crossover locations seem to disagree significantly, especially in the acquisition zones. It could be expected that the DEM was collected when the snow cover was minimal, so this may introduce a positive bias, underestimating the mass loss.

The glacier outlines created by Paul et al. (2020) were estimated specifically for the year 2015. The glaciers in the Alpes have lost a considerable amount of mass since then, so the glacier outlines can be expected to have shrunk, especially considering the large difference with the RGI outlines representing 2003. As already discussed in chapter 6.2, ICESAT-2 and GEDI data seems to confirm this in some cases, as the height change suddenly becomes more positive close to the edge of the outlines. The off-glacier elevation change does not have a significant bias, so it is expected to be close to zero in these locations. However, when extrapolating the observations to areas without data using cokriging, this effect is not taken into account, which introduces a negative bias to the estimation (the glaciers outlines are too large, and therefore the estimated mass loss is too large).

Of all glaciers in Austria 371 out of 661 (56%) have no ICESAT-2 or GEDI data for the timespan used here. Most of these glaciers have a very small surface area, so that in terms of area only 12% of glaciers contain no data. It was decided not to estimate their volume and mass difference with cokriging. The ice thickness change on the smallest glaciers tends to be smaller than that of larger glaciers, so the impact on the total mass change is expected to be small. Nevertheless, since the average glacier mass difference is negative, not including a number of glaciers may introduce a positive bias.

Nilsson et al. (2015) examines four different methods for extrapolating ICESAT data of icecap and glacier regions [74]. The methods are split into two groups: those using the spatial distribution of the observations with regard to the extrapolation point and those using the relation between height change and elevation. The first category ignores the correlation between height change and elevation, and therefore requires that the area is well sampled so that variations due to elevation differences are captured. This is not normally true for spaceborne lidar data, and certainly not for the ICESAT-2 and GEDI data used in this thesis. Ordinary kriging is an example of such a method. The second category assumes that the relation between elevation and height difference adequately describes the observations, and that the region behaves homogeneously in this regard. Such a method is used by Nuth et al. (2010) [75] and Moholdt et al. (2010) [31]. As can be seen by the results in this thesis, points lying at equal elevation may still vary significantly in their height change.

Cokriging can be seen as a compromise between these two types of extrapolation, since it takes into account both the nearby observations and the local elevation.

As already discussed in chapter 6.3, the cokriging results agree with the regular extrapolation method about the total volume and mass loss for Austria. It can be concluded that the cokriging method increases the accuracy of results for individual under-sampled glaciers without significantly altering the accuracy of the regional mass loss.

Cross-validation of the cokriging procedure shows a negative systematic bias which is not negligible. A possible explanation is that cokriging estimates an ice loss at locations where the glacier outlines are outdated and the glacier has already disappeared, so no ice loss would be present. The uncertainty of the total ice mass loss from cross-validation is small, but it should be considered that the accuracy of the observations themselves is not included, as well as the uncertainty of the glacier areas.

Cokriging allows for a visualisation of the ice loss at every location, based on nearby data or the whole dataset, giving insight into the heterogeneity of the ice loss in the study area and on the characteristics of individual glaciers. Comparing the mass loss results for just the Ötztal region shows a good agreement with other estimations [63] [22].

8. Conclusion & Recommendations

8.1 Research Questions

The main research question of this thesis was: *How can a combination of ICESAT-2 and GEDI data be used to detect changes of Alpine glaciers?* The main conclusion is that the high resolution and accuracy of ICESAT-2 can provide valuable detailed information about glacier height differences in the Austrian Alpes, and that the inclusion of GEDI data can help provide observations in sparsely sampled areas, but considering its relatively poor resolution and accuracy better alternatives may be available. A more detailed conclusion will be given for every subquestion.

1. Why is Alpine glacier change relevant?

Mountain glaciers contribute significantly to global sea level rise and are sensitive indicators of climate change. In addition, their mass loss has consequences for the local hydrology, ecology and economy. High quality height observations of the relatively small Austrian glaciers are required so that the time series of their mass balance can be determined for the past and present and predicted for the future.

2. What is a suitable workflow to process ICESAT-2 and GEDI data to ice thickness changes?

How are ICESAT-2 geolocated photon and GEDI geolocated waveform products created and how do they compare?

An overview of the ICESAT-2 and GEDI data collection and postprocessing was given in chapter 3. The photons collected by ICESAT-2 are filtered with a surface detection algorithm, classified by the probability of being a surface return, and precisely geolocated. The result is presented in the ATL03 product, which provides data at a 0.7 m resolution, but also includes a vertical spread of photons per location instead of a single surface elevation. The ATL06 product provides a single elevation value per location with a higher quality, but also reduces the resolution to 20 m. GEDI uses a more conventional full waveform lidar, where every waveform represents a 30 m diameter footprint. The L1B product provides the complete waveform with 0.15 m vertical resolution, with one waveform every 60 m along track. The L2A product detects the different returns in every waveform and provides their geolocation. For most glacier surface locations there is only a single return in the L2A product.

How does a combination of ICESAT-2 and GEDI improve the spatial and temporal coverage for the selected Alpine glaciers?

After 8 repeats over the entire mission lifetime, ICESAT-2 will have created 2 sets of parallel lidar ground tracks (one set ascending and one set descending) at a horizontal distance of approximately 810 m over Austria. Since GEDI is attached to the ISS its ground tracks do not form such a regular pattern. Over Austria, the GEDI ground tracks are almost perpendicular to the ICESAT-2 ground tracks, which improves the chance of GEDI sampling glacier locations missed by ICESAT-2 and also increases the amount of crossover locations greatly. The ICESAT-2 and GEDI missions are active until early 2021 so they are simultaneously active for most of their mission duration, which is another reason for a combined analysis,

How can Lidar altimetry be used in combination with a Digital Elevation Model to estimate ice thickness changes?

All ATL03, ATL06 and GEDI L2A tracks were filtered to the glacier outlines in Austria. Their elevations were converted from ellipsoidal to geoid height. The Austrian DEM was converted to the global WGS84 reference system. For GEDI the lowest return present in the L2A data was taken as the glacier surface return. The corresponding DEM elevation of every ICESAT-2 and GEDI point was determined by bilinear interpolation, and subtracted from their own elevation. The resulting median glacier height difference was -5.85 m for ICESAT-2 and -4.86 for GEDI.

What is the quality of estimated ice thickness changes?

The quality of the ICESAT-2 and GEDI data was determined by comparing them to the DEM for all locations outside of the glacier outlines. The errors were compared with the local slope, which showed that the accuracy drops significantly with an increasing gradient, which shows that the horizontal errors are larger than the vertical errors for both satellites. The systematic errors are below one meter. The off-glacier accuracy was weighted for the distribution of on-glacier slopes, which resulted in a random error below 2 meters for ICESAT-2 and below 6 meters for GEDI. The relatively low accuracy of GEDI is determined to be caused mainly by the large horizontal error.

3. How can characteristic features (such as elevation, slope, proximity to the edge of the glacier) of locations on the glacier be created and how do they correlate with their estimated ice thickness change?

The elevation, distance to glacier edge, slope and aspect were calculated for every observation and their relation with the glacier height change was examined, both for the whole region and for individual glaciers. All four features were found to have some information that could be used to extrapolate the observations to other glacier locations. The elevation analysis confirms that low lying valley glaciers have more negative height differences whereas the accumulation zones have almost no elevation loss or an elevation increase. The analysis of the distance to the glacier outlines shows that the outlines are outdated in some locations, but also shows that points near the edge show a smaller height decrease in general. The trends of the slope and aspect are more subtle. In case of the aspect, it even seems contradictory to what may be expected, namely that glaciers facing south will melt more than those facing north. A possible explanation for this is that most of the larger glaciers in Austria face north, and that the largest negative height differences are found on the larger glaciers.

4. Can estimated ice thickness changes be used to infer the mass balance of the whole glacier?

In most cases the ice thickness changes on a single glacier are limited to several profiles which are not sufficiently representative of the glacier as a whole. However, when taking all glaciers in Austria the observations can be assumed to be representative of the height change on average, and the relation between elevation and height change. If the observations are truly representative, the mean height difference can simply be applied to the total glacier area to acquire the total volume loss. However, this does not provide any detail about local ice loss outside the observations themselves. Ordinary cokriging was used to estimate the glacier height change for every glacier location with a 25 m resolution, also giving volume change figures for every individual glacier. The cokriging results agree well with the more conventional method of extrapolation, as well as other available figures in the Ötztal region. Cross-validation of the cokriging method shows a significant negative bias.

5. How do the results compare to those obtained by other methods?

Compared to other frequently used satellites ICESAT-2 has a better accuracy and resolution. A downside is that it has limited spatial coverage and is susceptible to clouds. Although the addition of GEDI data can be useful by sampling more areas its relatively low accuracy and resolution mean that other sensors could potentially be a better alternative. The cokriging results are in agreement with previous estimations for the Ötztal region, though some biases are expected to be present.

8.2 Recommendations

Improvements to the current method

The most obvious improvement to the ice loss estimations provided in this thesis is to include all data from the ICESAT-2 and GEDI missions when they have been made available. Only a small part of the dense pattern of ground tracks shown in chapter 3.3 are present in the current data. The quality of the total mass loss estimation will be improved by this, and the details of cokriging results will become more realistic when they are based less on the secondary variable.

The ATL06 product improves the accuracy compared to ATL03, but also reduces the resolution to 20 m. Determining the surface elevation from shorter segments of photons should be possible to retain the high resolution, which is one of the main advantages of ICESAT-2. Even averaging the photons every 0.7 m could decrease the random error of ATL03, and provide a much greater number of datapoints, which can be especially helpful near glacier edges where the height differences seem to behave more erratically.

The current analysis does not account for temporal differences between the observations. Including seasonal effects could make mass loss estimations more precise. Differences between weak and strong beams of both ICESAT-2 and GEDI have been observed, but their performance has not been analysed separately.

Further Research

The ability to create many different features characterising all glacier locations leads to the possibility of extrapolating observations using a machine learning regression model. In addition to the features presented in this thesis, many other features could potentially add more information to such an algorithm, including surface roughness, sun hours and glacier colour.

The comparison between distance to the glacier outline and observed height difference (figure 41) shows a clear trend that cannot be attributed solely to the outdated outlines. While there are many locations that show an exception to this rule, it may be beneficial to include this information when extrapolating the data.

ICESAT-2, especially in combination with GEDI, will produce a large amount of crossover points that allow for a time series analysis, though the amount of crossover locations within a single glacier will be minimal. These crossover locations provide opportunities to examine a time series within the dataset.

The volume loss of any point on the glacier is not necessarily a reflection of how much ice melted at that particular point, but for larger glaciers is more likely a result of changes in the large scale glacier flow.

References

[1] M. Zemp, H. Frey, I. Gärtner-Roer, S. Nussbaumer, M. Hoelzle, F. Paul and C. Vincent, "Historically unprecedented global glacier decline in the early 21st century," *Journal of glaciology,* vol. 61, 2015.

[2] J. L. Bamber, R. M. Westaway, B. Marzeion and B. Wouters, "The land ice contribution to sea level during the satellite era," *Environmental Research Letters,* vol. 13, 2018.

[3] B. Wouters, A. S. Gardner and G. Moholdt, "Global Glacier Mass Loss During the GRACE Satellite Mission (2002-2016)," *Frontiers in Earth Science,* vol. 7:96, 2019.

[4] M. Zemp, M. Huss, E. Thibert, N. Eckert, R. McNabb, J. Bannwart, M. Barandun, H. Machguth, S. Nussbaumer, I. Gärtner-Roer, L. Thomson, F. Paul, F. Maussion, S. Kutuzov and J. Cogley, "Global glacier mass changes and their contributions to sea-level rise from 1961 to 2016," *Nature,* vol. 568, 2019.

[5] D. Vaughan, J. Comiso, I. Allison, J. Carrasco, G. Kaser, R. Kwok, P. Mote, T. Murray, F. Paul, J. Ren, E. Rignot, O. Solomina, K. Steffen and T. Zhang, "Observations: Cryosphere," *Climate Change 2013: The Physical Science Basis. Contribution of Working Group I to the Fifth Assessment Report of the Intergovernmental Panel on Climate Change,* 2013.

[6] R. Hock, G. Rasul, C. Adler, B. Cáceres, S. Gruber, Y. Hirabayashi, M. Jackson, A. Kääb, S. Kang, S. Kutuzov, A. Milner, U. Molau, S. Morin, B. Orlove and H. Steltzer, "High Mountain Areas," *IPCC Special Report on the Ocean and Cryosphere in a Changing Climate,* 2019.

[7] A. Gardner, G. Moholdt, J. Cogley, B. Wouters, A. Arendt, J. Wahr, E. Berthier, R. Hock, W. Pfeffer, G. Kaser, S. Ligtenberg, T. Bolch, M. Sharp, J. Hagen, M. Van den Broeke and F. Paul, "A Reconciled Estimate of Glacier Contributions to Sea Level Rise: 2003 to 2009," *Science,* vol. 340, 2013.

[8] World Glacier Monitoring Service, "Kesselwandferner," [Online]. Available: https://wgms.ch/products_ref_glaciers/kesselwandferner-alps/. [Accessed 22 11 2020].

[9] F. Brun, P. Wagnon, E. Berthier, V. Jomelli, S. B. Maharjan, F. Shrestha and P. D. A. Kraaijenbrink, "Heterogeneous influence of glacier morphology on the mass balance variability in high mountain asia.," *Journal of Geophysical Research: Earth Surface,* vol. 124, no. 6, 2019.

[10] C. Charalampos, F. Andrea, K. Michael, L. Astrid, M. Christoph, T. Konstantinos and W. Markus, "Mass-budget anomalies and geometry signals of three austrian glaciers.," *Frontiers in Earth Science,* vol. 6, 2018.

[11] T. Jóhannesson, C. Raymond and E. Waddington, "Time–scale for adjustment of glaciers to changes in mass balance.," *Journal of Glaciology,* vol. 35, no. 121, p. 355–369, 1989.

[12] R. Pravettoni, "Glacier Mass Balance," [Online]. Available: https://www.grida.no/resources/12826. [Accessed 24 11 2020].

[13] E. Serrano, J. González-Trueba, J. Sanjosé and L. Del Rio, “Ice patch origin, evolution and dynamics in a temperate high mountain environment: the jou negro, picos de europa (nw spain),” *Geografiska Annaler. Series a, Physical Geography,* vol. 93, no. 2, pp. 57-70, 2011.

[14] R. R. Colucci, “Geomorphic influence on small glacier response to post-little ice age climate warming: julian alps, europe,” *Earth Surface Processes and Landforms,* vol. 41, no. 9, p. 1227–1240, 2016.

[15] J. Faillettaz, M. Funk and M. Vagliasindi, “Time forecast of a break-off event from a hanging glacier,” *Cryosphere,* vol. 10, no. 3, p. 1191–1200, 2016.

[16] J. Alean, “Hallstatter Glacier: From the Glacier Photograph Collection,” 2009. [Online]. Available: http://nsidc.org/data/glacier_photo/.

[17] B. Vishwakarma, B. Devaraju and N. Sneeuw, “What is the spatial resolution of grace satellite products for hydrology?,” *Remote Sensing,* vol. 10, no. 6, 2018.

[18] H. Zekollari, M. Huss and D. Farinotti, “On the imbalance and response time of glaciers in the european alps,” *Geophysical Research Letters,* vol. 47, no. 2, 2020.

[19] L. Foresta, N. Gourmelen, F. Weissgerber, P. Nienow, J. J. Williams, A. Shepherd, M. R. Drinkwater and S. Plummer, “Heterogeneous and Rapid Ice Loss Over the Patagonian Ice Fields Revealed by Cryosat-2 Swath Radar Altimetry,” *Remote Sensing of Environment,* vol. 211, 2018.

[20] Y. Li, “Glacier Changes and Their Linkage to the Climate-Topographic Context in the Borohoro Mountains, Tian Shan 1977-2018,” *Water,* vol. 2, 2020.

[21] P. Malz, W. Meier, G. Casassa, J. Ricardo, P. Skvarca and M. Braun, “Elevation and Mass Changes of the Southern Patagonia Icefield Derived from Tandem-X and Srtm Data,” *Remote Sensing,* vol. 10, 2018.

[22] C. Sommer, P. Malz, T. C. Seehaus, S. Lippl, M. Zemp and M. H. Braun, “Rapid Glacier Retreat and Downwasting Throughout the European Alps in the Early 21st Century.,” *Nature Communications,* vol. 11, 2020.

[23] T. G. Farr, P. A. Rosen, E. Caro, R. Crippen, R. Duren, S. Hensley, M. Kobrick, M. Paller, E. Rodriguez and L. Roth, “The Shuttle Radar Topography Mission,” *Reviews of Geophysics,* vol. 45, 2007.

[24] F. Satge, M. Denezine, R. Pillco, F. Timouk, S. Pinel, J. Molina, J. Garnier, F. Seyler and M.-P. Bonnet, “Absolute and Relative Height-Pixel Accuracy of Srtm-Gl1 Over the South American Andean Plateau,” *Isprs Journal of Photogrammetry and Remote Sensing,* vol. 121, 2016.

[25] E. Berthier, C. Larsen, W. Durkin, M. Pritchard and M. Willis, “Brief Communication: Unabated Wastage of the Juneau and Stikine Icefields (southeast Alaska) in the Early 21st Century,” *Cryosphere,* vol. 12, 2018.

[26] A. Kääb, D. Treichler, C. Nuth and E. Berthier, “Brief Communication: Contending Estimates of 2003-2008 Glacier Mass Balance Over the Pamir-Karakoram-Himalaya,” *The Cryosphere,* vol. 9, pp. 557-564, 2015.

[27] I. Dussaillant, E. Berthier and F. Brun, “Geodetic mass balance of the northern patagonian icefield from 2000 to 2012 using two independent methods,” *Frontiers in earth science,* vol. 6, 2018.

[28] J. Gardelle, E. Berthier and Y. Arnaud, “Impact of resolution and radar penetration on glacier elevation changes computed from dem differencing,” *Journal of glaciology,* vol. 58, pp. 419-422, 2012.

[29] N. Neckel, A. Braun, J. Kropacek and V. Hochschild, “Recent mass balance of the purogangri ice cap, central tibetan plateau, by means of differential x-band sar interferometry,” *Cryosphere,* vol. 7, pp. 1623-1633, 2013.

[30] C. Nuth and K. A., “Co-registration and bias corrections of satellite elevation data sets for quantifying glacier thickness change,” *The Cryosphere,* vol. 5, no. 1, 2011.

[31] G. Moholdt, C. Nuth, J. O. Hagen and J. Kohler, “Recent elevation changes of svalbard glaciers derived from icesat laser altimetry,” *Remote Sensing of Environment,* vol. 114, no. 11, p. 2756–2767, 2010.

[32] M. Zink, “Tandem-x mission status,” *The International Archives of the Photogrammetry, Remote Sensing and Spatial Information Sciences,* vol. XL, no. 7, p. 1345–1352, 2015.

[33] B. Bräutigam, M. Martone, P. Rizzoli, C. Gonzalez, C. Wecklich, D. Borla Tridon, M. Bachmann, D. Schulze and M. Zink, “Quality assessment for the first part of the tandem-x global digital elevation model,” *Isprs - International Archives of the Photogrammetry, Remote Sensing and Spatial Information Sciences,* vol. XL, no. 7, pp. 1137-1143, 2015.

[34] S. Abdullahi, B. Wessel, M. Huber, A. Wendleder, A. Roth and C. Kuenzer, “Estimating penetration-related x-band insar elevation bias: a study over the greenland ice sheet,” *Remote Sensing,* vol. 11, no. 24, p. 2903, 2019.

[35] T. Parrinello, S. Badessi, A. Shepherd, J. Bouffard, T. Casal, M. Davidson, M. Fornari, E. Maestroni and M. Scagliola, “Cryosat: esa's ice mission - eight years in space,” *Advances in Space Research,* vol. 62, no. 6, p. 1178–1190, 2018.

[36] F. Wang, X. Cheng and J. L. Bamber, “Accuracy and performance of cryosat-2 sarin mode data over antarctica,” *Ieee Geoscience and Remote Sensing Letters,* vol. 12, no. 7, p. 1516–1520, 2015.

[37] A. Dehecq, N. Gourmelen, A. Shepherd, R. Cullen and E. Trouvé, “Evaluation of CryoSat-2 for height retrieval over the Himalayan range,” *CryoSat-2 third user workshop,* 2014.

[38] M. Scagliola, N. Tagliani and M. Fornari, “Measuring the Effective Along-Track Resolution of Cryosat,” *Conference: CryoSat Third User Workshop, Dresden, Germany,* 2013.

[39] V. Helm, A. Humbert and H. Miller, “Elevation and elevation change of greenland and antarctica derived from cryosat-2,” *The Cryosphere,* vol. 8, no. 4, p. 1539–1559, 2014.

[40] A. Morris, G. Moholdt and L. Gray, “Spread of svalbard glacier mass loss to barents sea margins revealed by cryosat-2,” *Journal of Geophysical Research: Earth Surface,* vol. 125, no. 8, 2020.

[41] L. Foresta, N. Gourmelen, F. Pálsson, P. Nienow, H. Björnsson and A. Shepherd, “Surface elevation change and mass balance of icelandic ice caps derived from swath mode cryosat-2 altimetry,” *Geophysical Research Letters,* vol. 43, no. 23, p. 138–12, 2016.

[42] T. A. Neumann, A. J. Martino, T. Markus, S. Bae, M. R. Bock, A. C. Brenner, K. M. Brunt, J. Cavanaugh, S. T. Fernandes, D. W. Hancock, K. Harbeck, J. Lee, N. T. Kurtz, P. J. Luers and S. B. Luthcke, “The Ice, Cloud, and Land Elevation Satellite – 2 mission: A global geolocated photon product derived from the Advanced Topographic Laser Altimeter System,” *Remote Sensing of Environment,* vol. 233, 2019.

[43] T. Markus, T. Neumann, A. Martino, W. Abdalati, K. Brunt, B. Csatho, S. Farrell, H. Fricker, A. Gardner, D. Harding, M. Jasinski, R. Kwok, L. Magruder, D. Lubin, S. Luthcke, J. Morison, R. Nelson, A. Neuenschwander, S. Palm and C. S. S. Popescu, “The Ice, Cloud, and land Elevation Satellite-2 (ICESat-2): Science requirements, concept, and implementation,” *Remote Sensing of Environment,* vol. 190, pp. 260-273., 2017.

[44] “ICESat-2 Product Descriptions,” NASA Distributed Active Archive Center (DAAC) at NSIDC, [Online]. Available: https://nsidc.org/data/icesat-2/products/. [Accessed 10 6 2020].

[45] J. A Mcgarry, C. C. Carabajal, J. J. Degnan, A. Mallama, S. P. Palm, R. Ricklefs and J. L. Saba, “ATLAS Flight Science Receiver Algorithms Version 4.0,” National Aeronautics and Space Administration, 2019.

[46] J. DiMarzio and D. Hancock, “Algorithm Theoretical Basis Document for ATLAS Level 1A Processing,” National Aeronautics and Space Administration, 2017.

[47] A. J. Martino, M. R. Bock, C. Gosmeyer, C. Field, T. A. Neumann, D. Hancock, R. L. J. III, P. W. Dabney, C. E. Webb and J. Lee, “Algorithm Theoretical Basis Document (ATBD) for ATL02 (Level 1B) Data Product Processing,” National Aeronautics and Space Administration, 2020.

[48] S. Luthcke, T. Pennington, T. Rebold, B. Loomis and T. Thomas, “Algorithm Theoretical Basis Document (ATBD) for Precise Orbit Determination, Orbit Design, and Geolocation Parameter Calibration, Release 002,” National Aeronautics and Space Administration, 2019.

[49] S. Bae, L. Magruder, N. Smith and B. Schutz, “Algorithm Theoretical Basis Document for Precision Pointing Determination, version 2.0,” University of Texas Applied Research Laboratories, 2019.

[50] T. Neumann, A. Brenner, D. Hancock, J. Robbins, J. Saba, K. Harbeck, A. Gibbons, J. Lee and S. Luthcke, “Algorithm Theoretical Basis Document for Global Geolocated Photons ATL03, Release 003,” National Aeronautics and Space Administration, 2020.

[51] S. B. Luthcke, T. Pennington, T. Rebold and T. Thomas, “Algorithm Theoretical Basis Document (ATBD) for ATL03g ICESat-2 Receive Photon Geolocation,” National Aeronautics and Space Administration, 2019.

[52] RGI Consortium, “Randolph Glacier Inventory – A Dataset of Global Glacier Outlines: Version 6.0: Technical Report,” Global Land Ice Measurements from Space, Colorado, USA, 2017.

[53] L. Petrov, “Algorithm Theoretical Basis Document (ATBD) for Atmospheric delay correction to laser altimetery ranges,” National Aeronautics and Space Administration, 2014.

[54] R. Lucchesi, “File Specification for GEOS FP. GMAO Office Note No. 4 (Version 1.2),” Global Modeling and Assimilation Office, http://gmao.gsfc.nasa.gov/pubs/office_notes, 2018.

[55] B. Smith, D. Hancock, K. Harbeck, L. Roberts, T. Neumann, K. Brunt, H. Fricker, A. Gardner, M. Siegfried, S. Adusumilli, B. Csathó, N. Holschuh, J. Nilsson and a. F. Paolo, “Algorithm Theoretical Basis Document (ATBD) for Land Ice Along-Track Height Product (ATL06), Release 003,” National Aeronautics and Space Administration, 2020.

[56] B. Smith, H. A. Fricker, N. Holschuh, A. S. Gardner, S. Adusumilli, K. M. Brunt, B. Csatho, K. Harbeck, A. Huth, T. Neumann, J. Nilsson and M. R. Siegfried, “Land ice height-retrieval algorithm for NASA's ICESat-2 photon-counting laser altimeter,” *Remote Sensing of Environment,* no. 233, 2019.

[57] R. Dubayah, J. B. Blair, S. Goetz, L. Fatoyinbo, M. Hansen, S. Healey, M. Hofton, G. Hurtt, J. Kellner, S. Luthcke and e. al., “The global ecosystem dynamics investigation: high-resolution laser ranging of the earth’s forests and topography,” *Science of Remote Sensing,* vol. 1, 2020.

[58] D. Coyle, P. Stysley, F. Chirag, E. Frese and D. Poulios, “The Global Ecosystem Dynamics Investigation (GEDI) Lidar laser transmitter,” *Proceedings of SPIE - the International Society for Optical Engineering,* vol. XXVII, 2019.

[59] S. B. Luthcke, T. Rebold, T. Thomas and T. Pennington, “Algorithm Theoretical Basis Document (ATBD) for GEDI Waveform Geolocation for L1 and L2 Products, version 1.0,” National Aeronautics and Space Administration, 2019.

[60] M. Hofton and J. B. Blair, “Algorithm Theoretical Basis Document (ATBD) for GEDI Transmit and Receive Waveform Processing for L1 and L2 products, version 1.0,” National Aeronautics and Space Administration, 2019.

[61] Open Data Österreich, “Digitales Geländemodell Tirol,” [Online]. Available: https://www.data.gv.at/katalog/dataset/0454f5f3-1d8c-464e-847d-541901eb021a. [Accessed 5 6 2020].

[62] Open Data Österreich, “Digitales Geländemodell (DGM) Österreich,” [Online]. Available: https://www.data.gv.at/katalog/dataset/b5de6975-417b-4320-afdb-eb2a9e2a1dbf. [Accessed 5 6 2020].

[63] J. Abermann, M. Kuhn, A. Lambrecht and A. Fischer, “Quantifying changes and trends in glacier area and volume in the austrian ötztal alps (1969-1997-2006),” *Cryosphere,* vol. 3, no. 2, p. 205–215, 2009.

[64] Land Tirol, “Laserscandaten,” [Online]. Available: https://www.tirol.gv.at/sicherheit/geoinformation/geodaten/laserscandaten/. [Accessed 12 11 2020].

[65] F. Paul, P. Rastner, R. L. Bris, R. S. Azzoni, G. Diolaiuti, D. Fugazza, C. Smiraglia, J. Nemec, G. Schwaizer, A. Rabatel and M. Ramusovic, “Glacier shrinkage in the alps continues unabated as

revealed by a new glacier inventory from sentinel-2," *Earth System Science Data,* vol. 12, no. 3, p. 1805–1821, 2020.

[66] H. Ledoux, K. Arroyo and O. R. Peters, "Computational modelling of terrains," 2019. [Online]. Available: https://github.com/tudelft3d/terrainbook/releases. [Accessed 10 10 2020].

[67] H. Wackernagel, "Heterotopic Cokriging," in *Multivariate Geostatistics*, Springer-Verlag, 2003, pp. 158-161.

[68] K. Helfricht, M. Huss, A. Fischer and J. C. Otto, "Calibrated Ice Thickness Estimate for All Glaciers in Austria," *Frontiers in Earth Science,* vol. 7, 2019.

[69] H. C. Ren, Q. Yan, Z. J. Liu, Z. Q. Zuo, Q. Q. Xu, F. F. Li and C. Song, "Study on analysis from sources of error for Airborne LIDAR," *IOP Conference Series: Earth and Environmental Science,* vol. 46, no. 1, 2016.

[70] J. Höhle and M. Höhle, "Accuracy assessment of digital elevation models by means of robust statistical methods," *ISPRS Journal of Photogrammetry and Remote Sensing,* vol. 64, p. 398–406, 2009.

[71] G. Weyss, "Pasterze Glacier: From the Glacier Photograph Collection, National Snow and Ice Data Center," 2013. [Online]. Available: http://nsidc.org/data/glacier_photo/.

[72] C. Charalampos, F. Andrea, K. Michael, L. Astrid, M. Christoph, T. Konstantinos and W. Markus, "Mass-budget anomalies and geometry signals of three austrian glaciers," *Frontiers in Earth Science,* vol. 6, 2018.

[73] C. C. Carabajal and J.-P. Boy, "Icesat-2 altimetry as geodetic control," *International Archives of the Photogrammetry, Remote Sensing and Spatial Information Sciences - Isprs Archives,* vol. 43, p. 1299–1306, 2020.

[74] J. Nilsson, L. Sandberg Sørensen, V. R. Barletta and R. Forsberg, "Mass changes in arctic ice caps and glaciers: implications of regionalizing elevation changes," *The Cryosphere,* vol. 9, no. 1, p. 139–150, 2015.

[75] C. Nuth, G. Moholdt, J. O. Hagen, A. Kaab and J. Kohler, "Svalbard glacier elevation changes and contribution to sea level rise," *Journal of Geophysical Research F: Earth Surface,* vol. 115, no. 1, 2010.

[76] Land Salzburg, "ALS Befliegungen," [Online]. Available: https://www.salzburg.gv.at/verwaltung_/Seiten/als_befliegungen.aspx. [Accessed 22 11 2020].

[77] F. Brun, P. Wagnon, E. Berthier, V. Jomelli, S. B. Maharjan, F. Shrestha and P. D. A. Kraaijenbrink, "Heterogeneous influence of glacier morphology on the mass balance variability in high mountain asia," *Journal of Geophysical Research: Earth Surface,* vol. 124, no. 6, 2019.

[78] T. Jóhannesson, C. Raymond and E. Waddington, "Time–scale for adjustment of glaciers to changes in mass balance," *Journal of Glaciology,* vol. 35, no. 121, p. 355–369, 1989.